Continental Deformation: Collisional Orogenesis to Passive Margin Processes

A Dissertation Presented to

The Faculty of the Department of Earth and Atmospheric Sciences

University of Houston

In Partial Fulfillment

of the Requirements for the Degree

Doctor of Philosophy

By

John M. Cannon

December 2016

Continental Deformation: Collisional Orogenesis to Passive Margin Processes

John M. Cannon

APPROVED:

Dr. Michael A Murphy, Chairman

Dr. Alexander Robinson

Dr. Joel Saylor

Dr. Michael Taylor
University of Kansas

Dean, College of Natural Sciences and Mathematics

Acknowledgements

I would like to thank my committee, especially Dr. Murphy for providing me with patient guidance and a sounding board for my incessant theorizing. I could not have done it without you. The last five years have been both difficult and rewarding, without my fellow graduate students (Yiduo, Tom, Adrian, Jen, Ben, Mike… et al.) keeping me grounded and helping me with the occasional bit of fun it would have been a far greater struggle. Finally I want to thank Sandy, my wife, whose constant love, support (emotional and financial), and faith in me made this all possible.

Continental Deformation: Collisional Orogenesis to Passive Margin Processes

An Abstract of a Dissertation

Presented to

The Faculty of the Department of Earth and Atmospheric Sciences

University of Houston

In Partial Fulfillment

of the Requirements for the Degree

Doctor of Philosophy

By

John M. Cannon

December 2016

Abstract

My research investigates continental deformation at opposing ends of the Wilson cycle, intracontinental collision and passive margin development. I present a map of NW Nepal river channel steepness (k_{sn}), a proxy for rock uplift rate over 10^3-10^5 years, coupled with a seismotectonic model, and then expand this map and accompanying model to the entire Himalaya; and a subsidence analysis of the northern abyssal Gulf of Mexico (GoM), which I use to evaluate numerical models of North American dynamic topography. GPS shows southern Tibet creeps south at the same rate river terraces are deformed at the range front. The India-Asia intracontinental subduction zone, the Main Himalayan Thrust (MHT) is a lithospheric fault whose style of motion changes from seismogenic in the brittle upper-middle crust, to aseismic in the ductile middle-lower crust. I determine correlation coefficients between k_{sn} and: MHT coupling, lithology, and precipitation using a series of cross-orogen profiles. Averaging the results reveals a strong correlation between k_{sn} and MHT coupling (-0.6), a moderate correlation with lithology (0.3), and a weak correlation with precipitation (-0.1). This leads me to interpret the k_{sn} map in terms MHT coupling. I use it to divide the range into 7 segments based on the size and position of clusters of high k_{sn} rivers. At the other end of the Wilson cycle, in the post rift phase, passive margins develop, accumulate sediment, and subside. Numerical models of Mesozoic-Recent mantle circulation suggest that North America experienced a km of dynamic

subsidence as the sinking Farallon slab passed beneath it. I tested this by conducting a subsidence analysis of the northern abyssal GoM, and show that it underwent three episodes of enhanced subsidence. First is early Cretaceous (142-97 Ma), second is early Cenozoic (65-49 Ma), and thirds is late Cenozoic (34 Ma – 10 ka) which correlate with thermal contraction and density driven subsidence, asymmetric basin filling, and flexure beneath a rapidly prograding shelf margin wedge, respectively. My results show that GoM subsidence can be adequately explained without the influence of the sublithospheric passage of a subducted slab.

Contents

Chapter 1 Active lower crustal deformation and Himalayan seismic hazard revealed by stream channels and regional geology

Cannon, J., and Murphy, M., 2014, Active lower crustal deformation and Himalayan seismic hazard revealed by stream channels and regional geology: Tectonophysics, v. 633, p. 34-42.

1.1 Chapter Summary

Thick Tibetan crust stores energy driving large earthquakes along its margins. At its southern margin, it is hypothesized that its lower crust is extruded between an upper and lower shear zone, such that strain in the ductile lower crust is fed into the higher seismogenic portions of the crust predicting rapid rock uplift between these structures. The upper shear zone is regionally referred to as the South Tibetan detachment (STD) and the lower shear zone is referred to as the Main Central thrust (MCT). I use field mapping and k_{sn} channel steepness analysis to test this hypothesis in northwestern Nepal within a notable gap in historic seismicity. Here, I show a ~170 km x 40 km swath of rapid rock uplift at the southern margin of the Tibetan Plateau that overlaps a regional anticline suggesting active folding. The area of rapid uplift coincides with peak interseismic strain as determined by GPS and overlies the inferred locked-to creeping transition along the India-Asia plate boundary. The fold is cored by thick ductiley deformed crust and defined by a shear zone interpreted as the STD. Because the STD is folded, this structure is precluded from facilitating active extrusion of a mid-crustal channel. A regional cross section across the fold shows

that while the uppercrust has little post-Miocene shortening, the lower middle crust is anomalously thick. I explain this by duplexing that has occurred since the Middle Miocene whereby thrust-sense shear zones stack ductile lower-middle crust beneath the STD and north (downdip) of the locked-to creeping transition. The plate boundary here has not ruptured since the Mw 8.2 AD 1505 earthquake whose inferred rupture area encompasses the region of rapid rock uplift shown here, predicting a high slip potential. Integrating the structural geology and k_{sn} analysis with microseismicity patterns and the 1505 surface rupture suggests that in western Nepal the locked to creep transition is ~40 km wide and lies 100-120 km north of the Himalayan thrust front.

1.2 Introduction

The Himalayan thrust wedge actively absorbs ~ 2 cm yr^{-1} of convergence between the Indian plate and stable Eurasia, resulting in large amounts of crustal shortening, surface uplift, and recurring large (Mw>8) earthquakes (Ader et al., 2012; Bilham et al., 2001). Geometrically, the thrust wedge contains several major thrust faults that sole into the basal Main Himalayan Thrust (MHT) (Pandey et al., 1999). The MHT "decouples" the Himalayan wedge from the subducting Indian plate and breaks the surface in the sub-Himalaya along the Main Frontal Thrust (MFT; Figure 1.1a, b) (Kumar et al., 2006; Sapkota et al., 2013). In central Nepal coeval slip on thrust and normal faults is inferred to

facilitate active southward extrusion of middle-lower crust (Hodges et al., 2004; McDermott et al., 2013; Wobus et al., 2005). The inferred active thrust fault(s) near the Main Central Thrust (MCT) broadly coincide with the lone belt of microseismicity in central Nepal. This spatial relationship and has been hypothesized to represent a kinematic link between ductile lower crustal strain and surface deformation (Hodges et al., 2004). Whereas microseismic epicenters in central Nepal form a single linear cluster 80-100 km north of the MFT coincident with an interpreted major ramp in the MHT (Cattin and Avouac, 2000; Pandey et al., 1995; Schelling and Arita, 1991), in western Nepal at 82° 15'E this linear cluster bifurcates into two subparallel belts (Figure 1.2) 80-100 km and 120-150 km from the MFT. These belts remain distinct until 81°15' where they converge again into a single belt with a different orientation than observed in central Nepal (Cattin and Avouac, 2000). These belts of microseismicity appear to be collocated with small ramps in the MHT (Pandey et al., 1999), indicating that the geometry of the MHT is different in central and western Nepal. In this interpretation the geometry of the MHT in central Nepal is best described by a single large ramp 100 km from the MFT while in western Nepal its geometry is better described by a series of smaller ramps (Pandey et al., 1999). The northern limit of MHT microseismicity has been interpreted to mark the locked-creeping transition along the plate boundary between India and Asia (Cattin and Avouac, 2000) which appears to be 50 km further from the MFT in western Nepal than in

central Nepal. This is consistent with a regionally segmented MHT whose dip is significantly shallower in western Nepal than in central Nepal.

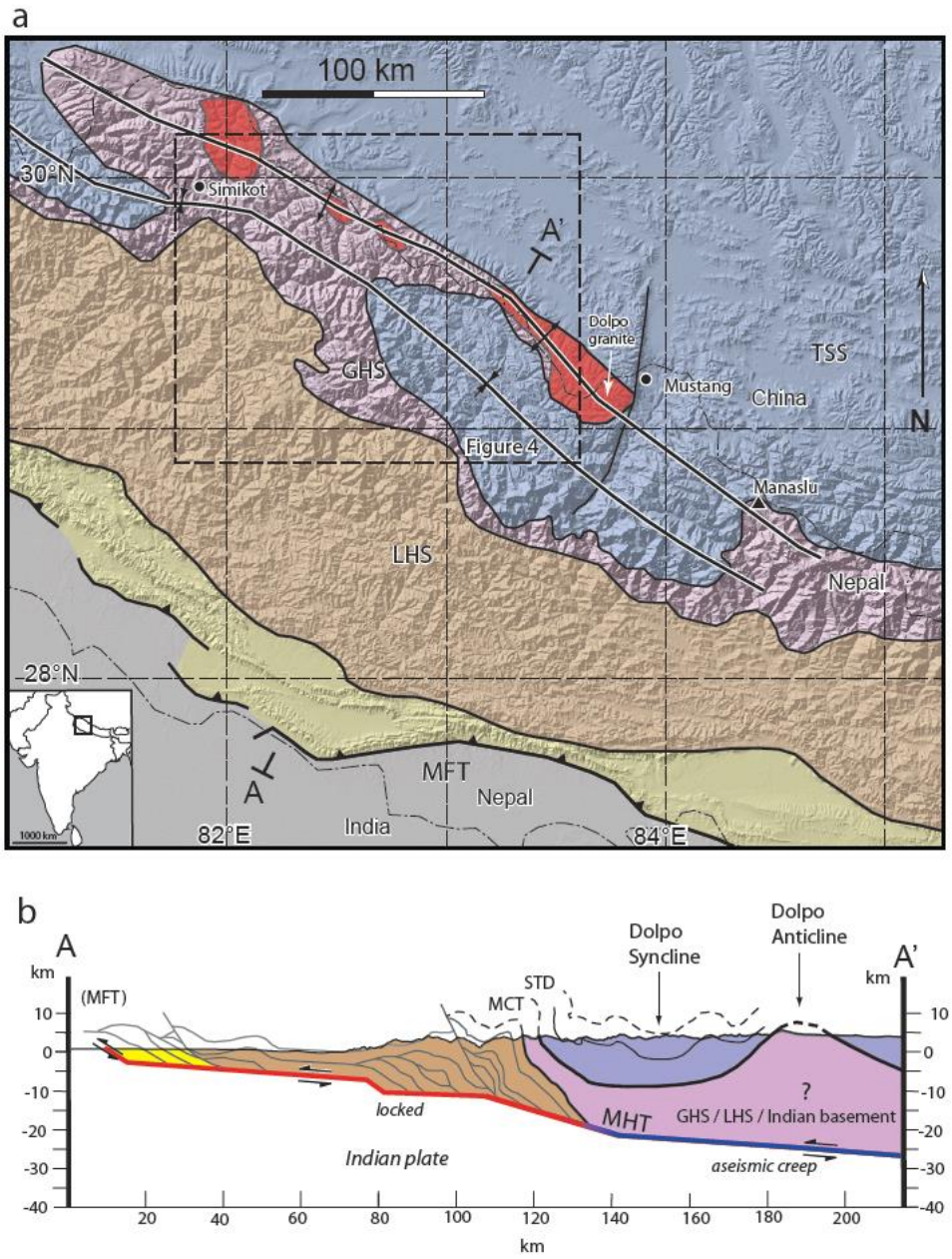

Figure 1.1 a) Regional geologic map of the Himalayan thrust wedge highlighting the Dolpo fold which coincides with significant crustal thickening and high GPS-derived vertical uplift rate (Ader et al., 2012). Insets show rupture areas of historical earthquakes (Bilham and Ambraseys, 2005) and GPS determined uplift rates (Ader et al., 2012). b) Cross section across Dolpo folds, geology south of syncline after (Robinson, 2008), MHT geometry north of syncline is from Caldwell (2013), the transition from aseismic creep (blue) to locked (red) corresponds to the intersection of the 350 °C isotherm with the MHT (Herman et al., 2010).

Much of the convergence of India relative to Tibet is stored elastically along the southern margin of plateau and is released in great earthquakes which rupture patches of the plate boundary extending from southern Tibet to the MFT (Bilham et al., 2001; Feldl and Bilham, 2006). The rate of south directed creep of Tibet relative to a fixed India is within error of the Pliocene to recent MFT slip rate calculated from offset river terraces (Lavé and Avouac, 2001) suggesting that the creep imparted strain is entirely elastic and does not significantly deform the thrust wedge (Cattin and Avouac, 2000). In this view, the moment magnitudes of all great Himalayan earthquakes in the 500 year historical record (Figure 1.3) can be summed and compared with an extrapolation of GPS derived interseismic strain rates over the same time period to calculate how much strain is currently stored in the wedge (Bilham and Ambraseys, 2005). This calculation results in a 75% strain deficit equivalent to four Mw 8.5 earthquakes implying that either large earthquakes are imminent, missing from the historical record, or that the magnitude of historical earthquakes has been underestimated (Bilham and Ambraseys, 2005). Alternatively the strain deficit would be lower if the thrust wedge deforms internally. In western Nepal an active cross orogen transtentional fault system has been interpreted to link the Gurla Mandhata core complex with the MFT (Murphy et al., 2014; Styron et al., 2011), and in central Nepal active thrust faulting is interpreted near the MCT and South Tibetan Detachment (STD) based on river channel steepness analysis and thermochronology (Bollinger et al.,

2004a; Herman et al., 2010; Hodges et al., 2004; Huntington et al., 2006; McDermott et al., 2013; Wobus et al., 2005), all of these indicate regionally significant internal deformation of the thrust wedge. In this contribution, I integrate geologic mapping with stream channel analyses to assess internal deformation of the thrust wedge in northwest Nepal.

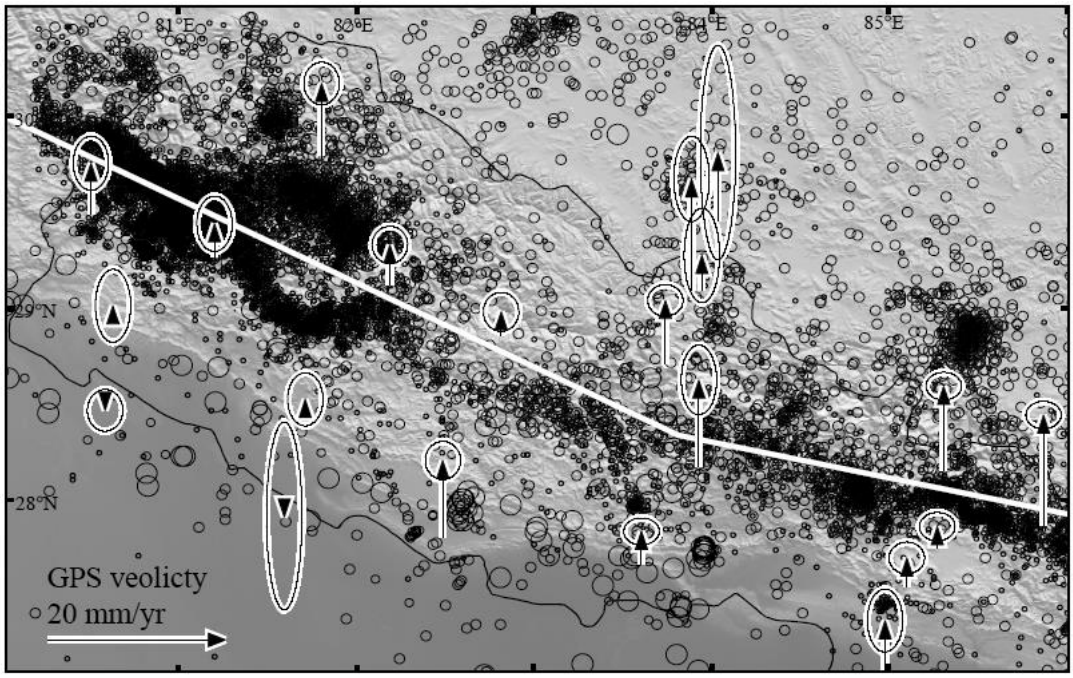

Figure 1.2. Map of microseismicity recorded between 04/01/1995 and 04/11/2000, Nepal Seismological Center, Department of Mines and Geology (Bollinger et al., 2007), and vertical GPS velocity (Ader et al., 2012) thick white line is the modeled dislocation (dislon) of (Jouanne et al., 2004).

1.3 Background

1.3.1 Regional Geology

Geologic mapping of the Dolpo region was conducted at 1:50,000 and compiled with previous mapping by Fuchs (1973). This mapping shows the presence of a pair of large folds defined by the contact between the Greater Himalayan Sequence (GHS) and the Tethyan Sedimentary Sequence (TSS) (Figure 1.4 and 1.5). The anticline is a gentle fold with a half wavelength of 50 km whose axial trace extends W-NW for ~400 km (Figure 1.1a and b) and defines Tibet-Himalaya drainage divide throughout the region. The regional map pattern indicates the folds are doubly plunging (Figure 1.1a). The crest of the anticline lies along the Nepal-China border, here the fold axis is horizontal (01° toward N67W) and represents a culmination in the anticline (Figure 1.4). Field measurements of the anticline's forelimb (southwest limb) show that its average attitude is S66E/31 SW. Measuring the orientation of its backlimb (northeast limb) was not possible in the field as it is located north of the Nepal-China border where travel is restricted. Instead I make use of 0.5 m resolution DigitalGlobe images overlaid on a 90 m STRM digital elevation model in Google earth to conduct three point problems on prominent bedding traces and contacts along the anticline's backlimb at ten locations. These calculations resulted in an average orientation of N74W/9 NE. Stereonet analysis of the combined field and satellite image derived measurements show a 140° interlimb angle and an axial plane

oriented N67W/79 NE (Figure 1.4).

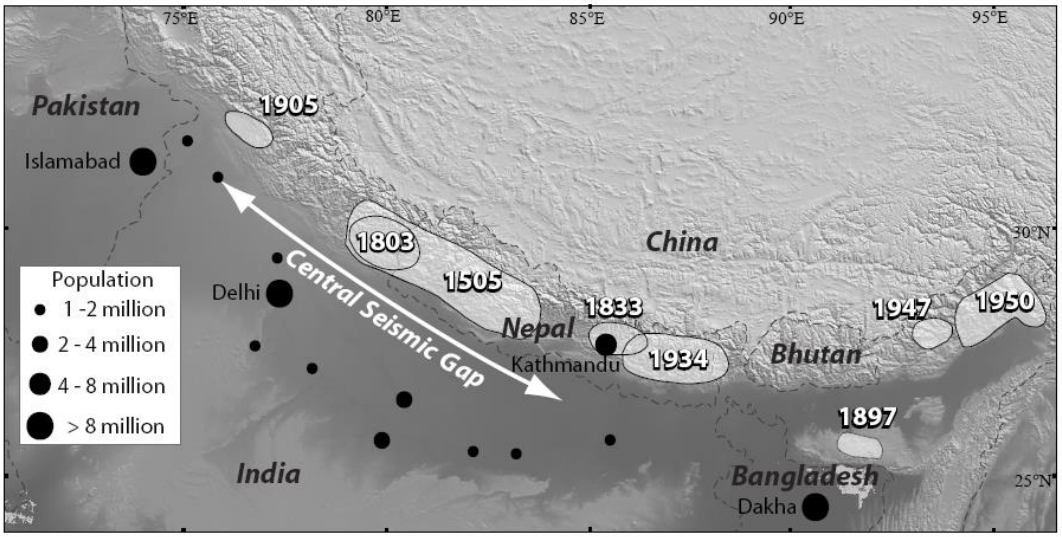

Figure 1.3. Map of inferred rupture areas of large historical earthquakes from 1500 AD to the present after Bilham et al. (2001).

The GHS in Dolpo is comprised of quartzofeldspathic gneisses, quartzites, biotite garnet-kyanite schists and gneisses, amphibolite gneisses, calc-silicate gneisses, and migmatites (Fuchs, 1973; this study), which are intruded by the Dolpo-Mugu leucogranite (Le Fort, 1995), referred to here as the Dolpo granite. The Dolpo granite has a single published Th^{232}-Pb^{208} monazite age of 17.6 $\pm$ 0.3 Ma (Harrison et al., 1999). Overlying the GHS are calc-silicate schists, marbles, and phyllites of the basal section of the Dhaulagiri Limestone which lies at the base of the Tethyan Sedimentary Sequence (TSS) (Fuchs, 1973). The TSS in Dolpo is made up of Paleozoic through Mesozoic metasedimentary to sedimentary rocks with a minimum thickness of ~9 km (Colchen et al., 1980) which decrease in metamorphic grade up section, and are pervasively folded and

faulted (Figure 1.4 and 1.5). The upper GHS and lower TSS in Dolpo are characterized by a diffuse shear zone several hundred meters thick within calcareous schists intercalated with biotite schist. Mineral stretching lineations within this shear zone are defined by aligned aggregates of quartz, biotite, and feldspar. Their trends show ENE-directed shear in the northern part of the mapped area and a more easterly direction in the southeast. Although the shear zone is regionally folded, unfolding the mineral stretching lineations along the regional fold axes does not result in any significant change to their trend. I and others interpret this shear zone as the South Tibetan Detachment (STD) (Carosi et al., 2007). Within and below the shear zone rocks are pervasively intruded by leucogranite dikes and sills and look similar to the lower plate observed in central Nepal and southern Tibet (Burchfiel et al., 1992; Murphy and Harrison, 1999; Searle, 1999) where it is described as an injection complex. The metamorphic grade reaches amphibolite facies based on the presence of diopside and garnet in calcareous schist layers (See Figure 5a-d). Toward the top of the shear zone diopside is notably absent in the upper plate as are the plutonic bodies, peak metamorphism reaches only the biotite zone of greenschist facies as observed by Carosi et al. (2007). The STD in this region is estimated to have ceased moving at ca. 19-16 Ma (Godin et al., 2006b; Searle and Godin, 2003) implying that development of the Dolpo folds could not have initiated before this time. The eastern end of the Dolpo folds are cut by normal faults in the Thakkhola graben which are estimated to have been active by 14-11 Ma (Coleman and Hodges,

1995; Garzione et al., 2003). These age estimates bracket folding to have occurred between 19-16 Ma and 14-11 Ma. However, continuous intracontinental subduction makes it clear that the onset of extension does not define the cessation of shortening suggesting that the Dolpo folds may be active. While the wavelength, structural relief, and the observation that GHS rocks are involved in the folding, indicate that deformation originates deep in the thrust wedge.

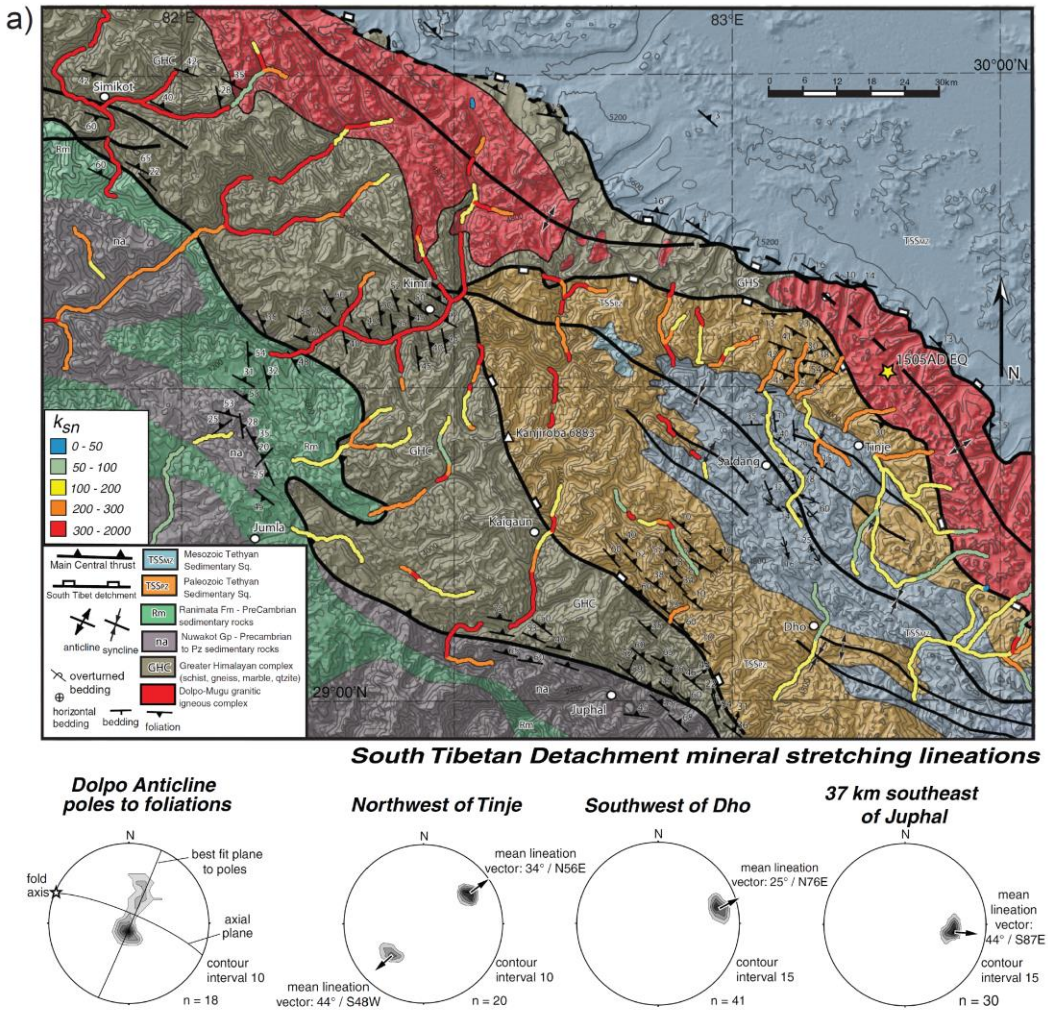

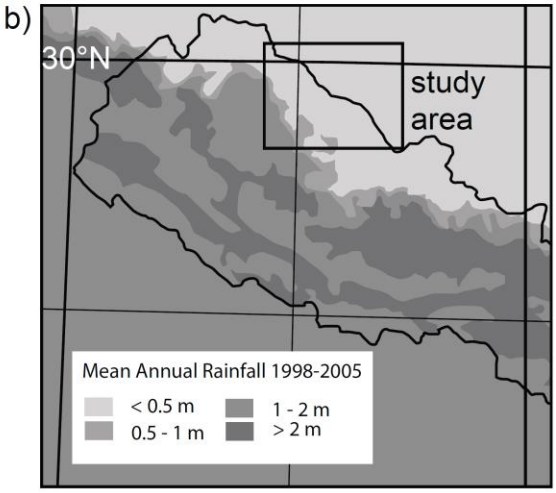

Figure 1.4 a) Geologic map and structural data of the Dolpo and Mugu Districts complied from our own mapping and that of Fuchs (1973) with channel steepness (ksn). The map highlights the Dolpo anticline defined by the STD. Structural data show STD shear sense is top-to-the-NE. b) Map of average annual percipitation from 1998-2005 after Bookhagen and Burbank (2006).

1.3.2 Channel steepness and Rock Uplift Rate

Relating channel steepness to rock uplift rate relies on the observation that graded streams in steady-state display a gentle concave up exponential shape (Hack, 1957), such that channel slope combined with available discharge and channel characteristics is balanced by available stream power to move the load supplied from upstream (Davis, 1902; Gilbert and Dutton, 1877; Mackin, 1948). This requires that in steady-state landscapes the rate of erosion be equal to the rate of material supplied to the system i.e. rock uplift, implying that when rock uplift outpaces incision, rivers get steeper. This allows channel steepness to be used as a proxy for rock uplift rate using the equation $S = k_{sn}A^{-\theta \mathrm{ref}}$ (Wobus et al., 2006), in which slope (S) is related to upstream drainage area (A), normalized channel steepness (k_{sn}), and a reference profile concavity (θ_{ref}). The use of channel longitudinal profiles to investigate active tectonics was pioneered by Seeber and Gornitz (1983) who analyzed gradients of major transverse Himalayan rivers to examine how tectonic processes relate to channel morphology. They found that the steepest gradients along rivers correspond with bands of microseismicity beneath the High Himalaya, and interpreted this as evidence of persistent rock uplift by an active orogen scale fault (Seeber and Gornitz, 1983). While normalized channel steepness (k_{sn}) has supplanted channel gradient as the index of choice for relating rock uplift rate to landscape response (Kirby and Whipple, 2001; Kirby and Whipple, 2012; Wobus et al., 2006) the observation that the pattern of rock uplift over 10^4-10^5 years (Whipple and Tucker, 1999) inferred

from river channel steepness resembles that of modern interseismic strain has been confirmed repeatedly (Ader et al., 2012; Bilham et al., 1997; Cattin and Avouac, 2000; Grandin et al., 2012; Hodges et al., 2004; Kirby and Whipple, 2012; Meade, 2010). This co-location has been hypothesized to reflect an inelastic component of southern Tibetan plateau margin strain accumulation (Bilham et al., 2001), or in central Nepal as southward migration of a MHT ramp via underplating accompanied by a delayed erosional response at the surface (Grandin et al., 2012).

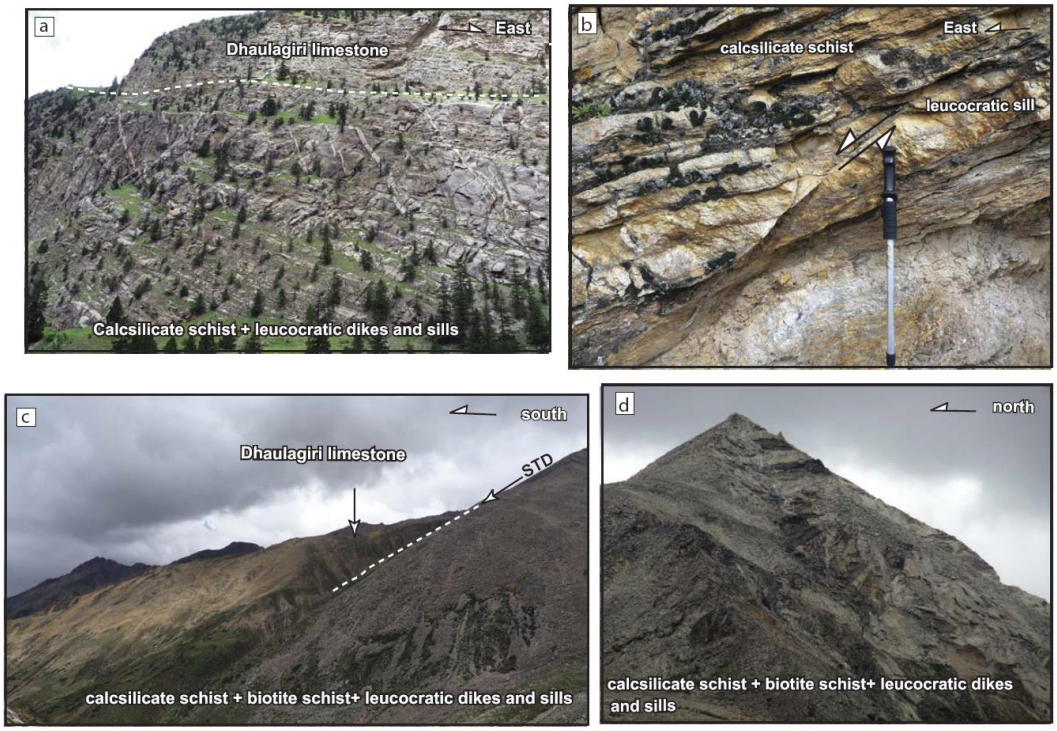

Figure 1.5. a) Photo of the STD approximately 12 km east of Juphal (dashed white line). STD juxtaposes the lower section of the Dhaulagiri limestone in its upper plate against mylonitic calc-silicate schists and leucocratic dikes and sills in the lower plate, view is to the north. b) Photo of STD lower plate showing a leucocratic sill and calc-silicate mylonitic schist cut by a top-to-northeast extensional shear zone, view to the north. c) Photo of the STD approximately 24 km northeast of Tinje, along the southern limb of the Dolpo antlicline (dashed white line). STD juxtaposes the lower section of the Dhaulagiri limestone in its upper plate against mylonitic calc-silicate and biotite mylonitic schists and leucocratic dikes and sills in the lower plate, view is to the west. d) Photo of the STD lower plate injection complex at the crest of the Dolpo anticline, view to the east.

1.4 Methods

The normalized channel steepness (k_{sn}) analysis was conducted using ASTER (Advanced Spaceborne Thermal and Reflection Radiometer) Global Digital Elevation Model V002 with a nominal resolution of 15 m. 63 channels in

the upper Dolpo and Mugu districts were analyzed using the method described in (Wobus et al., 2006). The fluvial scaling relationship described in equation 1 only applies above a critical drainage area (Kirby et al., 2003) of 1-10 km^2, therefore I exclude the upper reaches of catchments with contributing drainage areas less than 10 km^2. Channel reaches with glacial morphology (e.g. wide flat bottomed valleys) are also excluded, this generally equates to reaches above 5000 m for tributaries and 4000 m for trunk channels in our study area. Spikes were removed from the raw DEM data with a moving averaging window of 250 m. Reaches with near constant gradients were chosen for analysis using a logarithmic plot of gradient vs. downstream distance. Channel steepness was normalized to a reference concavity of 0.45, typical of catchments with uniform lithology and uplift rate (Kirby and Whipple, 2001; Kirby and Whipple, 2012), as well as allowing for easy comparison with recent studies (Kirby and Ouimet, 2011; Ouimet et al., 2009; Wobus et al., 2006).

Lithology and climate influence channel steepness as well and their effects must be considered. I overlay our k_{sn} data on our geologic map to test for lithologic control on channel steepness and evaluate climatic effects by examining rainfall gradients in our study area using satellite derived precipitation data (Figure 1.4a and b) (Bookhagen and Burbank, 2006). Where it is established that lithology and climate are not the dominant regional controls on channel steepness, normalizing steepness to a reference channel concavity allows changes in k_{sn} across the region can be interpreted as either a transient response to a change in

local base level or as variations in rock uplift rate (Kirby and Whipple, 2001; Kirby and Whipple, 2012; Wobus et al., 2006). As I know of no regional base level fall which can be invoked to drive channel steepening in the Dolpo area, I interpret our results to reflect changes in relative rock uplift rate.

1.5 Results

The correlation between lithology and channel steepness is a function of the relative resistance to erosion of different lithologies, and our study area is no exception. The steepest channels are mainly found within the high grade metamorphic rocks of the GHS and the channels with approximately equilibrium profiles are nearly all found within the greenschist facies to unmetamorphosed TSS (Figure 1.4). However significant variation in channel steepness exists within each lithology and channel profiles cross contacts with no interruption in steepness suggesting that rock uplift rate plays a dominant role in the regional pattern of channel steepness. Channel longitudinal profiles were examined for deviations from equilibrium in steepness and concavity, steepness was calculated at 1 km intervals along the length of the profiles to determine average values. On this basis the region is divided into a relatively high-uplift rate area in which channels are generally convex and characterized by high average k_{sn} 128-518 with a regional average of 378; and a relatively low-uplift rate area of concave, approximately equilibrium profiles with average k_{sn} of 98-264, and a regional

average of 139. Channels in high-uplift rate drainages are seen with red and orange channel segments corresponding to k_{sn} values over 200 while channels in low-uplift rate drainages are seen with yellow and green channel segments corresponding to k_{sn} values under 200 (Figure 1.4). See Figure 1.6 for comparison of high-uplift rate and low-uplift rate longitudinal profiles. I show a 170 km long swath of convex over-steepened channels coincident with the forelimb (southwest limb) of the Dolpo anticline which extends from 81° 45'E to 83° 15'E. The width of the swath varies from 50 km between Simikot and Kanjiroba to 30 km at its eastern end near Tinje (Figure 1.4). The most convex and highest average k_{sn} channels are concentrated in the northwest, in the vicinity of Jumla and Simikot. In the southeast half of the study area the core of the syncline is characterized by concave profiles with low k_{sn}. The low-uplift rate area terminates to the northwest where the syncline's axial trace enters the Jumla and Simikot areas (Figure 1.4). Here the high-uplift rate area extends south of the syncline's axial trace, suggesting the presence of an active structure.

The most rapid rock uplift predicted by the channel-steepness analysis correlates spatially with several geophysical observations: (i) a northwest-trending cluster of microseismicity (Cattin and Avouac, 2000; Pandey et al., 1995; Pandey et al., 1999); (ii) a northwest-trending dislocation (dislon) in simulations of the present-day displacement field with a locking depth at 21-17 km (Jouanne et al., 2004) (Figure 1.2); (iii) the intersection of the 350 °C isotherm (Herman et al., 2010) with the MHT (Caldwell et al., 2013) (Figure 1.1b); and (iv) peak

interseismic uplift (Ader et al., 2012; Bilham et al., 1997; Grandin et al., 2012) (Figure 1.2) suggesting that they share a common mechanism. The microseismicity is interpreted to be driven by stress build-up at the southern tip of the transition (locking line/dislon) between the northern creeping and southern locked segments of the MHT (Jouanne et al., 2004), its position being largely a function of the thermal structure of the MHT (Herman et al., 2010) which controls the rheologic transition from ductile to brittle. The area immediately north of the locking line coincides with peak interseismic uplift recorded by GPS stations where strain is concentrated in a ~50 km wide band running the length of the Himalaya (Bilham et al., 2001). While most of this strain is elastic and destined to be released in plate boundary earthquakes (Feldl and Bilham, 2006) the presence of an apparently active regional fold within this zone of strain accumulation suggests a portion is permanent.

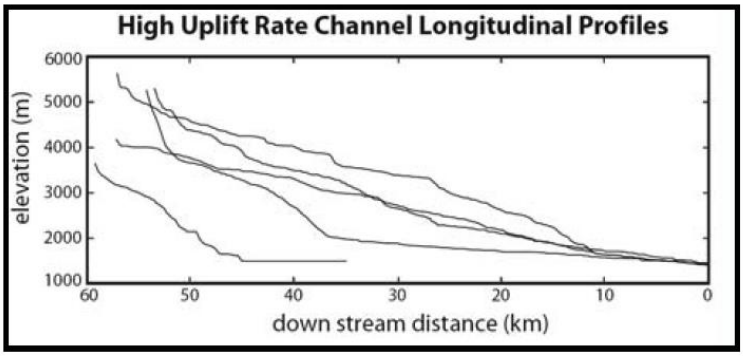

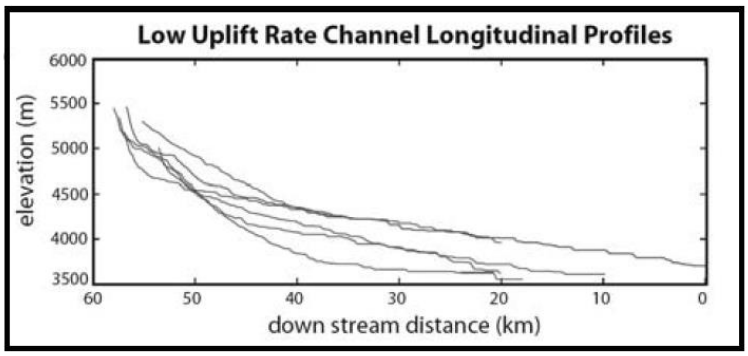

Figure 1.6. Channel longitudinal profiles from the interpreted high- and low-uplift rate areas.

1.6 Discussion

1.6.1 Strain Accumulation and Seismic Hazard

I interpret uplift north of the locking line in Dolpo to be driven by a long-lived duplex in the lower-middle crust which localizes deformation in a narrow band coincident with the Dolpo anticline suggesting that the fold is currently being uplifted and shortened. In this scenario, there is a passive roof thrust below the STD while the MHT serves as the sole thrust. The northeast trending STD

stretching lineation population presented above is consistent with horst blocks being inserted towards the SSW passively beneath it. The second population of STD stretching lineations trending east-west is regionally uncommon (Burchfiel et al., 1992; Godin et al., 2006a; Jessup et al., 2006; Murphy and Harrison, 1999) This duplex model predicts the stacking of rock overlying the MHT along a fault(s) within the thrust wedge (Figure 1.7). Previous studies in northwest Nepal have found that both GHS and LHS rocks underlie the STD in this region (Murphy, 2007). Duplex models predict a foreland migration of the active ramp along which new horst blocks are then incorporated into the wedge. However, I show that the position of uplift and shortening within the hinterland of the thrust wedge in Dolpo has apparently been stationary since the fold formed in the Middle to Late Miocene. While I cannot discern between slow continuous folding and episodic growth, I show that this region has been a locus of uplift and shortening along the plateau margin for time spanning six orders of magnitude: folds 10^6 years, drainages 10^5-10^4 years (Whipple and Tucker, 1999), historic earthquakes 10^2 years, and microseismicity, GPS, and InSAR 10^1 years; indicating persistent rock uplift for at least 100-1000 ka, and possibly since the Late Miocene. The plate boundary south of Dolpo has not ruptured since the AD 1505 Mw earthquake whose magnitude has been interpreted to be between 8.2 Mw and 9.0 Mw (Ambraseys and Jackson, 2003; Bilham and Ambraseys, 2005; Kumar et al., 2006) arguably the most powerful geologic event to strike western Nepal during recorded history. The location of its epicenter has been estimated based on

historical records to plot on the crest of the Dolpo anticline (Figure 1.1a) and it is estimated to have released as little as ~9-15 m of coseismic slip (Ambraseys and Jackson, 2003) and as much as 23 m (Kumar et al., 2006) along a 600-1000 km long rupture (Ambraseys and Jackson, 2003; Bilham and Ambraseys, 2005; Bilham et al., 2001). This earthquake's magnitude strongly suggests a plate boundary rupture, but its epicenter is estimated to be ~ 50 km north of the locked portion of the MHT in a region considered to be continuously creeping (Ader et al., 2012; Ambraseys and Jackson, 2003; Bilham et al., 2001) (Figure 1.1a and b). I note that while the location of the epicenter is uncertain, it nonetheless supports our interpretation of persistent strain accumulation along the MHT locking line producing uplift and shortening above the brittle-ductile transition zone (Bilham et al., 2001; Jouanne et al., 2004). I interpret this process to result in lower middle-crustal duplexing within the thrust wedge north of the locking line which feeds strain from the creeping lower crust into the seismogenic portion of the crust producing the observed northern belt of microseismicity (Figure 1.7).

Extrapolating modern convergence rates back to AD 1505 predicts at least 9 m of elastic strain accumulation in western Nepal (Bilham et al., 2001) and a 250-500 year recurrence interval for Mw 8.2 (Bilham et al., 1995), suggesting that the plate boundary here may be at significant risk of rupturing. However, if the AD 1505 earthquake was Mw 8.7 or greater the predicted recurrence interval would be at least 1000 years (Bilham and Ambraseys, 2005; Kumar et al., 2006). Comparison of geodetically determined convergence rate with energy released in

all known great Himalayan earthquakes since AD 1500 predicts a 75% strain deficit (Bilham and Ambraseys, 2005), however if some of this strain contributes to duplex growth as predicted, or if the AD 1505 earthquake was Mw > 8.7 (Bilham and Ambraseys, 2005; Kumar et al., 2006) then recurrence intervals could be significantly longer reducing the strain deficit. Nevertheless, the presence of a large swath of rapid rock uplift within the rupture area of the AD 1505 earthquake (Figure 1.3) (Bilham and Ambraseys, 2005; Bilham et al., 2001) suggests this segment of the plate boundary is in danger of slipping. If an event of similar magnitude were to occur here today it would affect > 20 million people in Nepal and India.

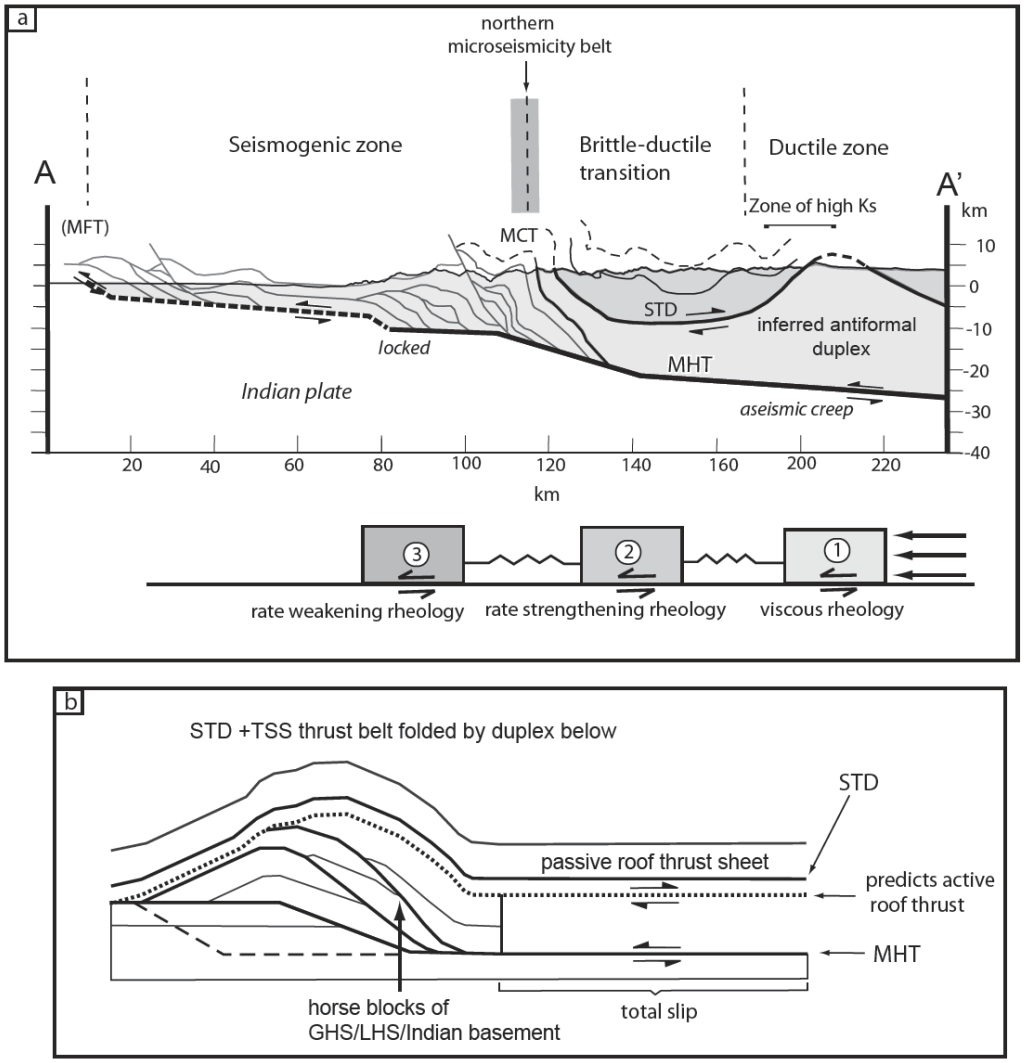

Figure 1.7. a) Seismotectonic model of western Nepal integrating ksn channels steepness analysis, intracontinental subduction zone rheology model (Perfettini and Avouac, 2004), and regional geology. b) Thrust duplex model describing a mechanism to produce large amounts of lower-crustal thickening below a modestly shortened passive roof-thrust sheet.

1.6.2 Seismotectonic Models

Our mapping shows that the STD is folded in western Nepal and therefore cannot participate in active internal deformation in the Himalayan thrust wedge.

This suggests that the kinematics prescribed by channel flow or wedge extrusion models do not adequately describe the post-Miocene kinematics of western Nepal. While it can be argued that the boundaries of a mid-crustal channel or extruding block may migrate up or down over time as has been suggested in central Nepal (McDermott et al., 2013) no evidence of this has yet been found in western Nepal. The channel flow model predicts rapid uplift in the region between the STD and MCT. Our channel steepness analysis shows the uplift pattern correlates better with the southern limb of the Dolpo anticline. Models which could explain the formation of the Dolpo anticline include a fault propagation fold structure, a fault bend fold in the MHT, or an antiformal duplex. Both the fault propagation fold and fault bend fold models require thrust ramps on the order of 10 km in height. While ramps have been imaged in western Nepal none approach the height required to create the Dolpo anticline (Caldwell et al., 2013; Pandey et al., 1999). Rather, I suggest that localized uplift and shortening of the southern plateau margin spanning thousands of seismic cycles is best explained by a hinterland antiformal duplex. Shortening estimates across the Dolpo anticline are complicated by the ductile nature of deformation, the lack of reliable strain markers, and uncertainty regarding the nature of the crust in the core of the anticline. Nevertheless, significant crustal thickening is required beneath the Dolpo anticline. At the trough of the Dolpo syncline the STD lies at 10 km depth while at the crest of the anticline, it projects to ~5 km a.s.l. (see Figure 1.1b), implying more than 10 km of structural relief, while horizontal shortening of the

STD between A' and the syncline's trough appears to be only 10% - 20%. Estimates of the amount of crustal thickening are strongly dependent on the nature of the middle crust in the core of the anticline. If the GHS occupies the entire region above the MHT then it has been thickened 5x based on its local thickness (see Figure 1.1b), however if there are LHS or underplated Indian basement rocks above the MHT then the GHS may only be doubled in thickness. These estimates bracket the ratio of GHS vertical thickening to STD horizontal shortening to be between 2:1 and 5:1, and guide our interpretation that the anticline results from an antiformal duplex in the lower-middle crust (Figure 1.7) producing hinterland crustal thickening with minimal upper crustal shortening. In this model the northern cluster of microseismic events nucleate on a ramp in the MHT 110 km to 150 km from the MFT and defining the regional locking line. The AD 1505 earthquake was initiated by stress accumulation at the rheologic transition from ductile to brittle along the MHT north of the locking line along a 600-1000 km long segment of the arc, the eastern portion of which lies below the Dolpo anticline. This earthquake rupture mechanism has been modeled for large earthquakes nucleating at depths of 10-20 km and temperatures of 300-350 °C in continental crust (Huc et al., 1998), the same conditions predicted to be present along the MHT below the fold.

The Dolpo anticline lies above the ductile portion of the MHT and north of the northern belt of microseismicity. I infer the brittle ductile transition zone in the Dolpo region to be ~40 km wide which is consistent with previous estimates

based on geodetic observations. I interpret the transition zone to extend from the southern limb of the Dolpo anticline to the northern belt of microseismicity (Figure 1.7). In this view, the accumulation of strain in the lower crust beneath the Dolpo anticline results in a buildup of elastic stress thereby loading the seismogenic portion of the MHT and facilitating the triggering of seismicity (Figure 1.7).

Geodetic analysis of the interseismic strain field (Ader et al., 2012) in western Nepal suggests that the MHT is locked from where it daylights at the range front to possibly the northern cluster (belt) of microseismicity, while aseismic creep has continued beneath the hinterland of the thrust wedge. Figure 1.7 shows our interpretation of the rheologic change along the MHT. It is modified from a fault model simulation by Perfettini and Avouac (2004). The rheology along the MHT is represented by a spring and slider system consisting of three slider blocks that schematically show how stress is transferred from the downdip ductile region in the hinterland to the shallow seismogenic zone at the range front. Slider 1 represents the ductile portion of the MHT. Slider 2 represents the portion of the MHT that lies within the brittle-ductile transition and slider 3 represents the seismogenic portion of the MHT.

1.7 Conclusions

The presence of localized rapid rock uplift over (at least) the last 10^4-10^5 years coincident with the Dolpo anticline, rapid interseismic strain accumulation, and the inferred rupture area of the Mw 8.2 - 9.0 AD 1505 earthquake, depict a region undergoing continuous aseismic to microseismic deformation punctuated by large earthquakes. An active regional structure at the plateau's southern margin implies that locally not all of the strain imparted by the southward creep of Tibet is elastic, suggesting that elastic strain deficits for the Himalaya may not be as large as predicted, and recurrence intervals may be longer. Seismotectonic models of central Nepal where the regional map pattern and microseismicity are relatively simple do not apply in western Nepal where regional geology, microseismicity, and patterns of rock uplift provide evidence for duplexing beneath both the Lesser Himalaya and the High Himalaya.

1.8 References

Ader, T., Avouac, J.P., Liu-Zeng, J., Lyon-Caen, H., Bollinger, L., Galetzka, J., Genrich, J., Thomas, M., Chanard, K., and Sapkota, S.N., 2012, Convergence rate across the Nepal Himalaya and interseismic coupling on the Main Himalayan Thrust: Implications for seismic hazard: Journal of Geophysical Research: Solid Earth (1978–2012), v. 117, p. B04403.

Ambraseys, N., and Jackson, D., 2003, A note on early earthquakes in northern India and southern Tibet: Current Science, v. 84, p. 570-582.

Bilham, R., and Ambraseys, N., 2005, Apparent Himalayan slip deficit from the summation of seismic moments for Himalayan earthquakes, 1500–2000: Current Science, v. 88, p. 1658-1663.

Bilham, R., Bodin, P., and Jackson, M., 1995, Entertaining a great earthquake in Western Nepal: Historic inactivity and geodetic tests for the present state of strain: Journal of Nepal Geological Society, v. 11, p. 73-78.

Bilham, R., Gaur, V.K., and Molnar, P., 2001, Himalayan seismic hazard: Science(Washington), v. 293, p. 1442-1444.

Bilham, R., Larson, K., Freymueller, J., Jouanne, F., Le Fort, P., Leturmy, P., Mugnier, J., Gamond, J., Glot, J., and Martinod, J., 1997, GPS measurements of present-day convergence across the Nepal Himalaya: Nature, v. 386, p. 61-64.

Bollinger, L., Avouac, J., Beyssac, O., Catlos, E., Harrison, T., Grove, M., Goffé, B., and Sapkota, S., 2004, Thermal structure and exhumation history of the Lesser Himalaya in central Nepal: Tectonics, v. 23, p. TC5015.

Bollinger, L., Perrier, F., Avouac, J.P., Sapkota, S., Gautam, U., and Tiwari, D., 2007, Seasonal modulation of seismicity in the Himalaya of Nepal: Geophysical research letters, v. 34, p. L08304.

Bookhagen, B., and Burbank, D.W., 2006, Topography, relief, and TRMM-derived rainfall variations along the Himalaya: Geophysical research letters, v. 33, p. L08405.

Burchfiel, B.C., Zhiliang, C., Hodges, K.V., Yuping, L., Royden, L.H., and Changrong, D., 1992, The South Tibetan detachment system, Himalayan orogen: Extension contemporaneous with and parallel to shortening in a collisional mountain belt, Geological Society of America Special Papers, v. 269, p. 1-41.

Caldwell, W.B., Klemperer, S.L., Lawrence, J.F., and Rai, S.S., 2013, Characterizing the Main Himalayan Thrust in the Garhwal Himalaya, India with receiver function CCP stacking: Earth and Planetary Science Letters, v. 367, p. 15-27.

Carosi, R., Montomoli, C., and Visona, D., 2007, A structural transect in the Lower Dolpo: Insights on the tectonic evolution of Western Nepal: Journal of Asian Earth Sciences, v. 29, p. 407-423.

Cattin, R., and Avouac, J., 2000, Modeling mountain building and the seismic cycle in the Himalaya of Nepal: Journal of Geophysical Research: Solid Earth (1978–2012), v. 105, p. 13389-13407.

Colchen, M., Fort, M., and Freytet, P., 1980, Evolution paléogéographique et structurale du fossé de la Thakkhola-Mustang (Himalaya du Népal): Implications sur l'histoire récente de la chaîne himalayenne: Paris: Comptes Rendus des Académie des Sciences, v. 290, p. 311-314.

Coleman, M., and Hodges, K., 1995, Evidence for Tibetan plateau uplift before 14 Myr ago from a new minimum age for east-west extension: Nature, v. 374, p. 49-52.

Davis, W., 1902, Baselevel, grade and peneplain: The Journal of Geology, v. 10, p. 77-111.

Feldl, N., and Bilham, R., 2006, Great Himalayan earthquakes and the Tibetan plateau: Nature, v. 444, p. 165-170.

Fuchs, G., 1973, On the geology of the Karnali and Dolpo regions, West Nepal: Mitteilungen der Geologischen Gesellschaft in Wien, 66, v. 67, p. 21-32.

Garzione, C.N., DeCelles, P.G., Hodkinson, D.G., Ojha, T.P., and Upreti, B.N., 2003, East-west extension and Miocene environmental change in the southern Tibetan plateau: Thakkhola graben, central Nepal: Geological Society of America Bulletin, v. 115, no. 1, p. 3-20.

Gilbert, G.K., and Dutton, C.E., 1877, Report on the Geology of the Henry Mountains, Govt. print. off.

Godin, L., Gleeson, T., Searle, M., Ullrich, T., and Parrish, R.R., 2006a, Locking of southward extrusion in favour of rapid crustal-scale buckling of the Greater Himalayan sequence, Nar valley, central Nepal: Geological Society, London, Special Publications, v. 268, p. 269-292.

Godin, L., Grujic, D., Law, R., and Searle, M., 2006b, Channel flow, ductile extrusion and exhumation in continental collision zones: an introduction: Geological Society, London, Special Publications, v. 268, p. 1-23.

Grandin, R., Doin, M.-P., Bollinger, L., Pinel-Puysségur, B., Ducret, G., Jolivet, R., and Sapkota, S.N., 2012, Long-term growth of the Himalaya inferred from interseismic InSAR measurement: Geology, v. 40, p. 1059-1062.

Hack, J.T., 1957, Studies of Longitudinal Stream Profiles in Virginia and Maryland, U.S. Government Printing Office.

Harrison, M.T., Grove, M., Mckeegan, K.D., Coath, C., Lovera, O.M., and Le Fort, P., 1999, Origin and episodic emplacement of the Manaslu intrusive complex, central Himalaya: Journal of Petrology, v. 40, p. 3-19.

Herman, F., Copeland, P., Avouac, J.-P., Bollinger, L., Mahéo, G., Le Fort, P., Rai, S., Foster, D., Pêcher, A., and Stüwe, K., 2010, Exhumation, crustal deformation, and thermal structure of the Nepal Himalaya derived from the inversion of thermochronological and thermobarometric data and modeling of the topography: Journal of Geophysical Research, v. 115, p. B06407.

Hodges, K.V., Wobus, C., Ruhl, K., Schildgen, T., and Whipple, K., 2004, Quaternary deformation, river steepening, and heavy precipitation at the front of the Higher Himalayan ranges: Earth and Planetary Science Letters, v. 220, p. 379-389.

Huc, M., Hassani, R., and Chéry, J., 1998, Large earthquake nucleation associated with stress exchange between middle and upper crust: Geophysical Research Letters, v. 25, p. 551-554.

Huntington, K.W., Blythe, A.E., and Hodges, K.V., 2006, Climate change and Late Pliocene acceleration of erosion in the Himalaya: Earth and Planetary Science Letters, v. 252, p. 107-118.

Jessup, M., Law, R., Searle, M., and Hubbard, M., 2006, Structural evolution and vorticity of flow during extrusion and exhumation of the Greater Himalayan Slab, Mount Everest Massif, Tibet/Nepal: implications for orogen-scale flow partitioning: Geological Society, London, Special Publications, v. 268, p. 379.

Jouanne, F., Mugnier, J.-L., Gamond, J., Fort, P.L., Pandey, M., Bollinger, L., Flouzat, M., and Avouac, J., 2004, Current shortening across the Himalayas of Nepal: Geophysical Journal International, v. 157, p. 1-14.

Kirby, E., and Ouimet, W., 2011, Tectonic geomorphology along the eastern margin of Tibet: Insights into the pattern and processes of active deformation adjacent to the Sichuan Basin: Geological Society, London, Special Publications, v. 353, p. 165-188.

Kirby, E., and Whipple, K., 2001, Quantifying differential rock-uplift rates via stream profile analysis: Geology, v. 29, p. 415-418.

Kirby, E., and Whipple, K.X., 2012, Expression of active tectonics in erosional landscapes: Journal of Structural Geology, v. 44, p. 54-75.

Kirby, E., Whipple, K.X., Tang, W., and Chen, Z., 2003, Distribution of active rock uplift along the eastern margin of the Tibetan Plateau: Inferences

from bedrock channel longitudinal profiles: Journal of Geophysical Research, v. 108, p. 2217.

Kumar, S., Wesnousky, S.G., Rockwell, T.K., Briggs, R.W., Thakur, V.C., and Jayangondaperumal, R., 2006, Paleoseismic evidence of great surface rupture earthquakes along the Indian Himalaya: Journal of Geophysical Research: Solid Earth (1978–2012), v. 111, p. B03304.

Lavé, J., and Avouac, J., 2001, Fluvial incision and tectonic uplift across the Himalayas of central Nepal: Journal of Geophysical Research: Solid Earth (1978–2012), v. 106, p. 26561-26591.

Le Fort, P., France-Lanord, C., 1995, Granites from Mustang and the Surrounding Regions (Central Nepal): Journal of Nepal Geological Society, v. 11, p. 5.

Mackin, J.H., 1948, Concept of the graded river: Geological Society of America Bulletin, v. 59, p. 463-512.

McDermott, J.A., Whipple, K.X., Hodges, K.V., and Soest, M.C., 2013, Evidence for Plio-Pleistocene north-south extension at the southern margin of the Tibetan Plateau, Nyalam region: Tectonics, v. 32, no. 3, p. 317-333.

Meade, B.J., 2010, The signature of an unbalanced earthquake cycle in Himalayan topography?: Geology, v. 38, p. 987-990.

Murphy, M., and Harrison, T.M., 1999, Relationship between leucogranites and the Qomolangma detachment in the Rongbuk Valley, south Tibet: Geology, v. 27, p. 831-834.

Murphy, M., Taylor, M., Gosse, J., Silver, C., Whipp, D., and Beaumont, C., 2014, Limit of strain partitioning in the Himalaya marked by large earthquakes in western Nepal: Nature Geoscience, v. 7, p. 38-42.

Murphy, M.A., 2007, Isotopic characteristics of the Gurla Mandhata metamorphic core complex: Implications for the architecture of the Himalayan orogen: Geology, v. 35, p. 983-986.

Ouimet, W.B., Whipple, K.X., and Granger, D.E., 2009, Beyond threshold hillslopes: Channel adjustment to base-level fall in tectonically active mountain ranges: Geology, v. 37, p. 579-582.

Pandey, M., Tandukar, R., Avouac, J., Lave, J., and Massot, J., 1995, Interseismic strain accumulation on the Himalayan crustal ramp (Nepal): Geophysical Research Letters, v. 22, p. 751-754.

Pandey, M., Tandukar, R., Avouac, J., Vergne, J., and Héritier, T., 1999, Seismotectonics of the Nepal Himalaya from a local seismic network: Journal of Asian Earth Sciences, v. 17, p. 703-712.

Perfettini, H., and Avouac, J.P., 2004, Stress transfer and strain rate variations during the seismic cycle: Journal of Geophysical Research: Solid Earth (1978–2012), v. 109, p. B06402.

Robinson, D.M., 2008, Forward modeling the kinematic sequence of the central Himalayan thrust belt, western Nepal: Geosphere, v. 4, p. 785-801.

Sapkota, S.N., Bollinger, L., Klinger, Y., Tapponnier, P., Gaudemer, Y., and Tiwari, D., 2013, Primary surface ruptures of the great Himalayan earthquakes in 1934 and 1255: Nature Geoscience, v. 6, p. 71-76.

Schelling, D., and Arita, K., 1991, Thrust tectonics, crustal shortening, and the structure of the far-eastern Nepal Himalaya: Tectonics, v. 10, p. 851-862.

Searle, M., 1999, Emplacement of Himalayan leucogranites by magma injection along giant sill complexes: examples from the Cho Oyu, Gyachung Kang and Everest leucogranites (Nepal Himalaya): Journal of Asian Earth Sciences, v. 17, p. 773-783.

Searle, M.P., and Godin, L., 2003, The south Tibetan detachment and the Manaslu Leucogranite: A structural reinterpretation and restoration of the Annapurna-Manaslu Himalaya, Nepal: The Journal of Geology, v. 111, p. 505-523.

Seeber, L., and Gornitz, V., 1983, River profiles along the Himalayan arc as indicators of active tectonics: Tectonophysics, v. 92, p. 335-367.

Styron, R.H., Taylor, M.H., and Murphy, M.A., 2011, Oblique convergence, arc-parallel extension, and the role of strike-slip faulting in the High Himalaya: Geosphere, v. 7, p. 582-596.

Whipple, K.X., and Tucker, G.E., 1999, Dynamics of the stream-power river incision model: Implications for height limits of mountain ranges, landscape response timescales, and research needs: Journal of Geophysical Research: Solid Earth (1978–2012), v. 104, p. 17661-17674.

Wobus, C., Heimsath, A., Whipple, K., and Hodges, K., 2005, Active out-of-sequence thrust faulting in the central Nepalese Himalaya: Nature, v. 434, p. 1008-1011.

Wobus, C., Whipple, K.X., Kirby, E., Snyder, N., Johnson, J., Spyropolou, K., Crosby, B., and Sheehan, D., 2006, Tectonics from topography: Procedures, promise, and pitfalls: Special Papers-Geological Society of America, v. 398, p. 55.

Chapter 2 Segmentation of the Himalayan arc expressed in river channel steepness

2.1 Chapter Summary

I present a map of normalized river channel steepness (k_{sn}) - a proxy for rock uplift rate over 10^4-10^5 years, for the Himalayan arc, and generate correlation coefficients for k_{sn} and the degree of Main Himalayan Thrust (MHT) (India-Asia intracontinental subduction zone) fault coupling (-0.6), lithology (0.3), and average precipitation interpolated for the last 50 years (-0.1) (all p-values < 0.05). Based on this analysis, I interpret the pattern of Himalayan k_{sn} to be primarily a function of MHT coupling and use it to divide the range into segments based on the distribution of clusters of high k_{sn} rivers. From west-to-east the segments are: Himachal Pradesh, Uttarakhand, west Nepal, central Nepal, east Nepal, Bhutan, and Arunachal Pradesh. Along the length of the Himalaya, high k_{sn} clusters are located immediately north of the strongly coupled portion of the MHT, where the behavior of the fault changes from seismogenic to sliding at the rheologic brittle-to-plastic transition (BPT). I propose that the India-Asia BPT is located along a series of thrust ramps marked at the surface by clusters of high k_{sn} rivers, and offset from each other across Hima-Tibetan rifts, requiring intervening lateral ramps. The ability of a particular segment to rupture the plate boundary is related

to two parameters – the width of the high k_{sn} cluster and its distance from the leading edge of the thrust wedge.

This segmentation reveals a correspondence with the historical record of great earthquakes in the west Nepal, central Nepal, and Bhutan segments. The Mw 7.6 April 25, 2015 Gorkha earthquake was the third Mw > 7 event in 300 years within this segment. West Nepal has not ruptured since 1505, and Bhutan (excluding Shillong plateau) since 1713, implying either great earthquakes are missing from the historical record, or the seismic cycle in central Nepal is shorter than adjacent segments.

2.2 Introduction

The Himalayan thrust wedge is 2500 km long, 250 km wide, and up to 50 km thick below southern Tibet (Nábělek et al., 2009) (Figure 2.1). The wedge is floored by an intracontinental thrust fault separating India from Asia known as the Main Himalayan Thrust (MHT), which goes from an aseismically sliding decollment beneath southern Tibet to the Himalayan Seismogenic Zone at the brittle-plastic transition (BPT) beneath the High Himalaya (Bilham et al., 2001; Ader et al., 2012; Stevens and Avouac, 2015). The BPT corresponds to the boundary between the strongly coupled portion of the MHT and the weakly coupled portion delineated by Stevens and Avouac (2015) (Figure 2.2a). The MHT's surface trace manifests itself in a series of thrust-related folds and faults at

the toe of the wedge which form the first topographic expression of the Himalaya, and are collectively known as the Main Frontal Thrust (MFT) (Figure 2.1). The folding rate for anticlines in central Nepal, documented by offset river terraces (Lavé and Avouac, 2001), is within uncertainty of the rate of aseismic sliding recorded by GPS stations in south-central Tibet (Ader et al., 2012; Bilham et al., 2001; Bilham et al., 1997; Jackson and Bilham, 1994). This observation suggests the wedge does not deform internally implying that rock uplift within the wedge is a passive product of fluxing material over ramps in the MHT (Cattin and Avouac, 2000; Pandey et al., 1995). However, the suggestion of an entirely passive wedge is at odds with observations. Recent work has highlighted that the 1505 quake in west Nepal ruptured multiple splays (West Nepal Fault, Main Boundary Thrust) within the wedge (Hossler et al., 2016; Murphy et al., 2014), and Quaternary thrust faulting at the base of the High Himalaya has been suggested on the basis of field observations and thermochronology (Hodges et al., 2004; Wobus et al., 2005). Thermal models and structural restorations of the frontal portion of the wedge suggest that underplating of Indian crust along a foreland migrating ramp is consistent with the Late Miocene to recent thermokinematic history (Bollinger et al., 2004a; Herman et al., 2010; McQuarrie and Ehlers, 2015; Robinson, 2008). GPS measurements show the most rapid interseismic strain rate is located at, or north of the 3500 m topographic contour (Ader et al. 2012; Bilham et al., 2001). A GPS based model of the degree of MHT coupling (Stevens and Avouac, 2015) reveals a similar result which I used

to generate correlation coefficients with Himalayan normalized river-channel steepness (k_{sn}) (Figure 2.2b). k_{sn} is a proxy for relative rock-uplift rate over 10^4-10^5 years (Kirby and Whipple; 2001; Kirby and Whipple, 2012), and my analysis documents clusters of high k_{sn} rivers, most of which straddle the boundary between the strongly coupled and weakly coupled portions of the MHT (Stevens and Avouac, 2015) (Figure 2.2c), which I interpret to be coincident with the BPT. The MHT BPT is a mechanical boundary whose location is a function of temperature, it begins where the subduction interface encounters the 350 °C isotherm (Herman et al., 2010) at which point quartz begins to behave ductiley (Hirth and Tullis, 1992). The percentage of deformation accommodated by crystal plastic creep increases with temperature as the dominant mineral constituents began to deform plastically (feldspar begins to deform ductiley at 600 °C) (Tullis and Yund, 1992). The width of the MHT BPT depends on the geothermal gradient and the local dip of the MHT. The portion of the thrust wedge north of the BPT acts as a dashpot storing strain until it overcomes static friction on the fully coupled portion of the MHT generating a great earthquake (Avouac, 2003; Cannon and Murphy, 2014). Some amount of this strain must be permanent since rapid interseismic strain recorded by GPS is collocated with the highest topography, and clusters of high k_{sn} rivers; the percentage released in earthquakes versus absorbed by shortening structures remains uncertain (Bilham and Ambraseys, 2005; Cannon and Murphy, 2014; Meade, 2010; Stevens and Avouac, 2015).

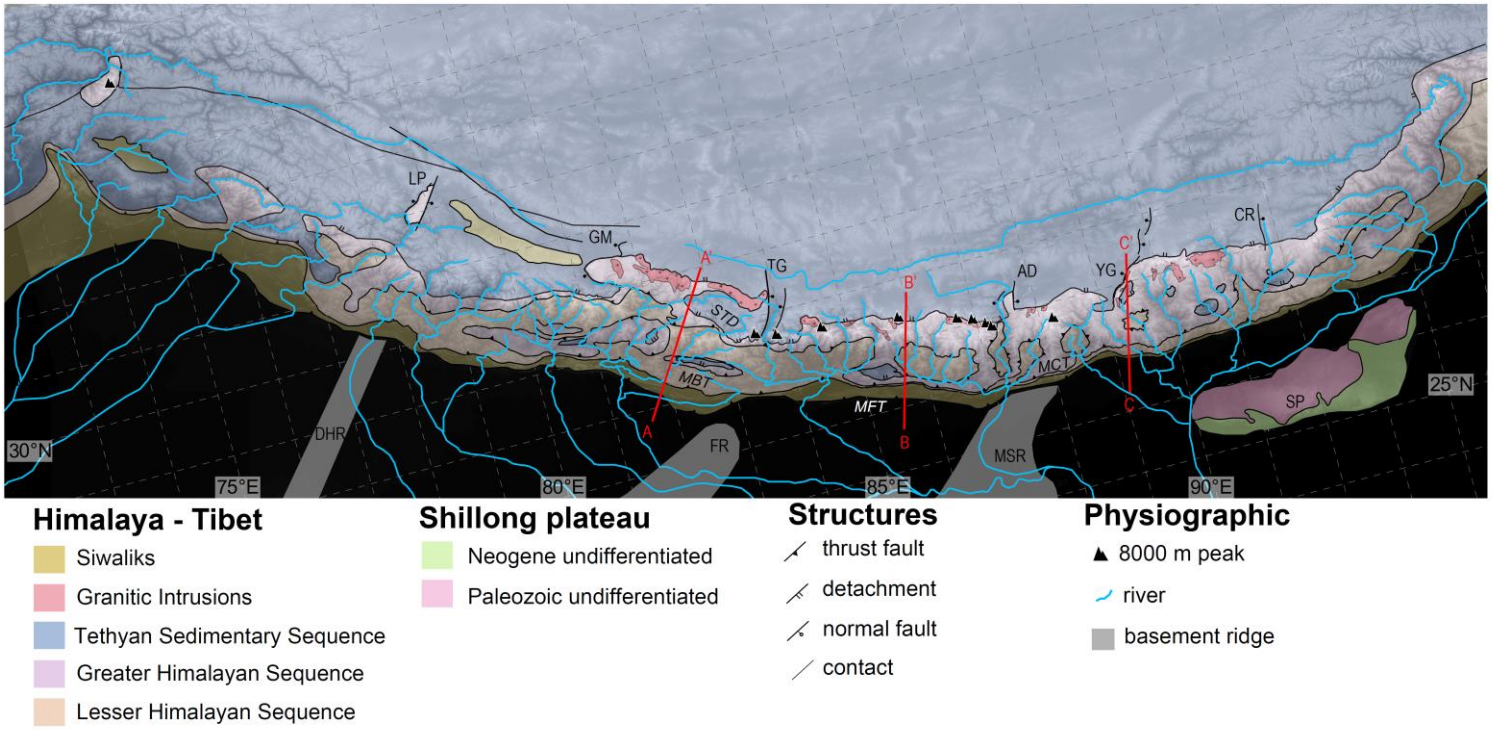

Figure 2.1. a) Digital elevation map of the Himalaya with major rivers, 8000 m peaks, and bedrock geology. Gray polygons are Indian basement ridges after Gahalaut and Kundu 2012 DHR = Delhi-Hardwar ridge, FR = Faizabad ridge, MSR = Munger-Saharsa ridge. Tibetan rifts AD = Ama Drime, CR = Coma rift, GM = Gurla Mandhata, LP = Leo Pargil, TG = Thakhola graben, YG = Yadong Gulu rift. SP = Shillong plateau.

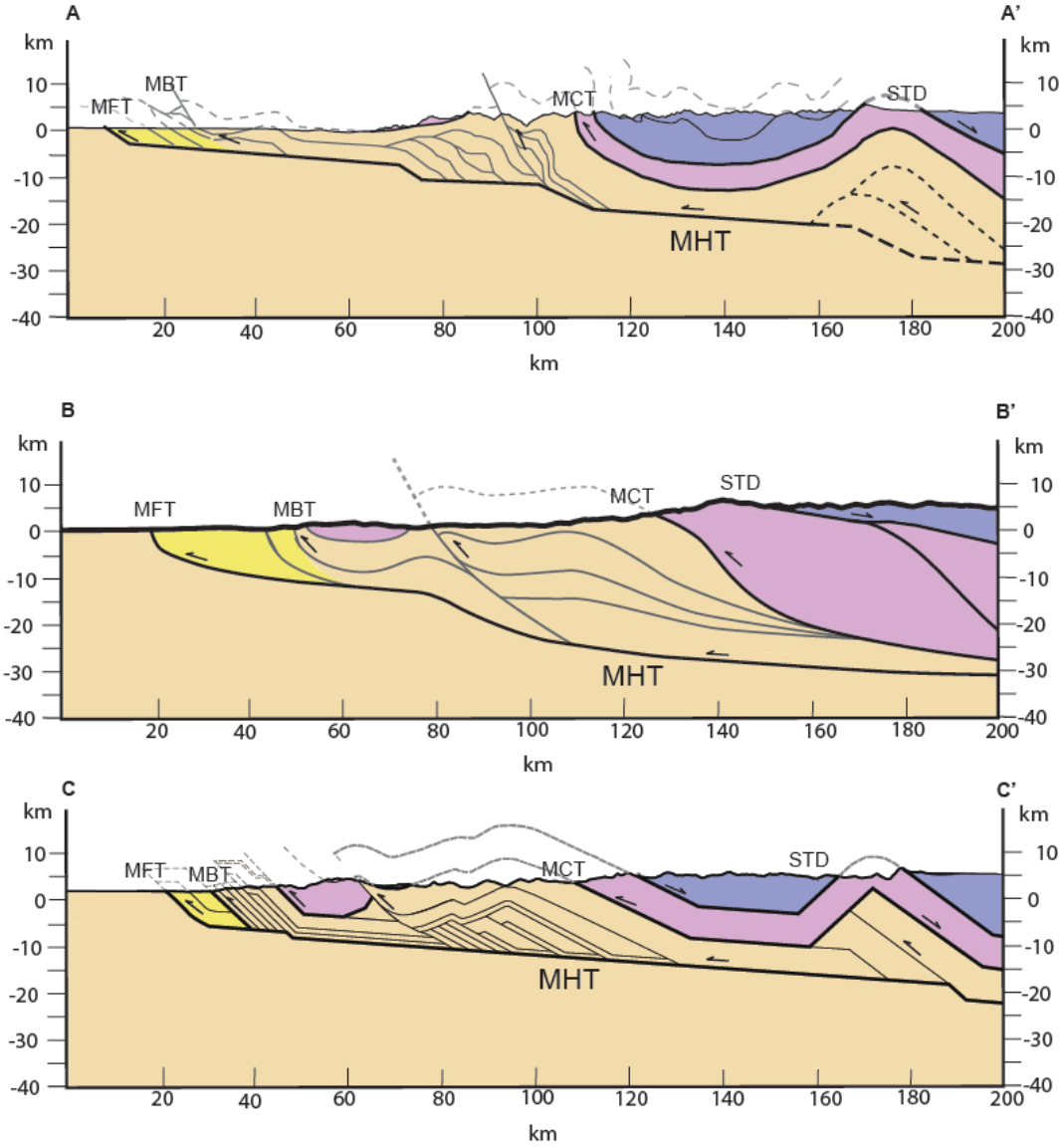

Figure 2.1. b) Geologic cross sections after Cannon and Murphy 2014, Bollinger et al. 2004, McQuarrie et al. 2014. See a.) for cross section locations. MHT = Main Himalayan Thrust, MFT = Main Frontal Thrust, MBT = Main Boundary Thrust, MCT = Main Central Thrust, STD = South Tibetan Detachment.

A record of Himalayan strain accumulation is encoded in the landscape through a competition between erosion and rock uplift. Currently, high

topography (Figure 2.1), high k_{sn} rivers (Figure 2.2b), interseismic strain (Ader et al., 2012; Bilham et al., 2001; Stevens and Avouac, 2015), belts of microseismicity (Figure 3a) (Bollinger et al., 2007; Pandey et al., 1995; Pandey et al., 1999), and MHT ramps interpreted from geologic mapping (Figure 2.1 cross sections), coincide with the inferred MHT BPT (Figure 2.3b and 2.3c) (Bilham et al., 2001; Herman et al. 2010; Cannon and Murphy; 2014) which marks the northern limit of the strongly coupled portion of the plate boundary (Figure 2.2a) (Stevens and Avouac, 2015). This suggests that the topography of the high Himalaya is in steady state over hundred thousand year timescales, and that it is a function of subduction interface geometry and plate boundary thermal structure. The strong negative correlation ($r = -0.6$, p-value < 0.005) between k_{sn} and MHT coupling suggests that clusters of high k_{sn} rivers can be interpreted to reflect where strain is accumulating within the thrust wedge.

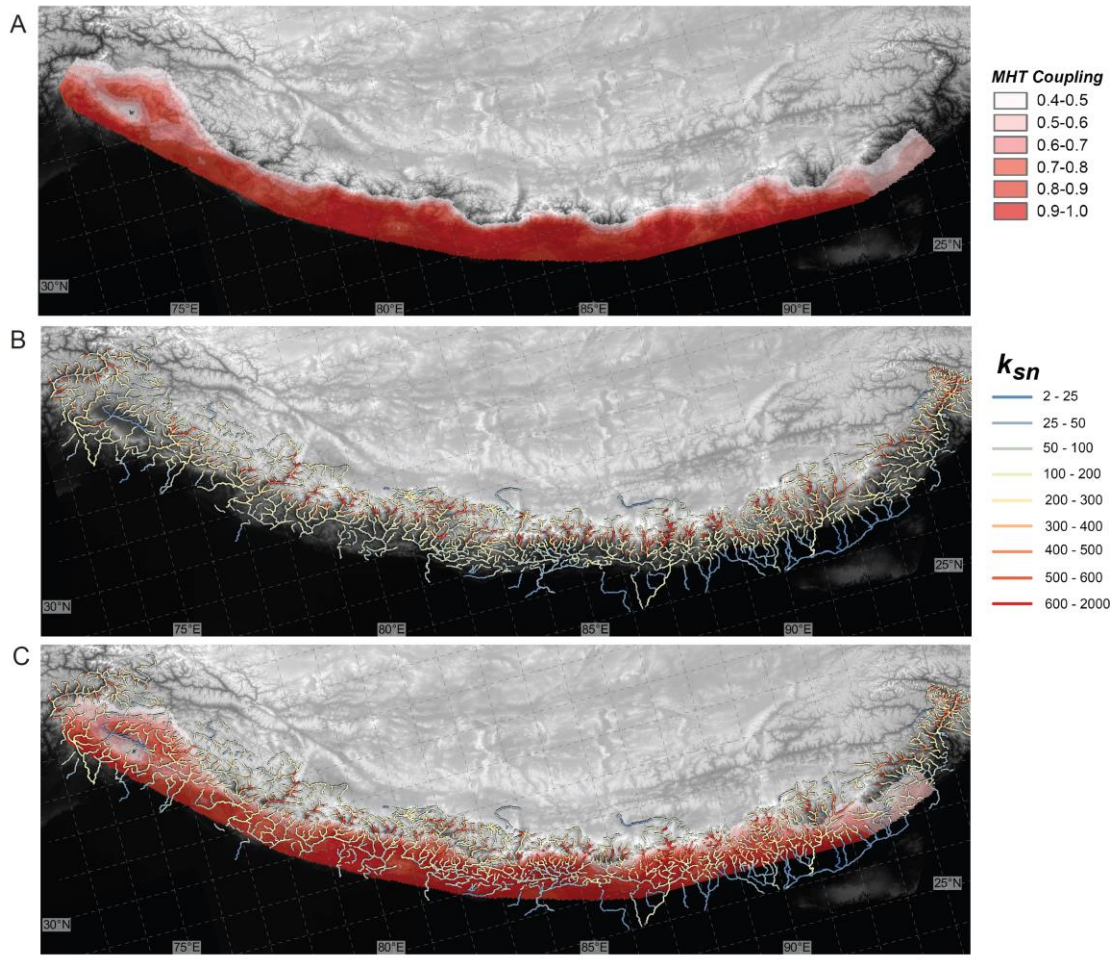

Figure 2.2. a) Map of Main Himalayan Thrust (MHT) fault coupling from Stevens and Avouac (2015). b) Map of Himalayan river channel steepness (k_{sn}). c) MHT coupling with k_{sn} overlaid.

2.3 Background

The striking orogen-parallel continuity of Himalayan lithotectonic stratigraphy (Figure 2.1) prompted the application of theories developed from one part of the range (typically central Nepal) to be used to explain the behavior of the

entire system. However, as research expanded across the mountain range geoscientists have been confronted by an array of kinematic and erosional behaviors not consistent with any particular model of the emplacement of the high grade metamorphic core of the orogen, the Greater Himalayan Sequence (GHS) (Figure 2.1), i.e. channel flow, extrusion, or tectonic wedging. My orogen scale investigation of modern relative rock-uplift rates (k_{sn} analysis) reveals that rock-uplift rates are not homogenous across the range, or by inference, throughout the history of the Himalaya. The surface bedrock geology of the High Himalaya in central Nepal is largely the result of emplacement of the metamorphic core of the orogen between the Main Central Thrust (MCT) and the South Tibetan Detachment (STD) (Figure 2.1) during the Early Miocene. These structures maintain a low degree of activity today (Hodges et al., 2004; McDermott et al., 2013; Wobus et al., 2005), however, no recent surface ruptures have been found, and cooling histories and channel steepness datasets have been variously interpreted to represent out-of-sequence faulting, duplexing, or passive uplift over MHT ramps (Pandey et al., 1995; Cattin and Avouac, 2000; Avouac, 2003; Bollinger et al., 2004a; Wobus et al., 2005; Herman et al., 2010; McDermott et al., 2013; McDermott et al., 2015). In west Nepal, the STD is folded (Figure 2.1) and defines the Dolpo anticline, a regional anticline with at least 9 km of structural relief (Cannon and Murphy, 2014) whose frontal limb coincides with a cluster of high k_{sn} channels interpreted to overlie the BPT in west Nepal. Folding initiated after the cessation of STD motion, regionally constrained to 16-19 Ma

(Searle and Godin, 2003; Godin et al., 2006b). The concentration of high k_{sn} rivers and young zircon U-Th/He ages (8.0 $\pm$ 1.3 to 2.6 Ma $\pm$ 0.7) (McCallister et al., 2014) at Gurla Mandhata-Humla (GMH) (a core complex which marks the western limit of the Dolpo anticline) suggests that hinterland folding was initiated in the Late Miocene and is ongoing today. In Bhutan, the STD was active from 23-16 Ma (Kellett et al., 2010) or 20.5-14 Ma (Cooper et al., 2015) and was folded into a broad anticline which spans the northern provinces of Punakha, Bumthang, and Kurtoed (Grujic et al., 2002; Long et al., 2011; McQuarrie et al., 2014). The anticline is collocated with the BPT interpreted from my k_{sn} data. The cooling history of northwest Bhutan using zircon and apatite [U-Th]/He found cooling events at 8-10 Ma (zircon) and 2-4 Ma (apatite) coincident with the Bhutan anticline (Cannon, 2011). The anticlines overlying the BPT of West Nepal and Bhutan, interpreted from k_{sn} data, share similar cooling histories and are both bound on one side by major extensional structures, the GMH core complex and the Chomolari detachment (Yadong-Gulu rift) (Murphy et al., 2002; Wu et al., 1998). In both cases, folding appears synchronous with the onset of extension, suggesting that the initiation of hinterland ductile duplexes is kinematically linked with thickening of the lower crust in a constructional-strain field (Sundell et al., 2013).

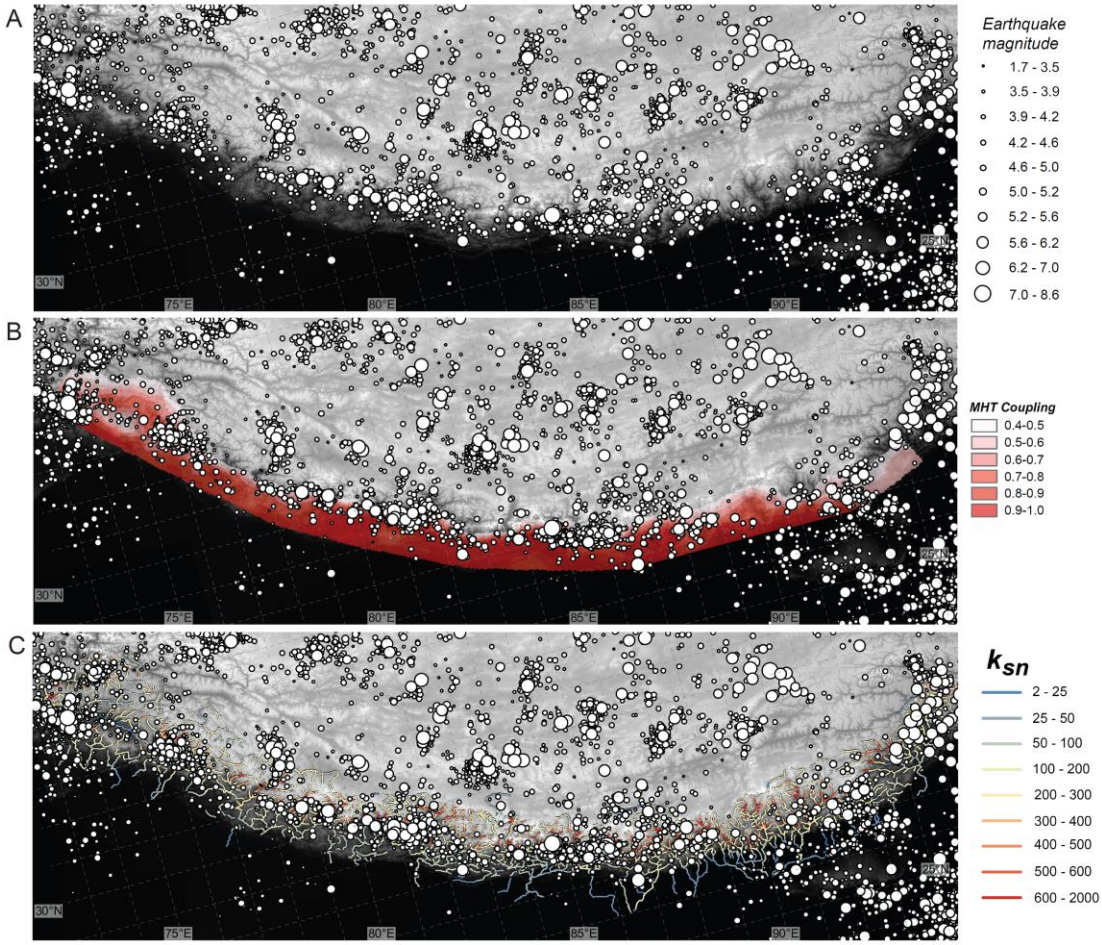

Figure 2.3. a) Map of Hima-Tibetan seismicity from 1973-2015 National Earthquake Information Center. b) Hima-Tibetan seismicity overlaid on MHT coupling. c) Hima-Tibetan seismicity overlaid on k_{sn}.

2.4 Methods

Normalized river-channel steepness k_{sn} analysis was conducted using the Advanced Spaceborne Thermal and Reflection Radiometer (ASTER) Global Digital Elevation Model V002 with 30 m resolution. I analyzed tributaries and trunk channels along the Himalayan arc from Himachal Pradesh to the Arunachal Pradesh (Figure 2.2b). k_{sn} analysis is founded on the observation that the

longitudinal profiles (elevation vs. downstream distance) of graded streams in steady-state are characterized by gentle concave up curves (Hack, 1957). In steady-state landscapes channel slope, width, and available discharge are balanced by the available stream power (Davis, 1902; Mackin, 1948) implying that the rate of erosion is equal to the rate of rock uplift. This relationship can be expressed using $S = k_{sn}A^{-\theta ref}$ (Kirby and Whipple, 2001; Wobus et al., 2006) in which S = slope, A = upstream drainage area, k_{sn} = normalized channel steepness, and θ_{ref} = reference concavity (0.45). Reaches of rivers with similar gradient are visually selected by the user in *Matlab* and subsequently plotted in *ArcGIS*. Deviations from steady-state longitudinal profiles can be produced by changes in rock uplift, changes in substrate erodibility, and climatic gradients so the results of the analysis must be evaluated for each of these forcing mechanisms.

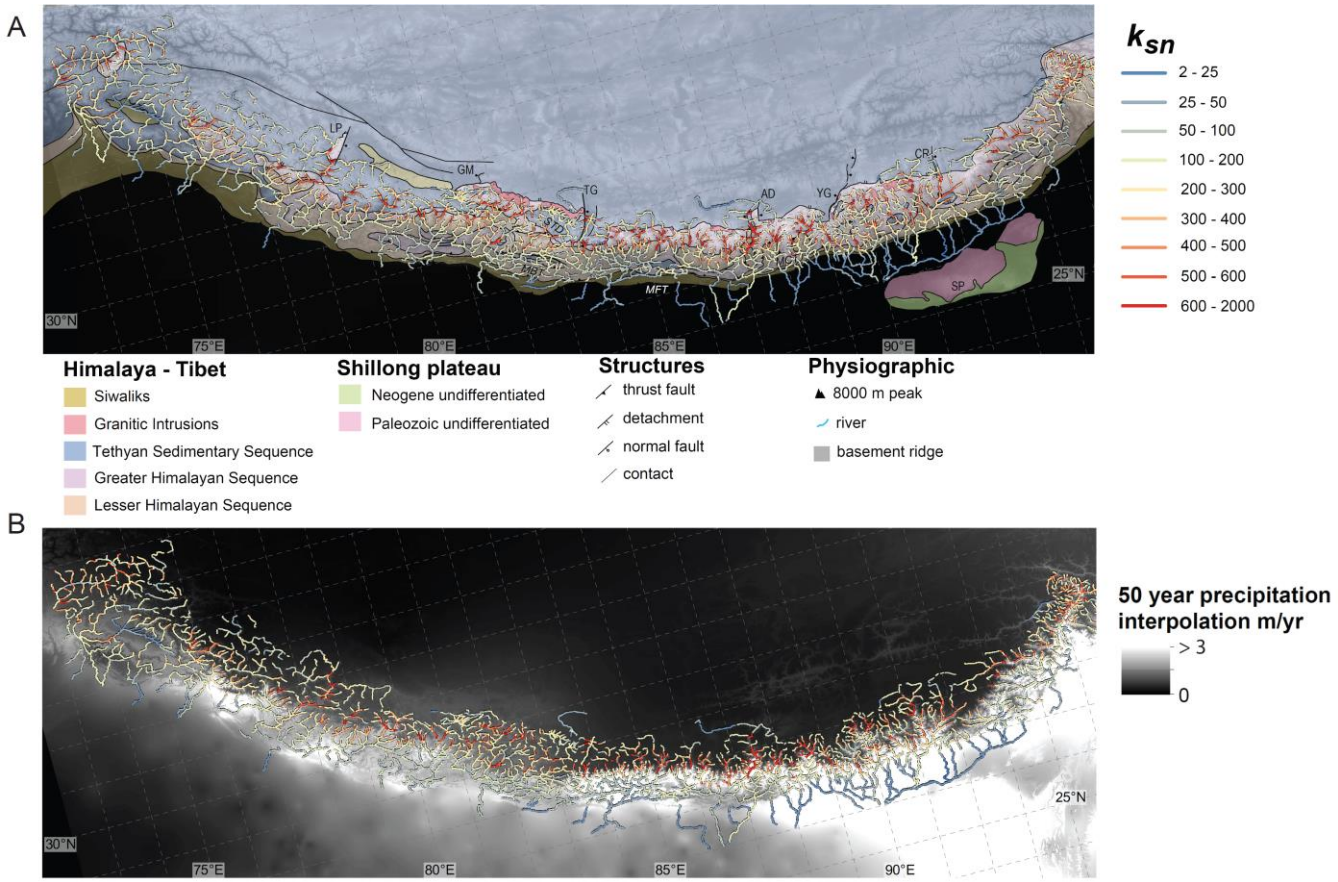

Figure 2.4. a) Map of Himalayan bedrock geology with k_{sn} overlaid. b) Interpolated map of 50 years of precipitation data (Hijmans et al., 2005) with k_{sn} overlaid.

To this end, I generated correlation coefficients for k_{sn} and MHT coupling (Figure 2.2c), lithology (Figure 2.4a), and a 50 year interpolation of precipitation data (Figure 2.4b) (Hijmans et al., 2015) using *ArcGIS* and *Microsoft Exel* (Fig 2.5a-n). k_{sn} is a vector dataset, to compare it quantitatively with MHT coupling, and precipitation required converting the individual vector shapefiles to a single raster file. I used the natural neighbors interpolation algorithm with a one kilometer grid (Figure 2.6). Data were then extracted from each dataset along the same profile using the *3D Analyst* toolbar interpolate line function, followed by the profile graph function, and then exporting the resuls to *Excel*. I normalized the values to 1, and generated correlation coefficients. Comparisons of k_{sn} with MHT coupling, and precipitation are straightforward using existing raster datasets and the method outlined above. However, there is no existing dataset for substrate erodibility which required me to use a proxy. I used lithology as a proxy for substrate erodibility and assigned an erodibility index to each of the five major Himalayan lithologies. The erodability index values were chosen to reflect the relative hardness of the lithologies in question, and were founded on the principle that harder, less erodible rocks maintain steeper river channels, while softer rocks support gentler channels. This principle can be observed in plateaus where a more resistant capstone protects a more erodible substrate beneath; the capstone supports vertical cliffs whereas the underlying substrate supports gentle slopes. The relative erodibility index values were chosen based on the average k_{sn} value for each lithology, e.g. k_{sn} in the Siwaliks was always lower than the Lesser

Himalaya Sequence (LHS), which was nearly always lower than the Greater Himalaya Sequence (GHS), and was similar to the Tethyan Sedimentary Sequence (TSS) (Figure 2.4a). While my assignment of erodibility index values was arbitrary, it did not affect the outcome of the analysis since correlation coefficients only track how one set of values change (positive or negative correlation) in relation to another without respect to what the exact values are. The erodability index values assigned are: Siwaliks 0.25 (poorly consolidated sandstones and conglomerates), the LHS 0.5 (low to medium grade metamorphic rocks), the GHS 0.75 (medium to high grade metamorphic rocks), the TSS 0.35 (low grade metamorphic to unmetamorphosed sedimentary rocks), and granitic intrusions 0.75. To characterize the relationship between k_{sn}, MHT coupling, substrate erodability, and precipitation, I analyzed four profiles spaced at 25 km intervals for 13 regions, from west-to-east they are: west Himachal Pradesh, east Himachal Pradesh, west Uttarakhand, east Uttarakhand, Doplo, west Nepal, west central Nepal, Kathmandu, Arun, east Nepal, east Bhutan, west Bhutan, and Arunachal Pradesh (Fig 5a-n). The results reported for the entire range (Table 1) are an average of all 13 regions.

A

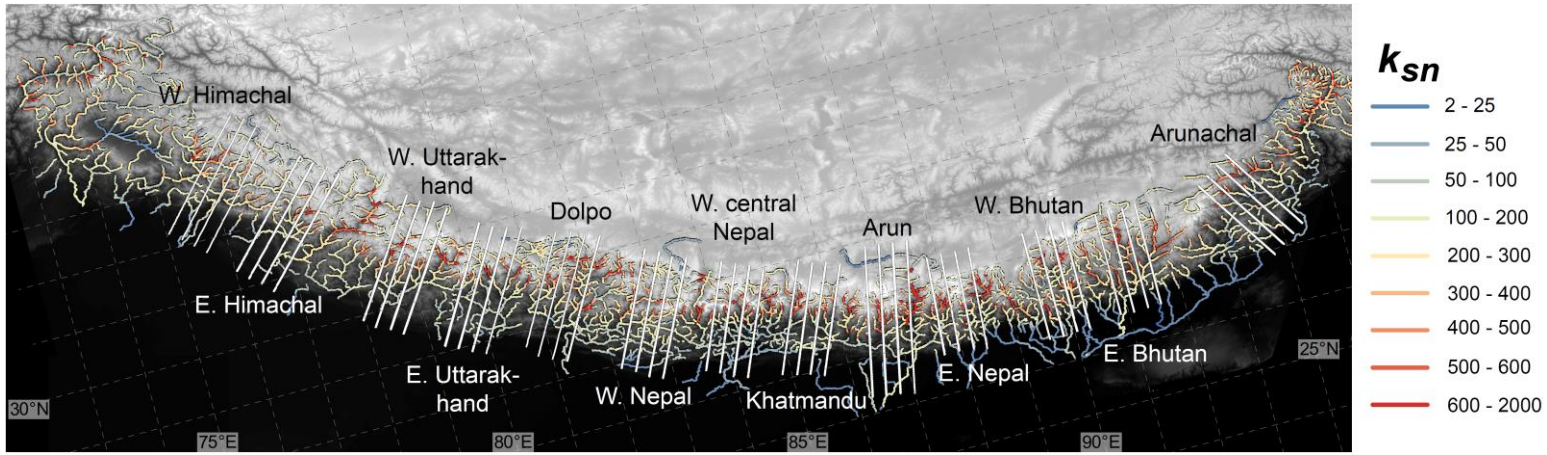

Figure 5a. Index map for comparison profiles in following sub-figures. Digital elevation map, overlain by ksn, and comparison profiles labelled by region.

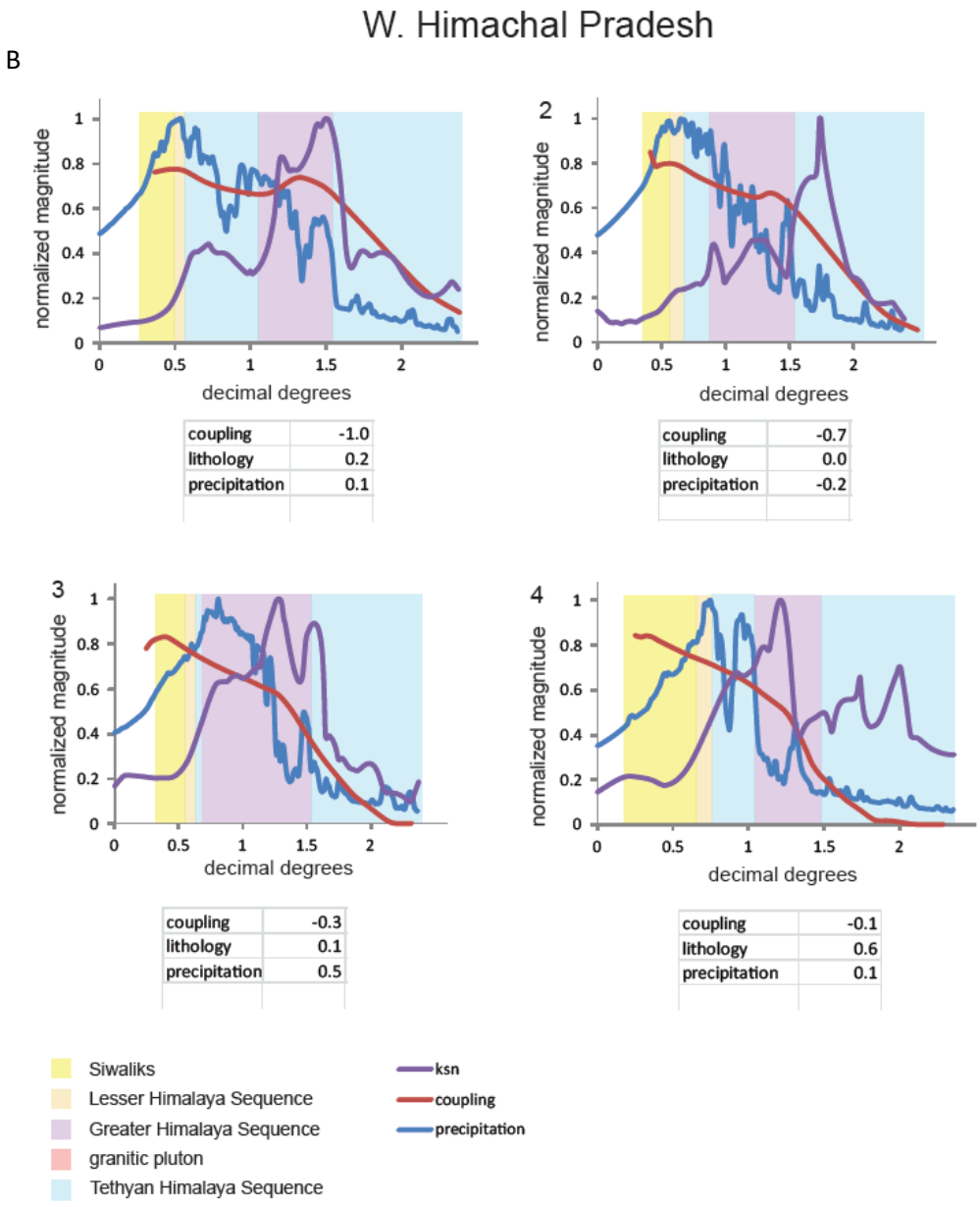

Figure 5b.1. West Himachal Pradesh comparison profiles 1-4 are plotted west-to-east on map in figure 5a and 5b.2. Correlation coefficients listed below each graph.

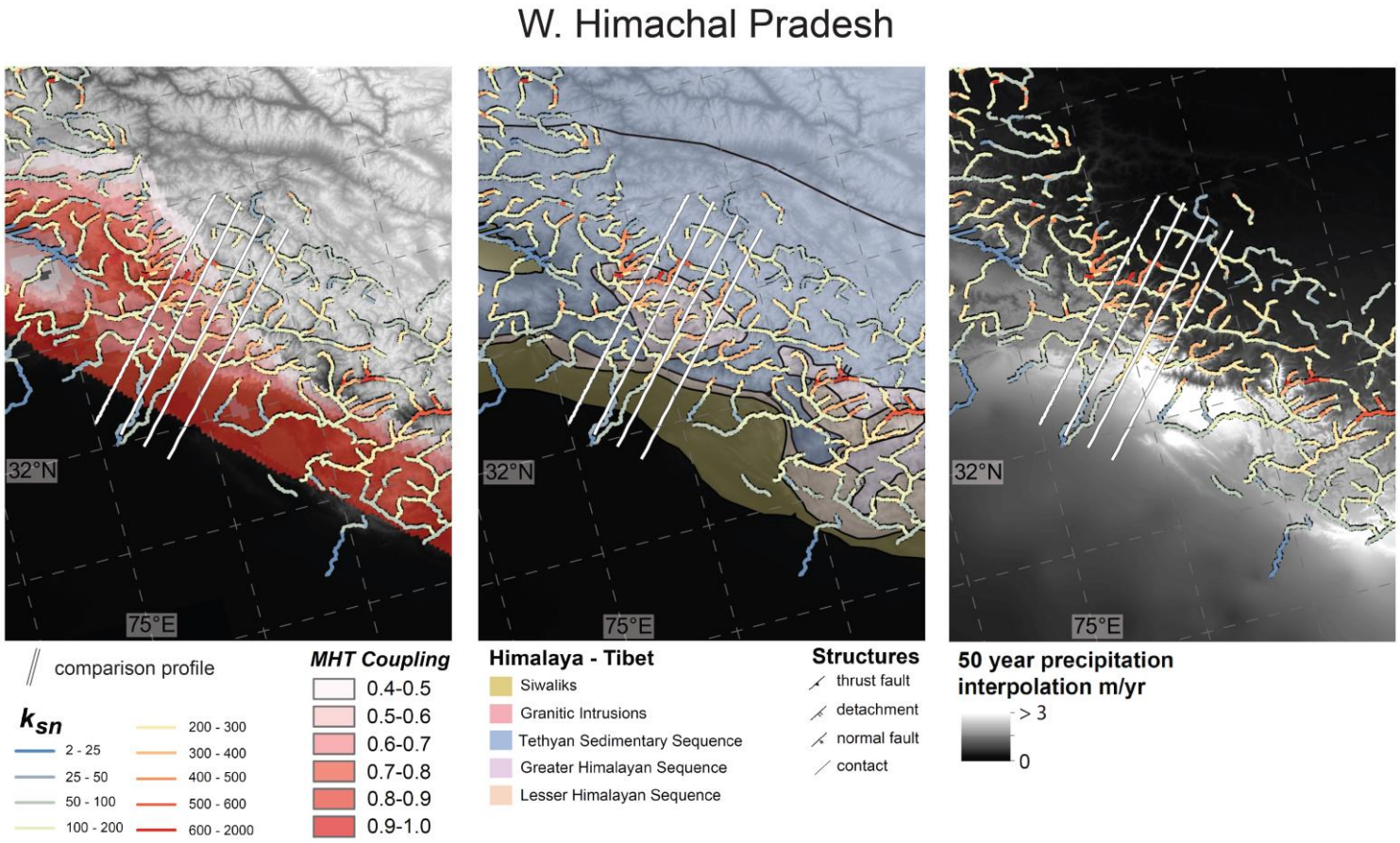

Figure 5b.2. West Himachal Pradesh comparison datasets and profiles 1- 4 (west-to-east). a) MHT coupling and k_{sn}, b) lithology and k_{sn}, c) 50 year precipitation interpolation (Hijmans et al., (2005) and k_{sn}..

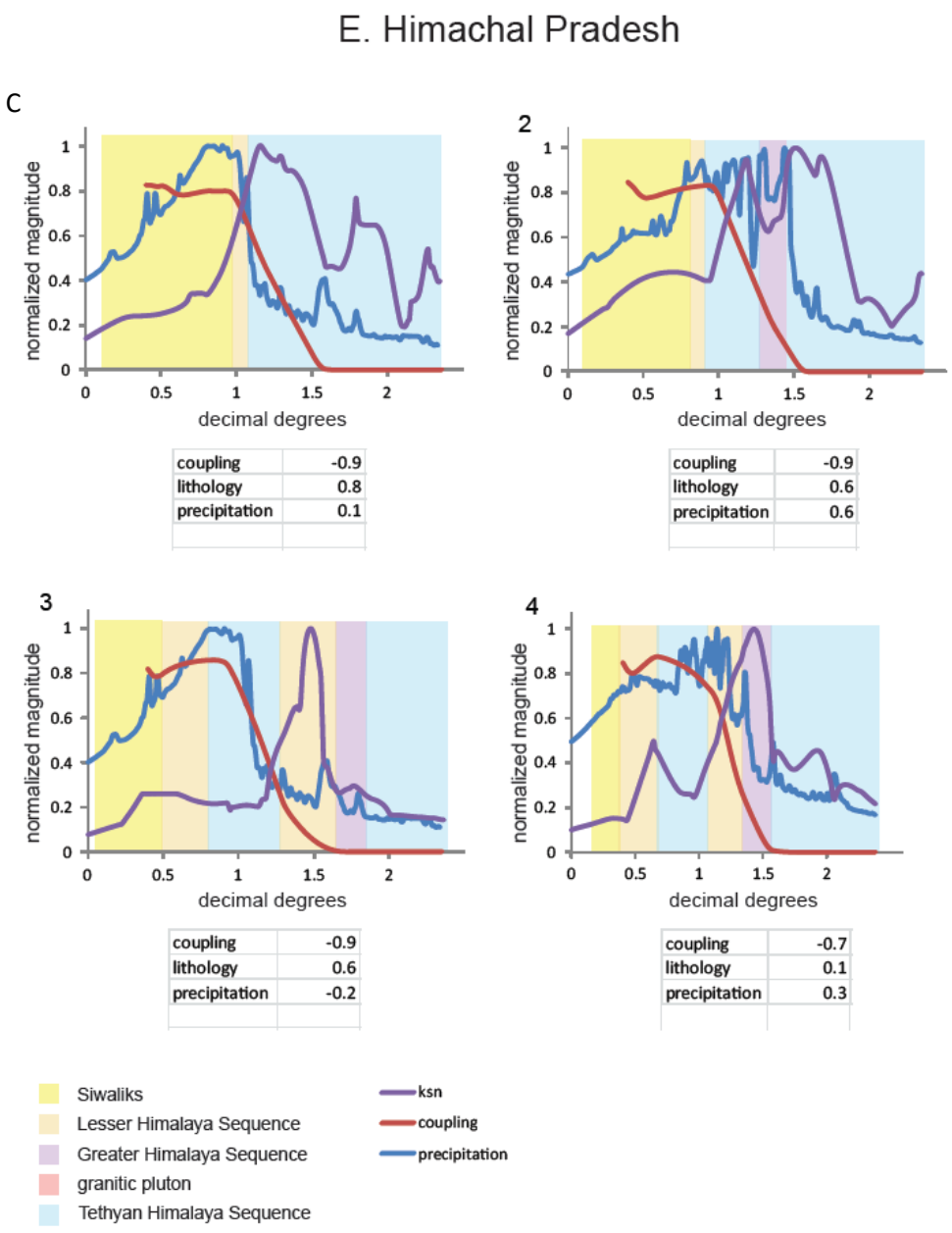

Figure 5c.1. East Himachal Pradesh comparison profiles 1-4 are plotted west-to-east on map in figure 5a and 5c.2. Correlation coefficients listed below each graph.

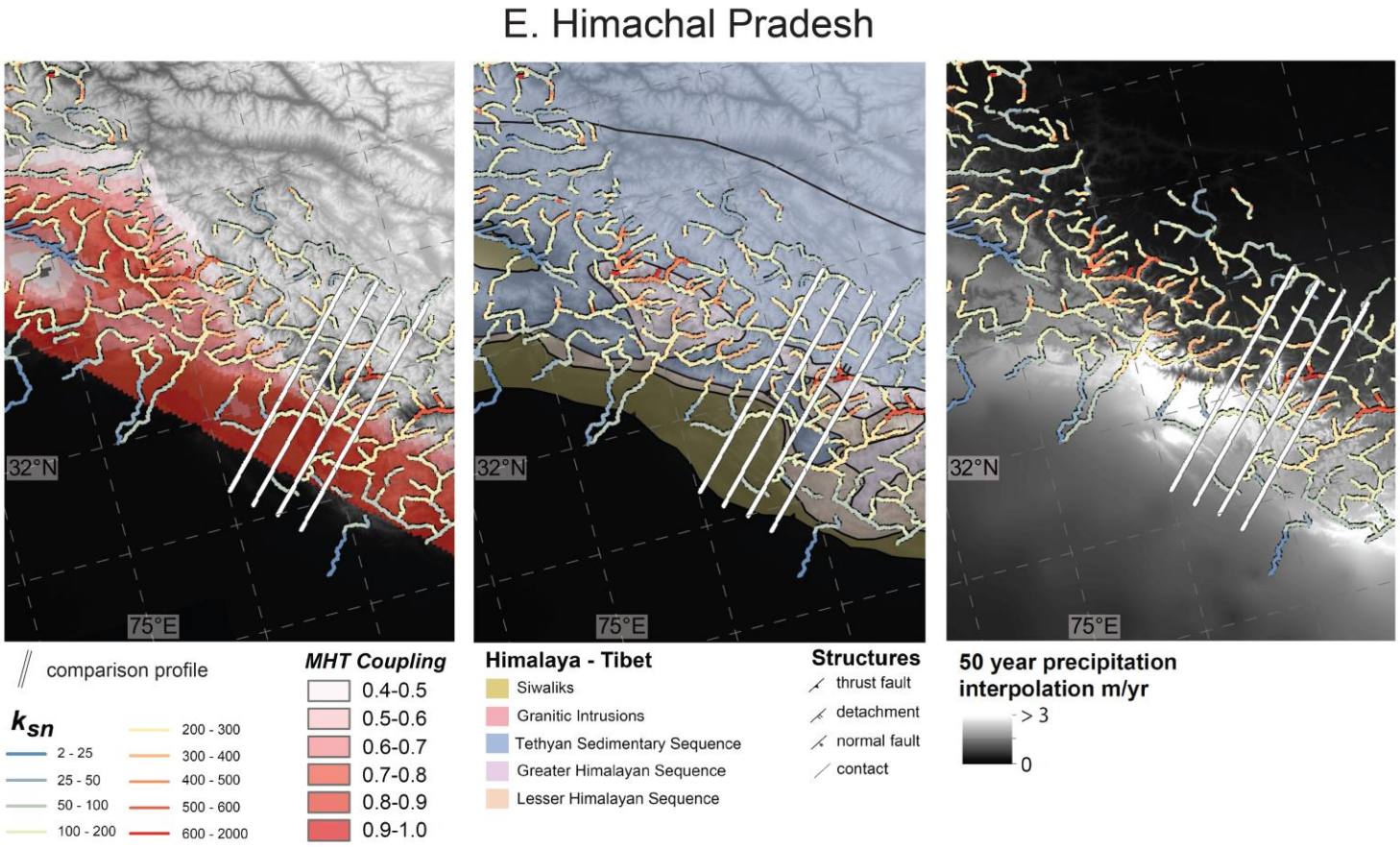

Figure 5c.2. East Himachal Pradesh comparison datasets and profiles 1- 4 (west-to-east). a) MHT coupling and k_{sn}, b) lithology and k_{sn}, c) 50 year precipitation interpolation (Hijmans et al., (2005) and k_{sn}..

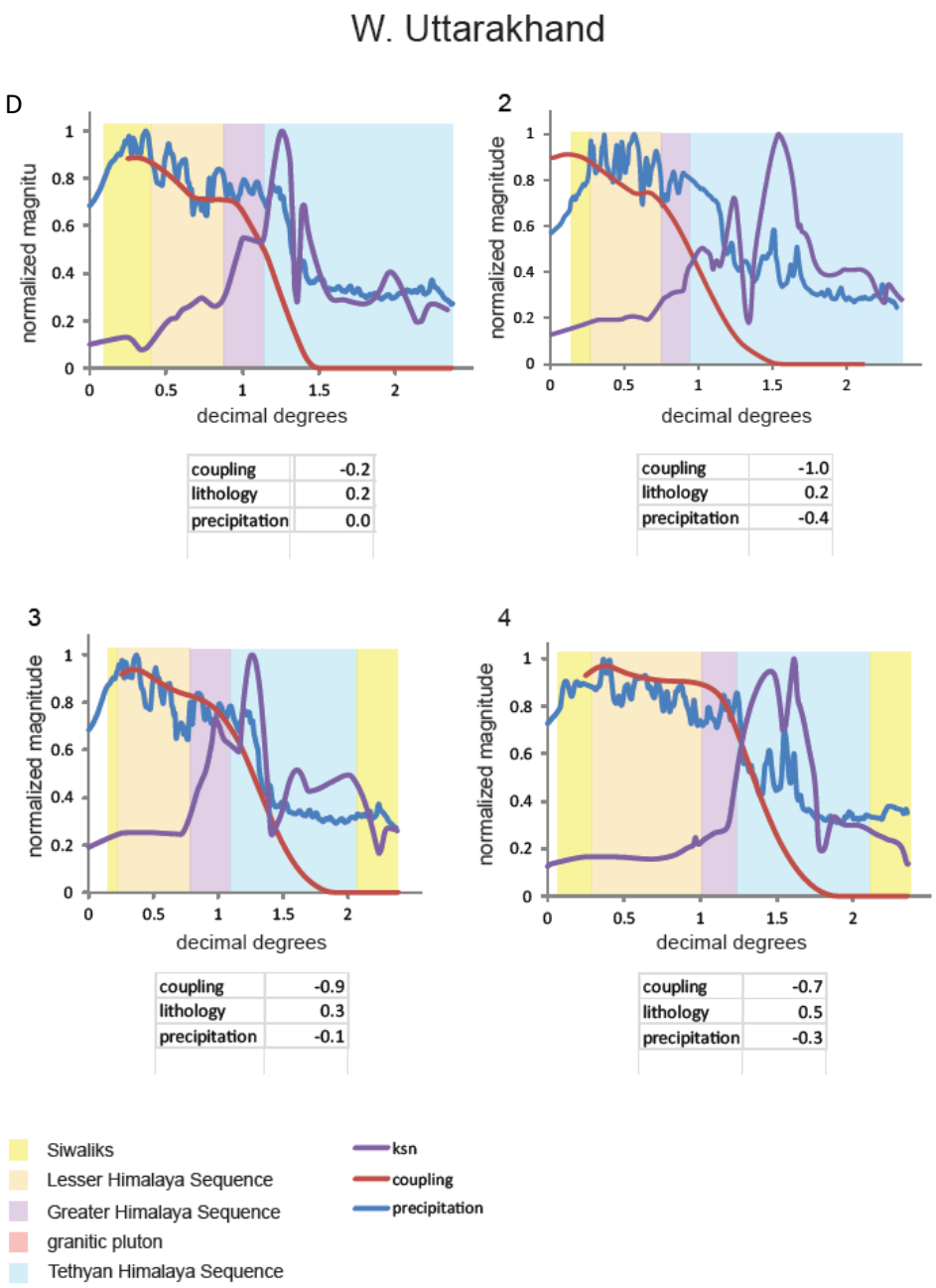

Figure 5d.1. West Uttarakhand comparison profiles 1-4 are plotted west-to-east on map in figure 5a and 5d.2. Correlation coefficients listed below each graph.

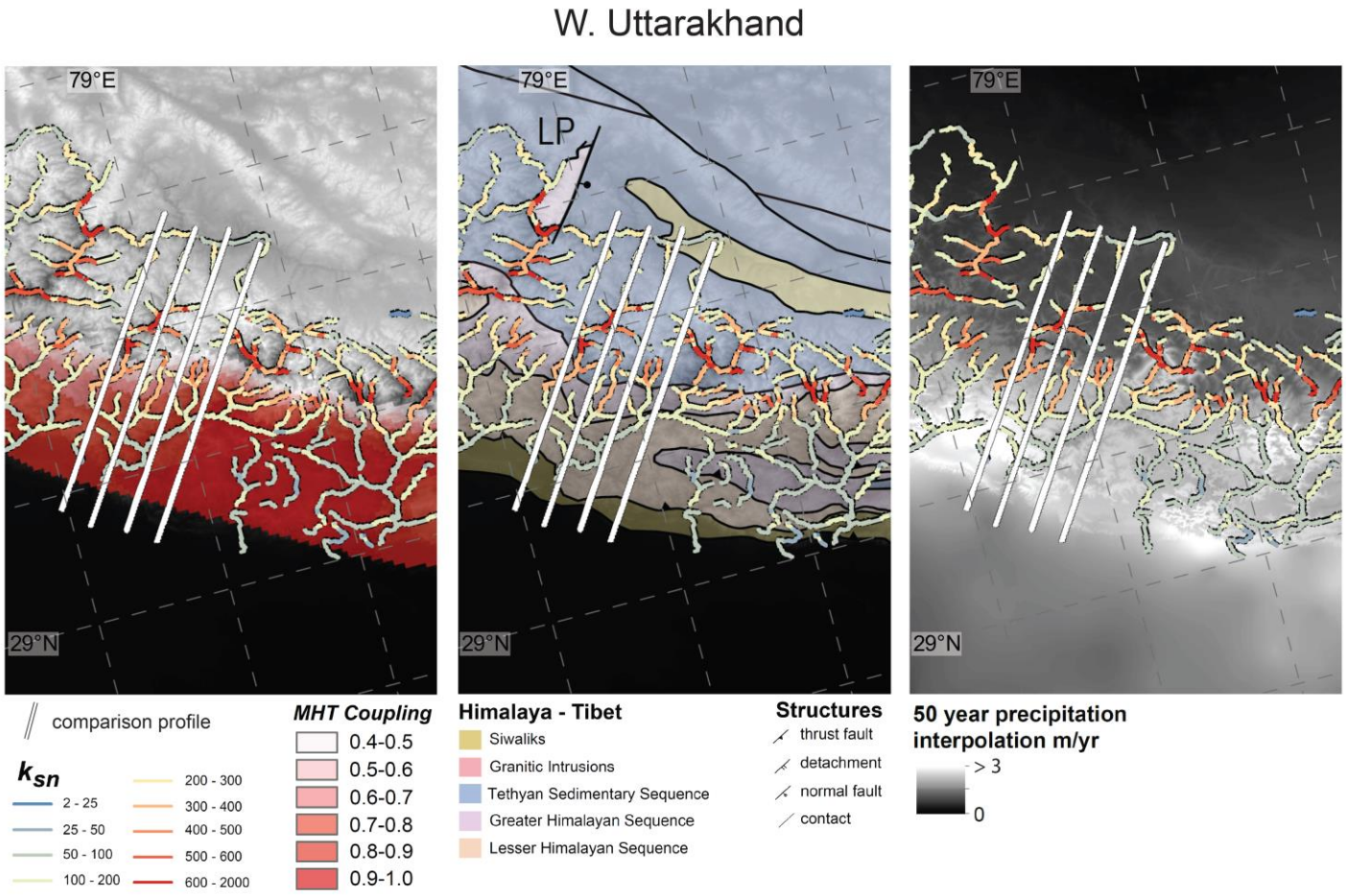

Figure 5d.2. West Uttarakhand comparison datasets and profiles 1- 4 (west-to-east). a) MHT coupling and k_{sn}, b) lithology and k_{sn}, c) 50 year precipitation interpolation (Hijmans et al., (2005) and k_{sn}..

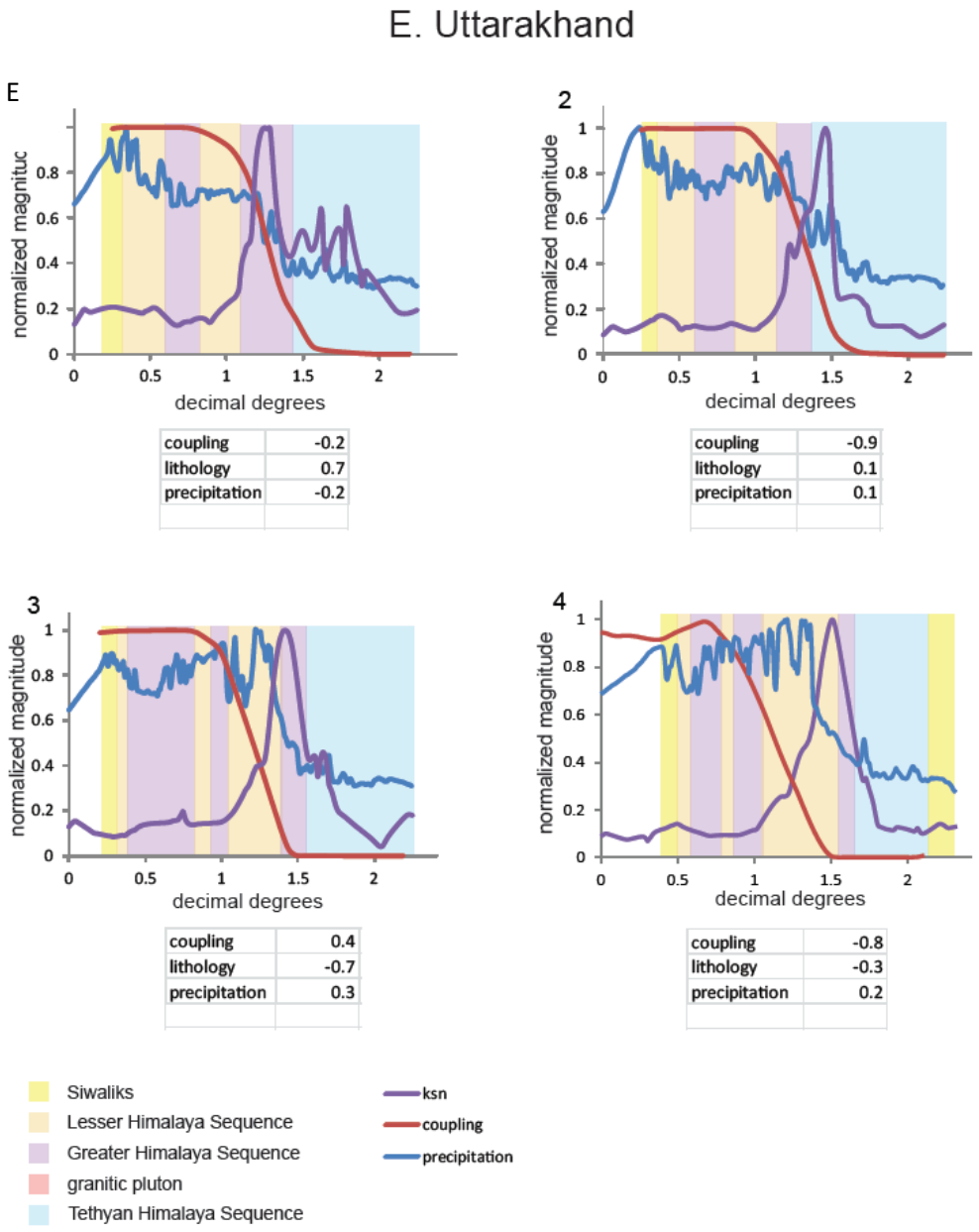

Figure 5e.1. East Uttarakhand comparison profiles 1-4 are plotted west-to-east on map in figure 5a and 5e.2. Correlation coefficients listed below each graph.

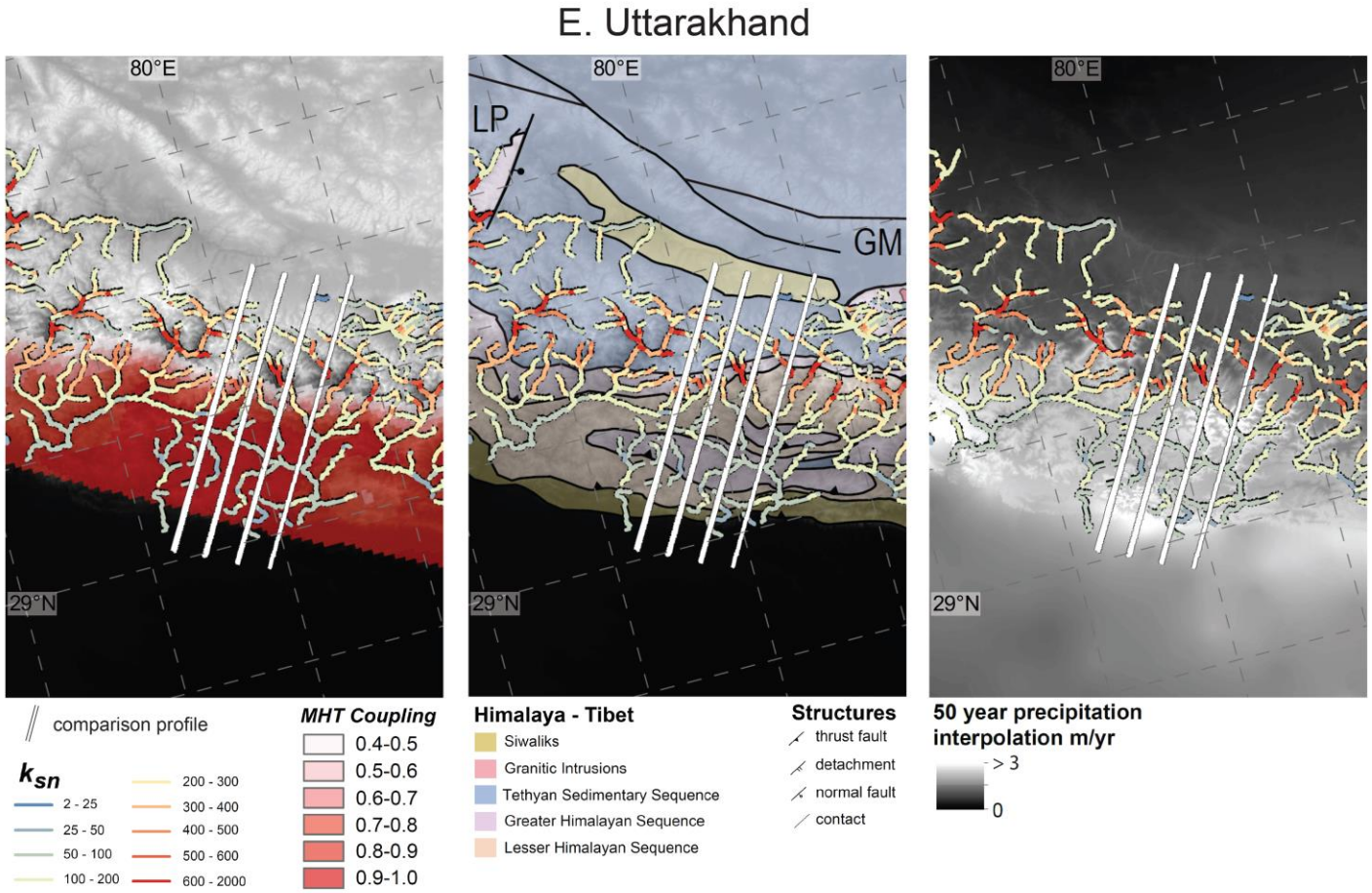

Figure 5e.2. East Uttarakhand comparison datasets and profiles 1- 4 (west-to-east). a) MHT coupling and k_{sn}, b) lithology and k_{sn}, c) 50 year precipitation interpolation (Hijmans et al., (2005) and k_{sn}..

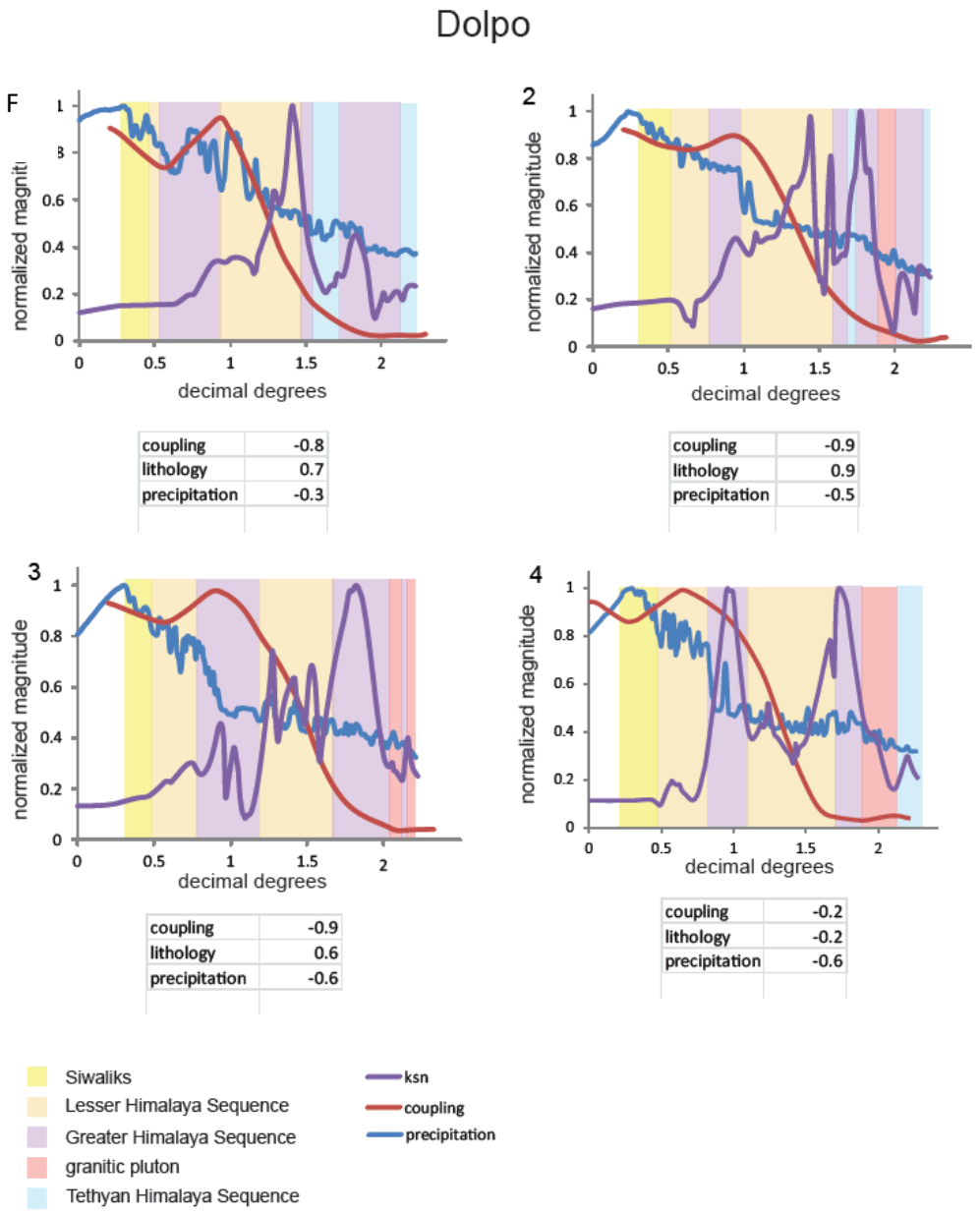

Figure 5f.1. Dolpo comparison profiles 1-4 are plotted west-to-east on map in figure 5a and 5f.2. Correlation coefficients listed below each graph.

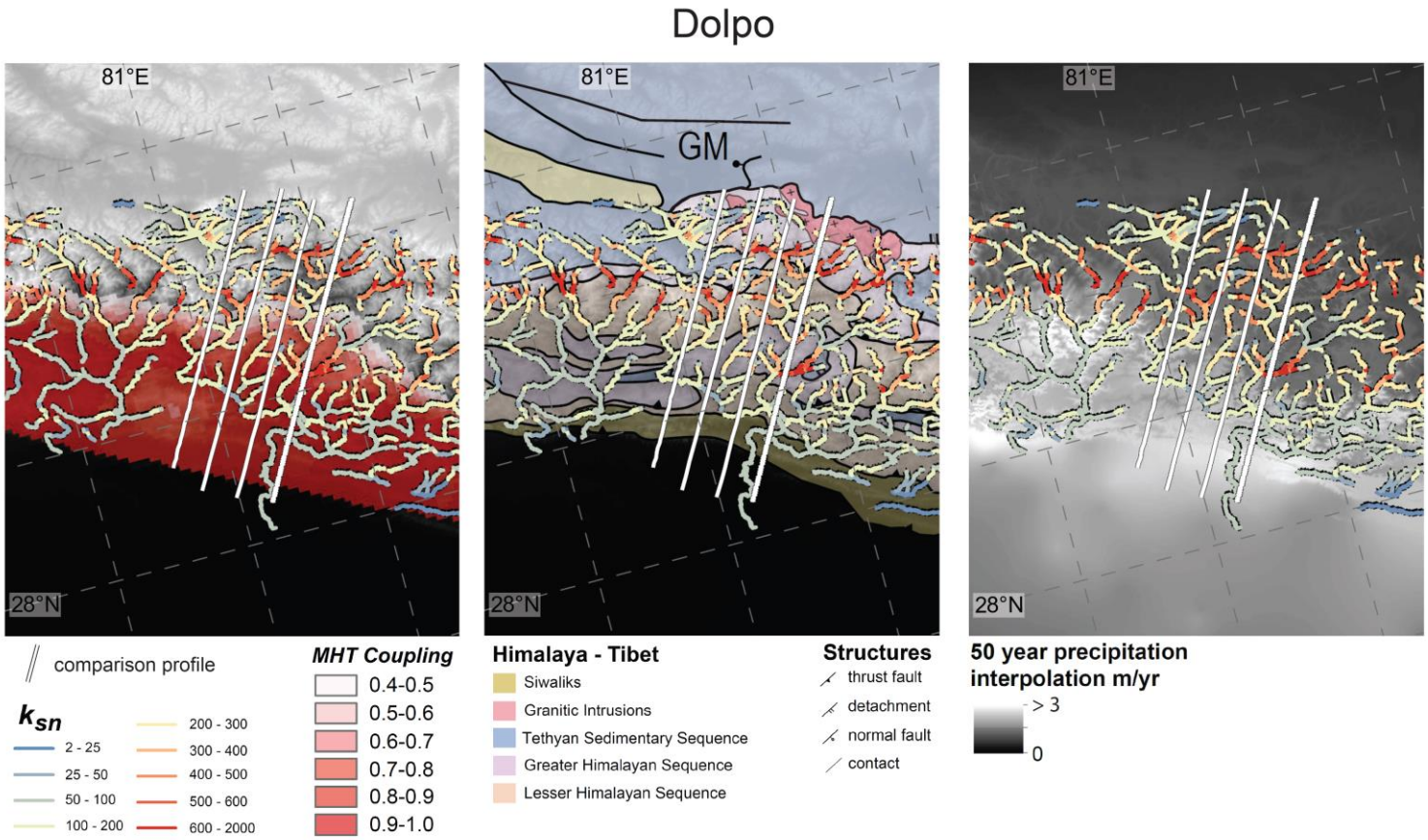

Figure 5f.2. Dolpo comparison datasets and profiles 1- 4 (west-to-east). a) MHT coupling and k_{sn}, b) lithology and k_{sn}, c) 50 year precipitation interpolation (Hijmans et al., (2005) and k_{sn}..

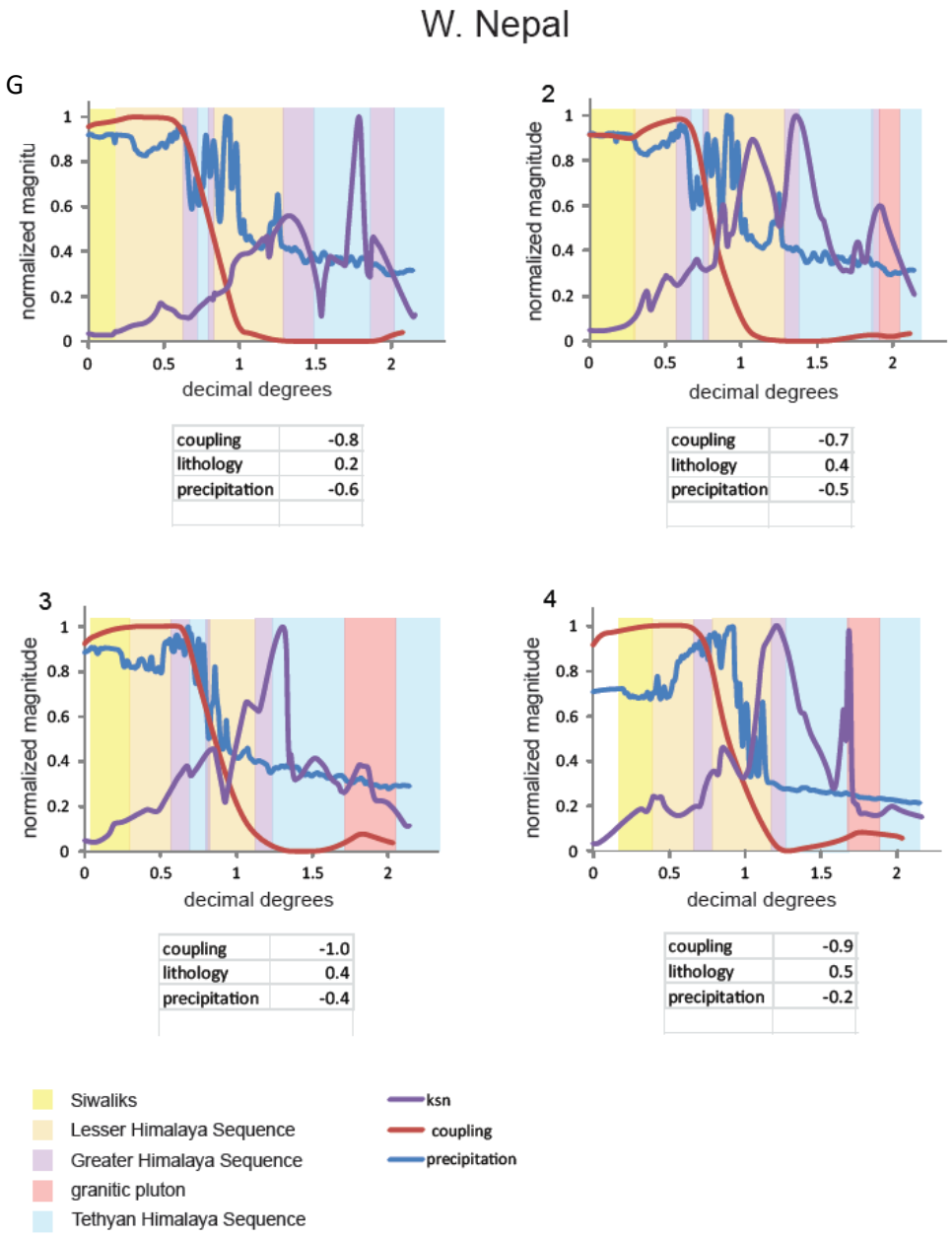

Figure 5g.1. West Nepal comparison profiles 1-4 are plotted west-to-east on map in figure 5a and 5g.2. Correlation coefficients listed below each graph.

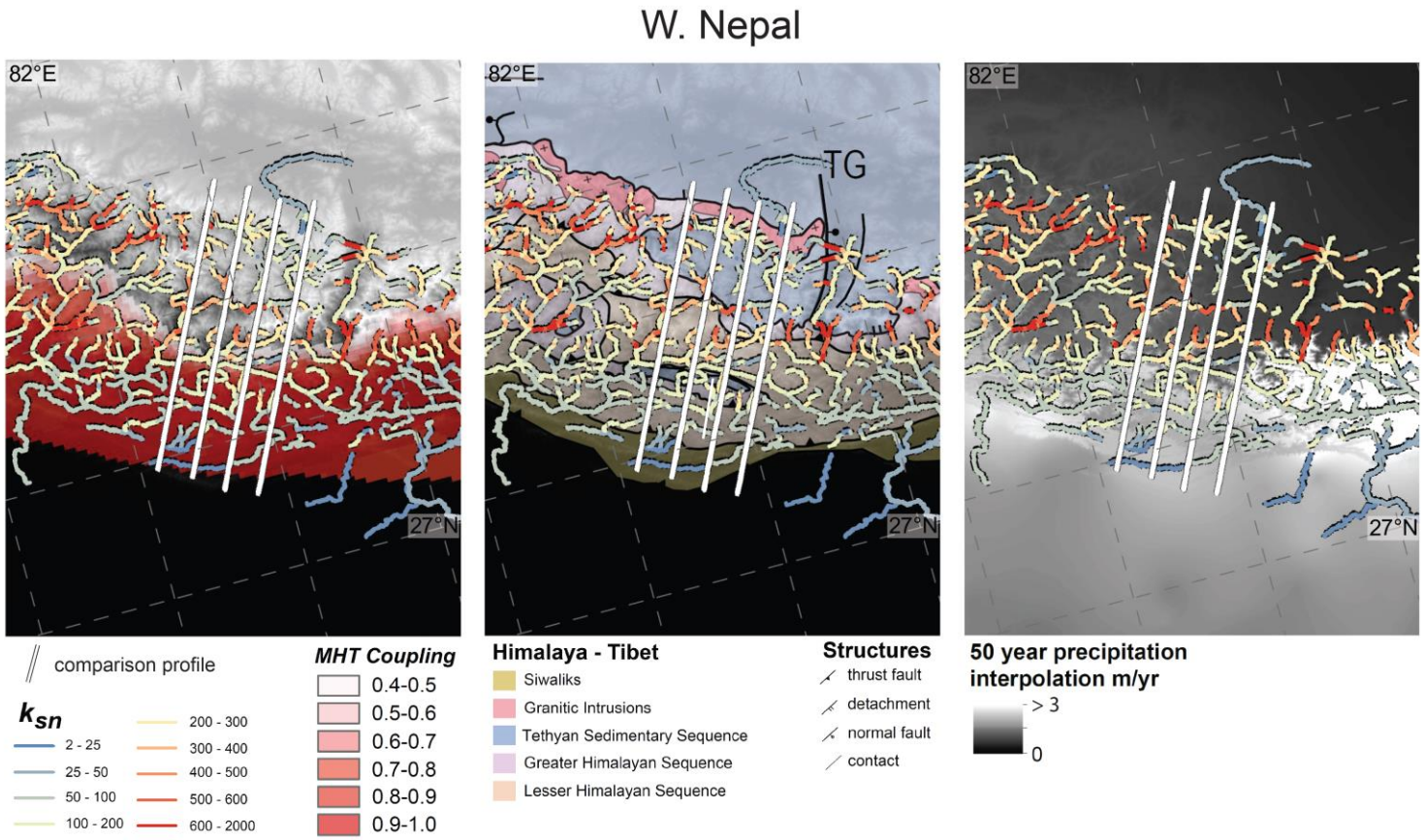

Figure 5g.2. West Nepal comparison datasets and profiles 1- 4 (west-to-east). a) MHT coupling and k_{sn}, b) lithology and k_{sn}, c) 50 year precipitation interpolation (Hijmans et al., (2005) and k_{sn}..

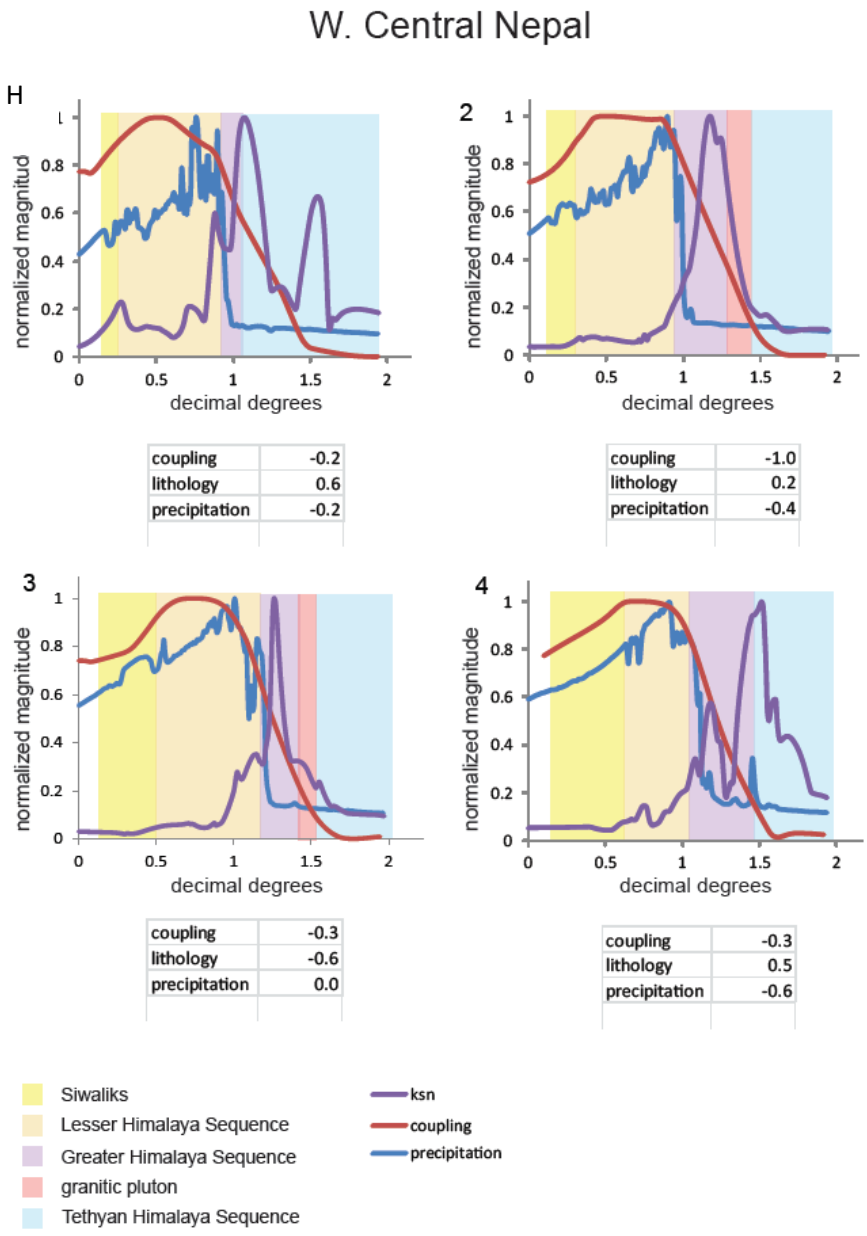

Figure 5h.1. West central Nepal comparison profiles 1-4 are plotted west-to-east on map in figure 5a and 5h.2. Correlation coefficients listed below each graph.

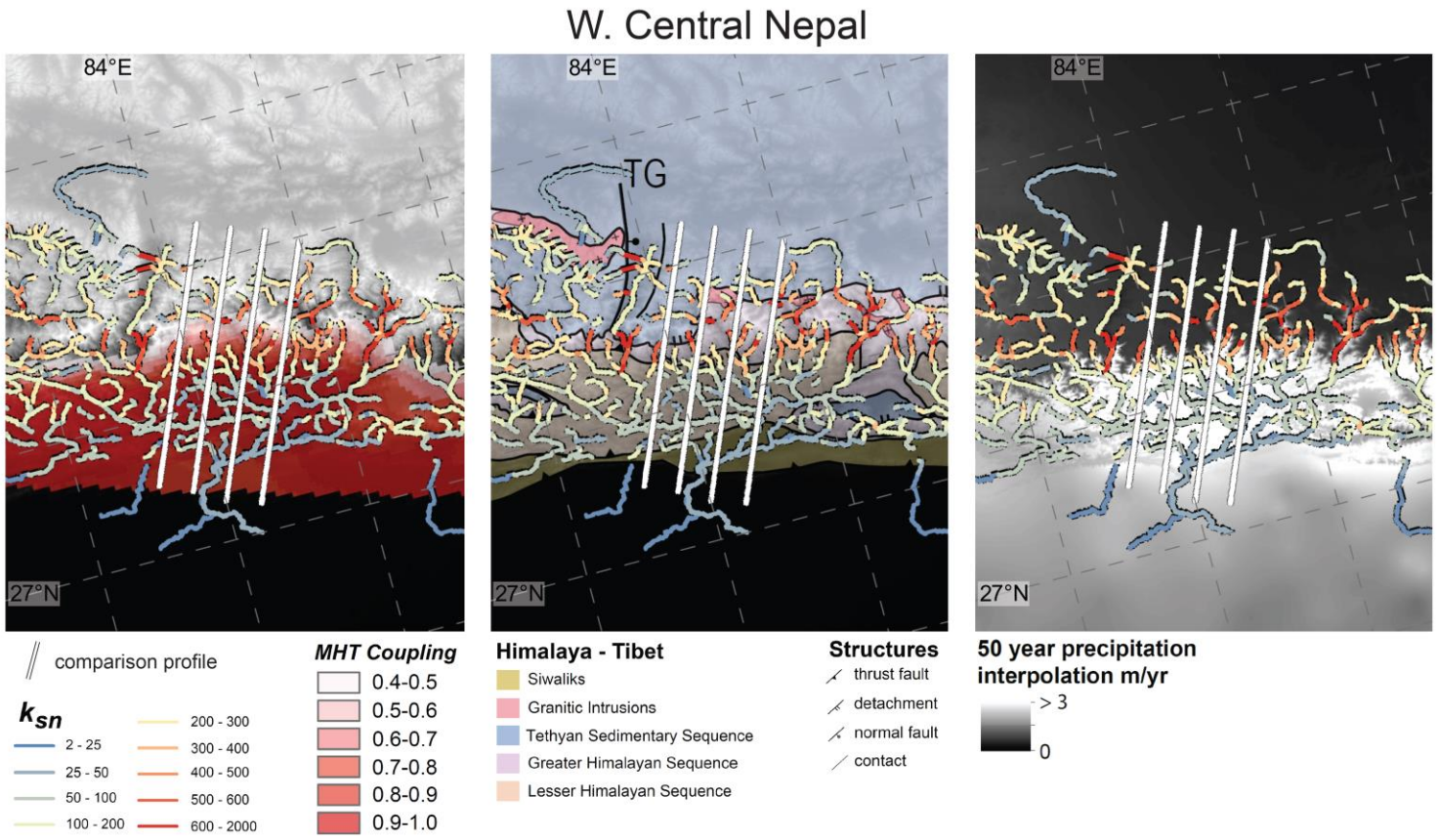

Figure 5h.2. West central Nepal comparison datasets and profiles 1- 4 (west-to-east). a) MHT coupling and k_{sn}, b) lithology and k_{sn}, c) 50 year precipitation interpolation (Hijmans et al., (2005) and k_{sn}.

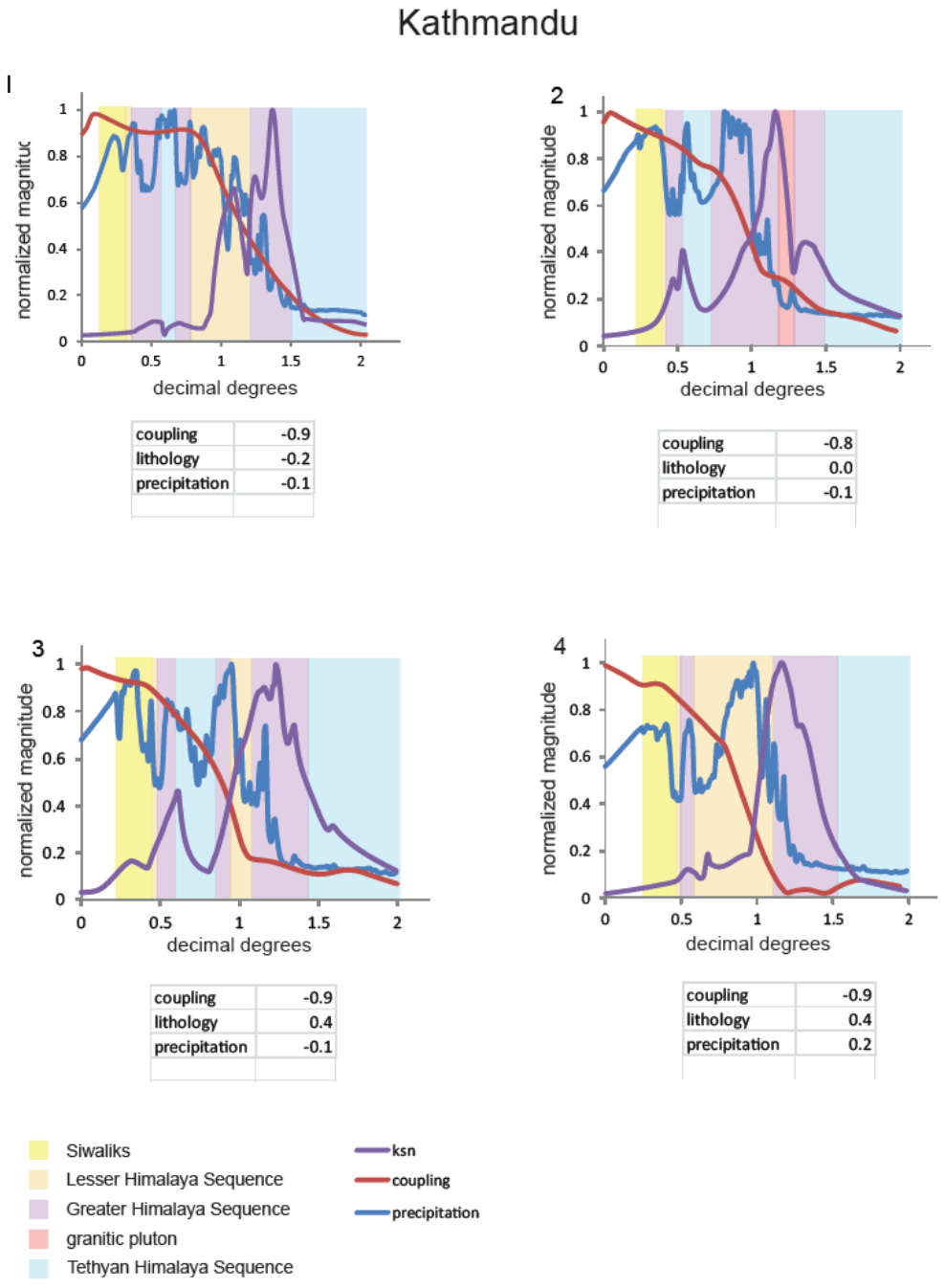

Figure 5i.1. Kathmandu comparison profiles 1-4 are plotted west-to-east on map in figure 5a and 5i.2. Correlation coefficients listed below each graph.

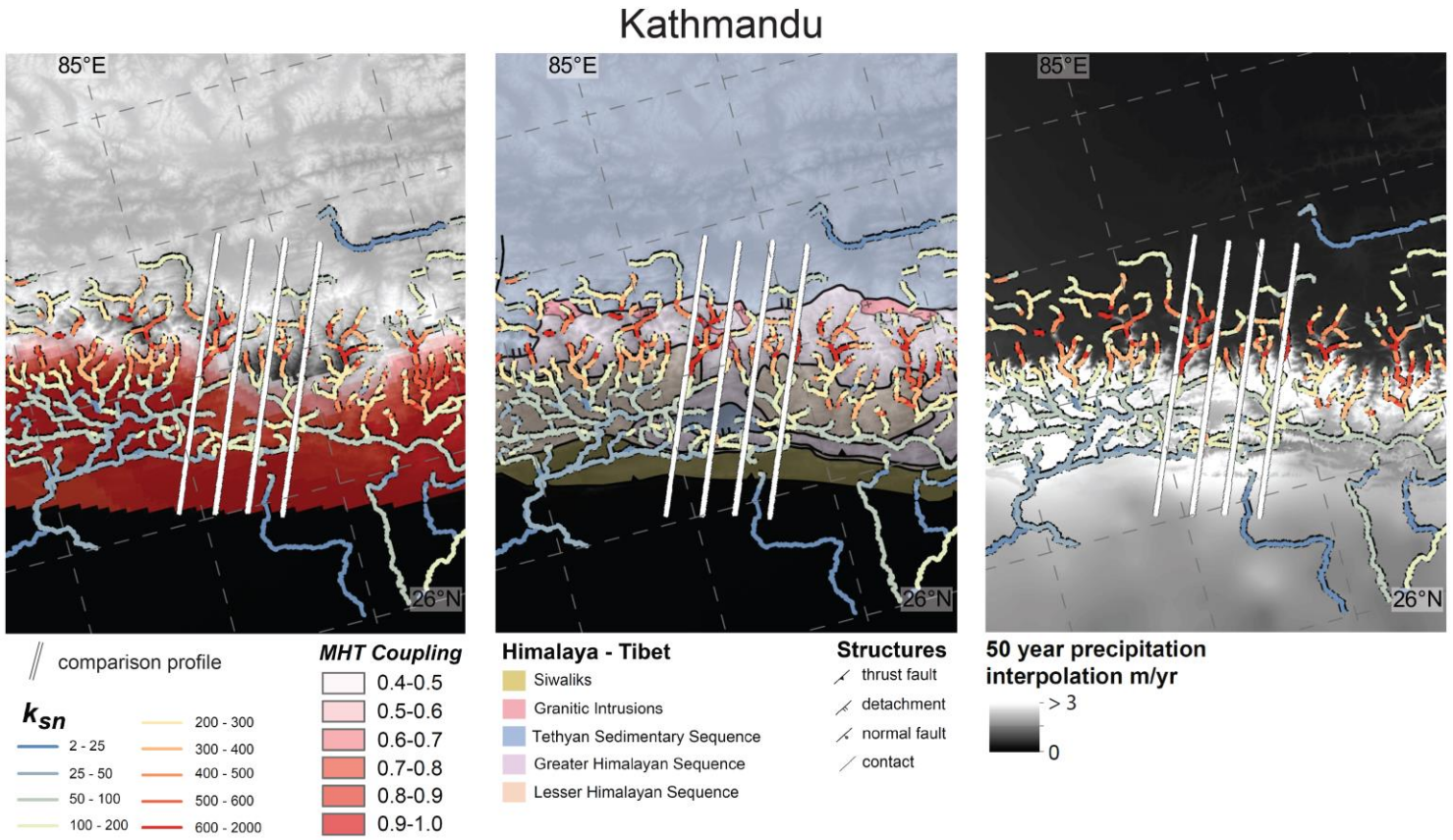

Figure 5i.2. Kathmandu comparison datasets and profiles 1- 4 (west-to-east). a) MHT coupling and k_{sn}, b) lithology and k_{sn}, c) 50 year precipitation interpolation(Hijmans et al., (2005) and k_{sn}..

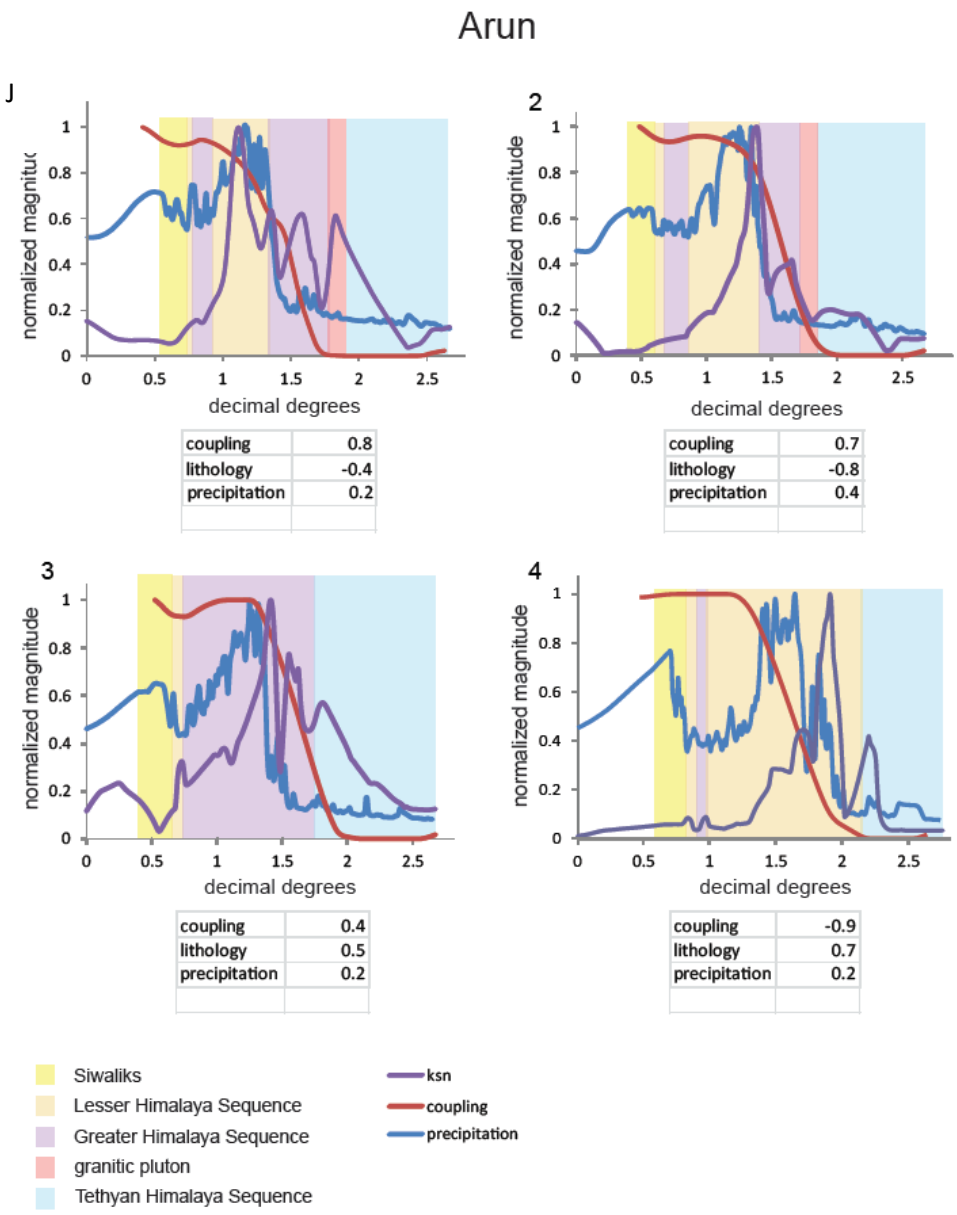

Figure 5j.1. Arun comparison profiles 1-4 are plotted west-to-east on map in figure 5a and 5j.2. Correlation coefficients listed below each graph.

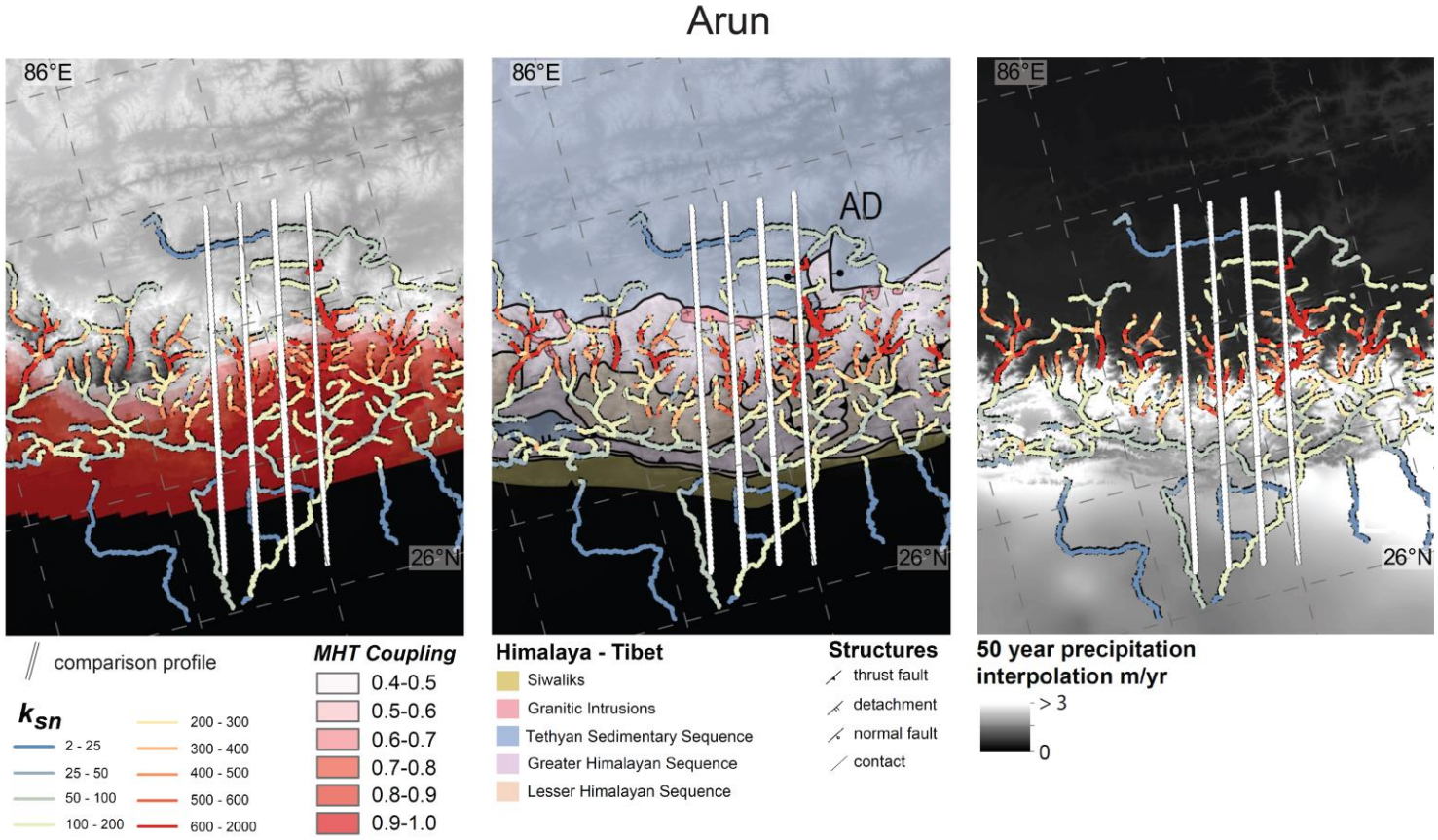

Figure 5j.2. Arun comparison datasets and profiles 1- 4 (west-to-east). a) MHT coupling and k_{sn}, b) lithology and k_{sn}, c) 50 year precipitation interpolation (Hijmans et al., (2005) and k_{sn}..

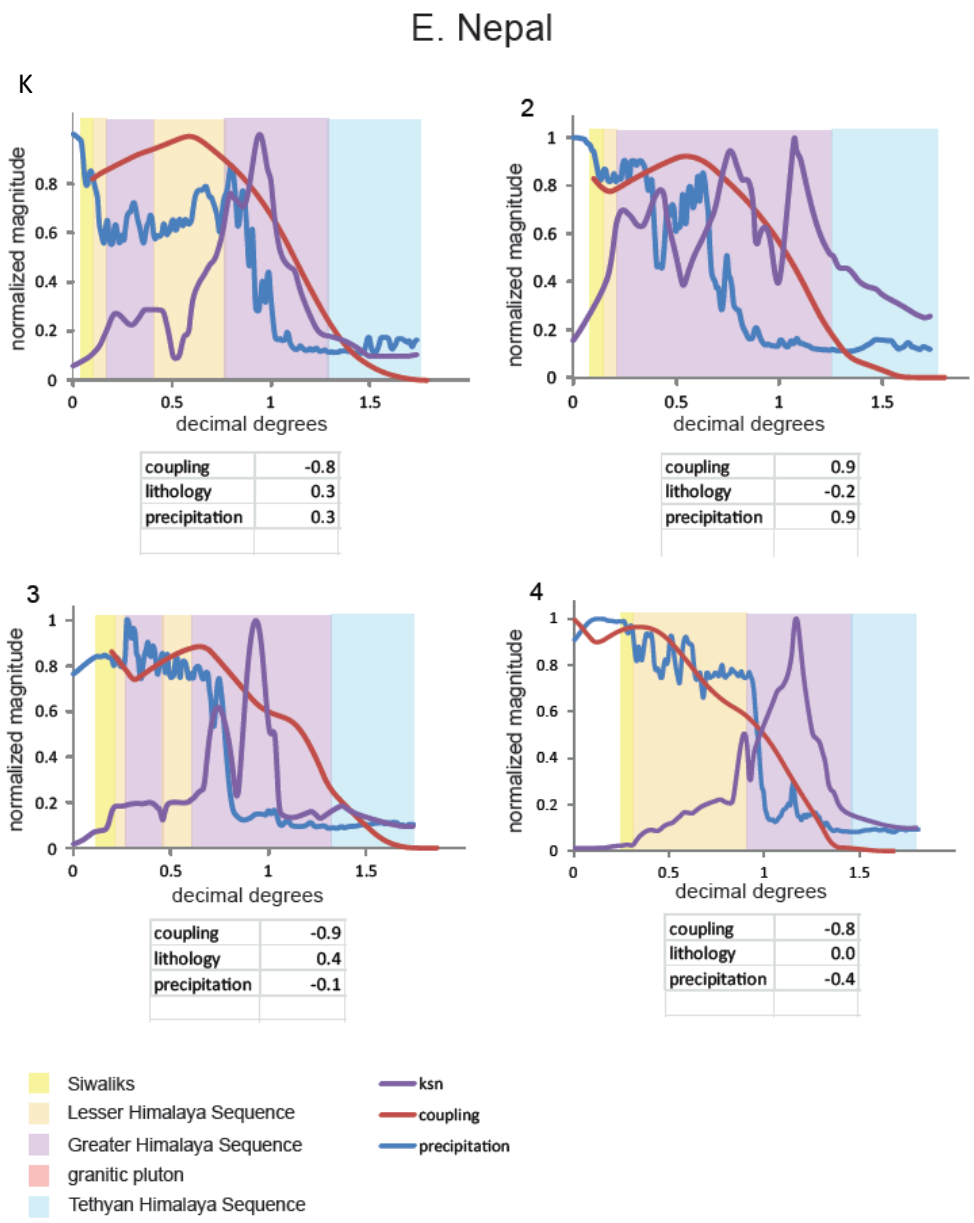

Figure 5k.1. East Nepal comparison profiles 1-4 are plotted west-to-east on map in figure 5a and 5k.2. Correlation coefficients listed below each graph.

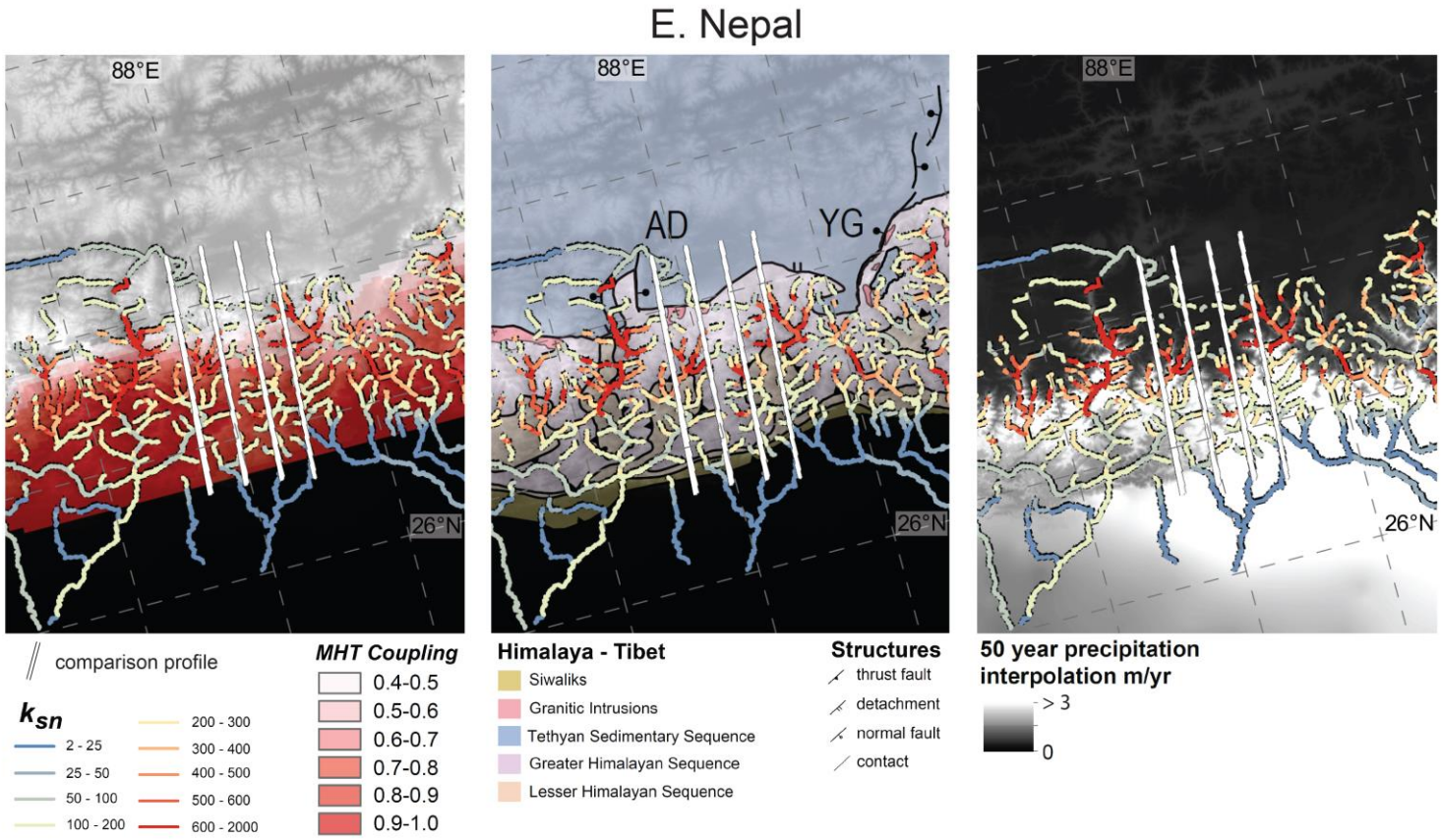

Figure 5k.2. East Nepal comparison datasets and profiles 1- 4 (west-to-east). a) MHT coupling and k_{sn}, b) lithology and k_{sn}, c) 50 year precipitation interpolation (Hijmans et al., (2005) and k_{sn}..

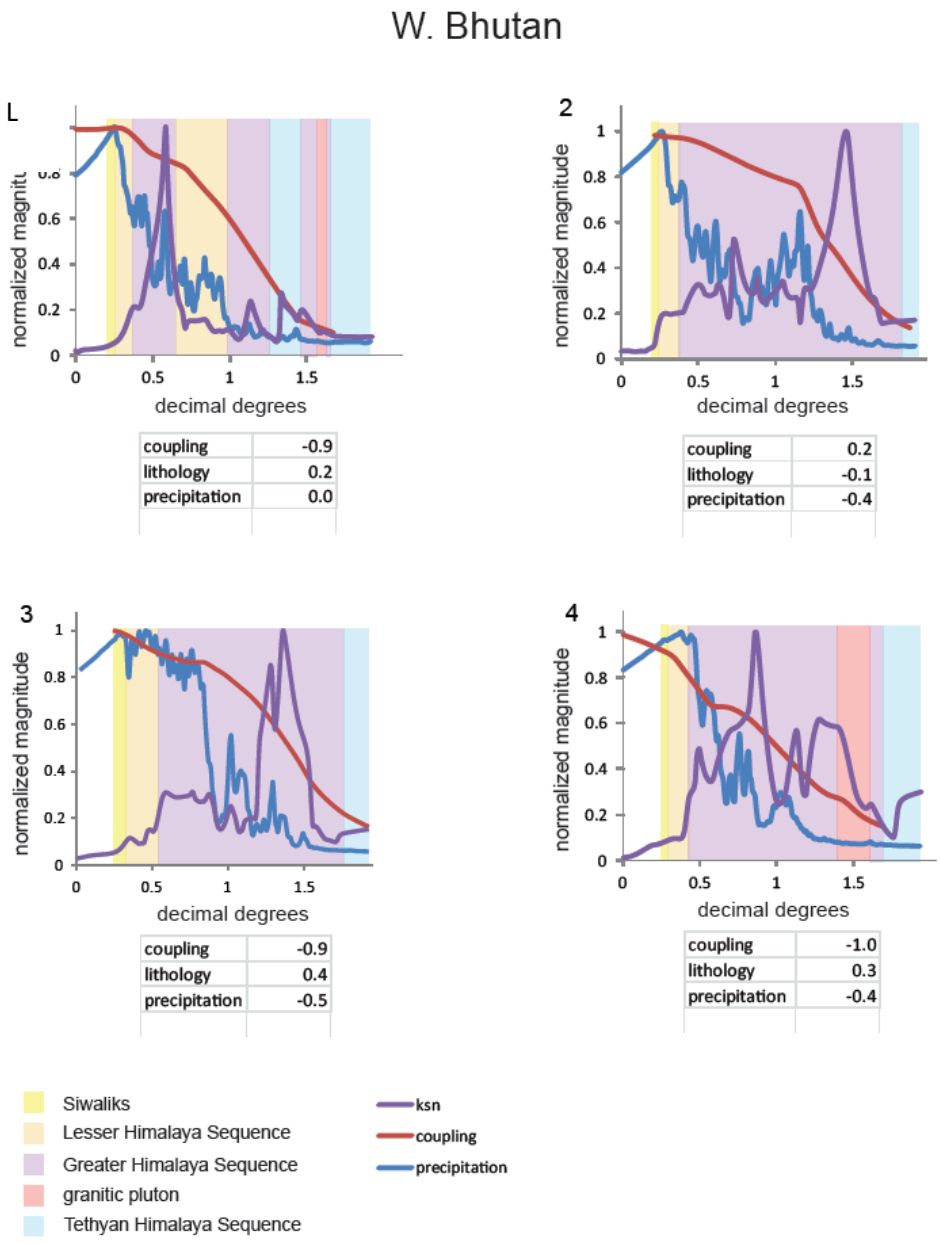

Figure 5l.1. West Bhutan comparison profiles 1-4 are plotted west-to-east on map in figure 5a and 5l.2. Correlation coefficients listed below each graph.

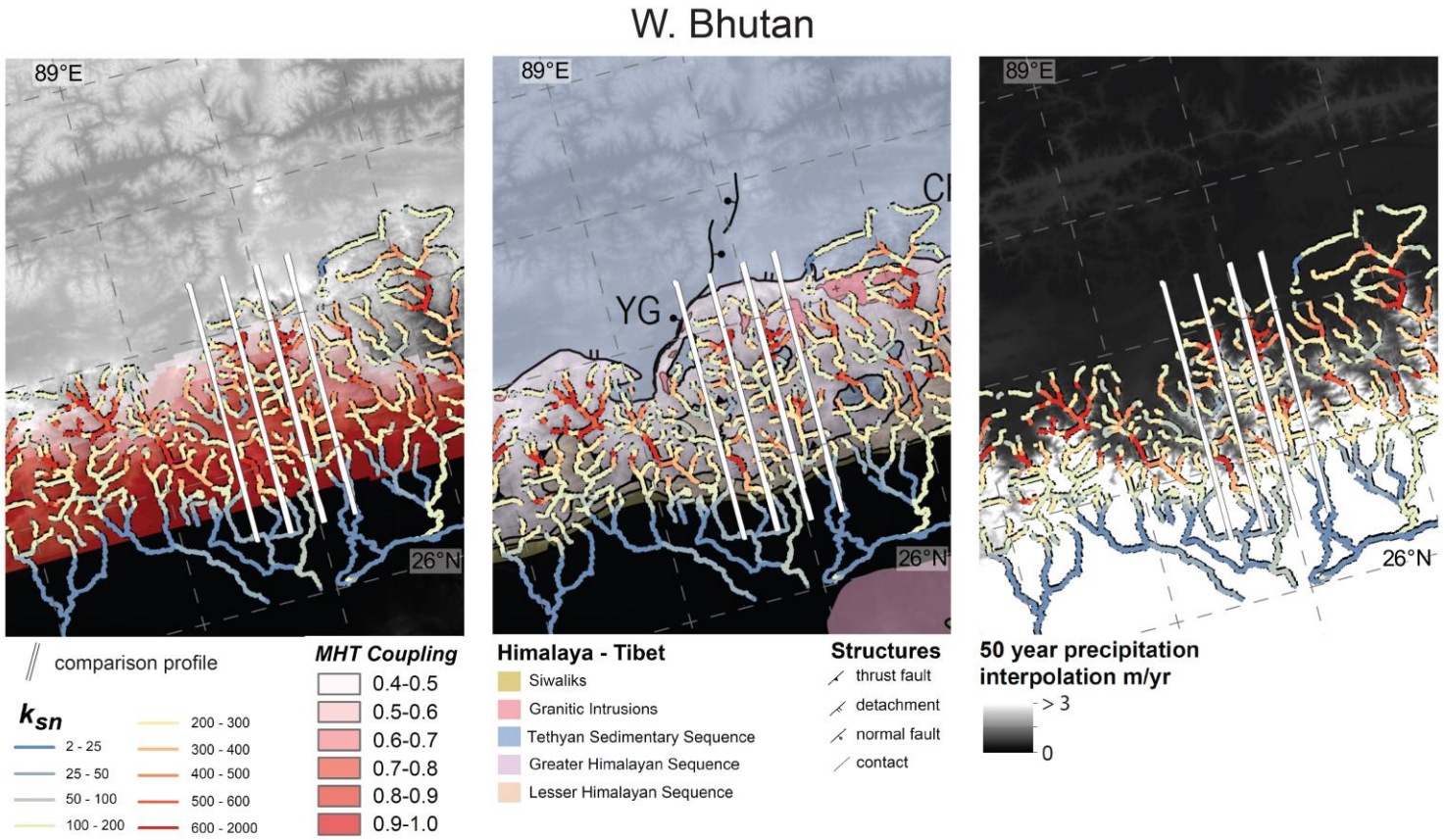

Figure 5l.2. West Bhutan comparison datasets and profiles 1- 4 (west-to-east). a) MHT coupling and k_{sn}, b) lithology and k_{sn}, c) 50 year precipitation interpolation (Hijmans et al., (2005) and k_{sn}..

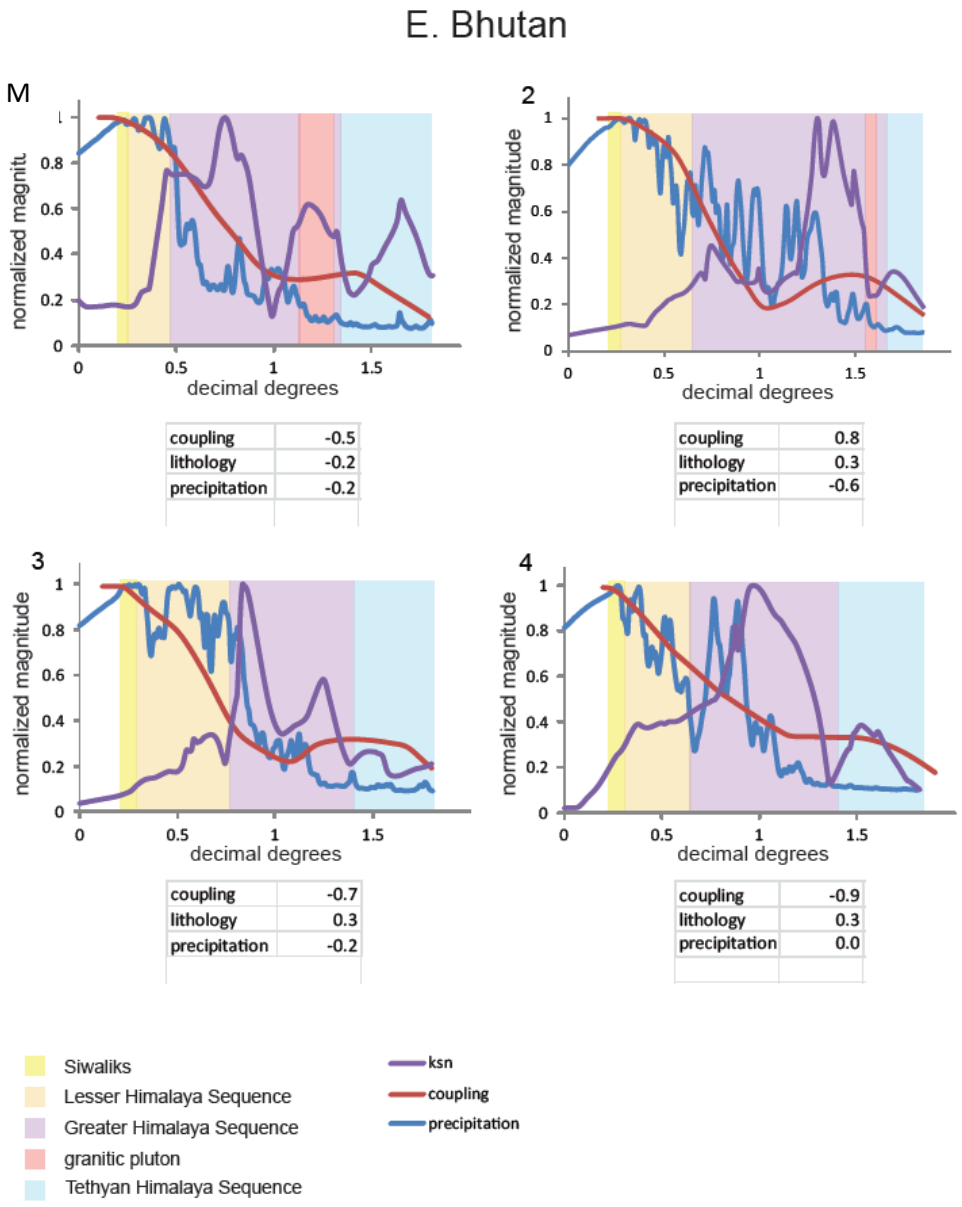

Figure 5m.1. East Bhutan comparison profiles 1-4 are plotted west-to-east on map in figure 5a and 5m.2. Correlation coefficients listed below each graph.

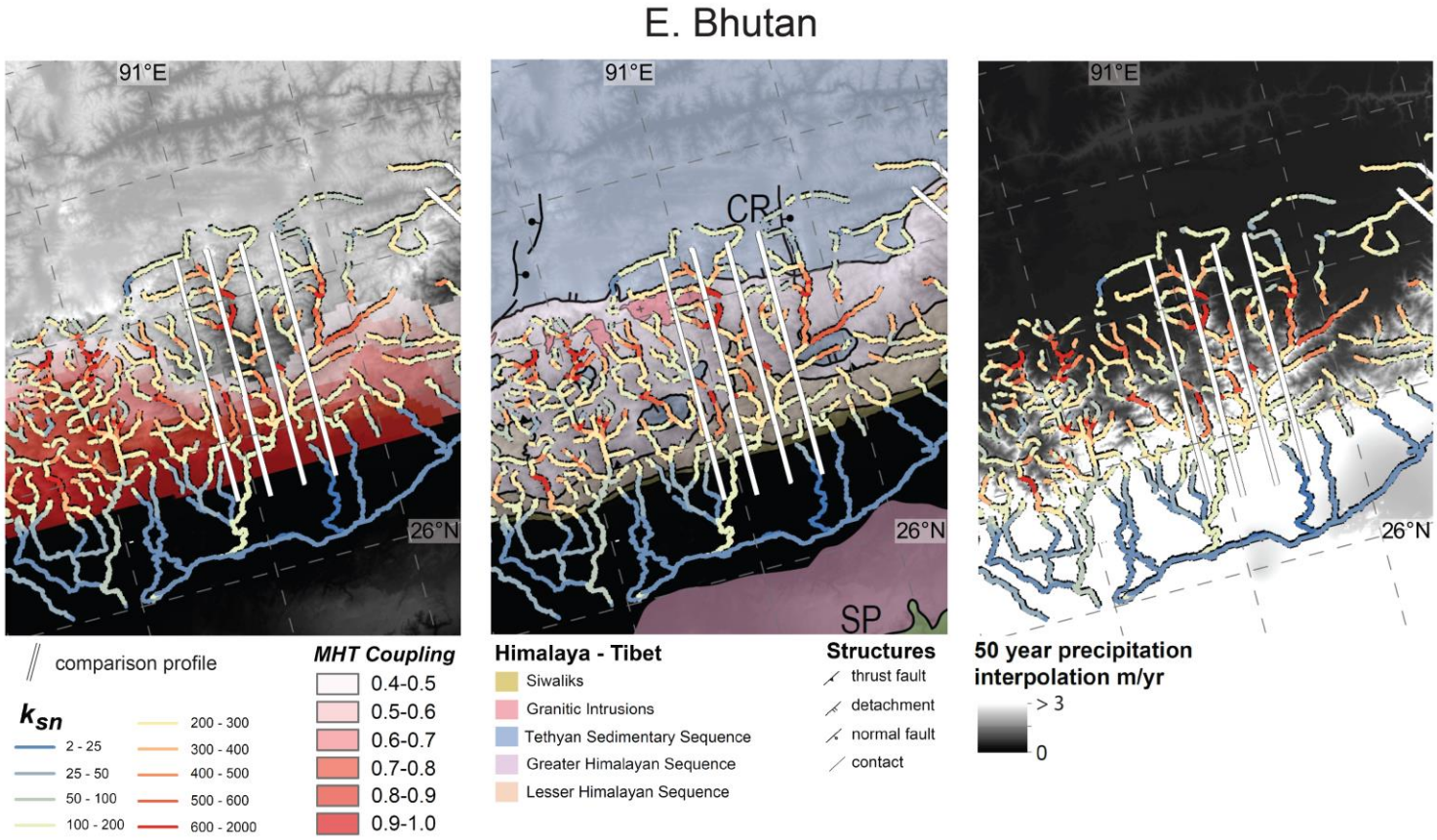

Figure 5m.2. East Bhutan comparison datasets and profiles 1- 4 (west-to-east). a) MHT coupling and k_{sn}, b) lithology and k_{sn}, c) 50 year precipitation interpolation (Hijmans et al., (2005) and k_{sn}..

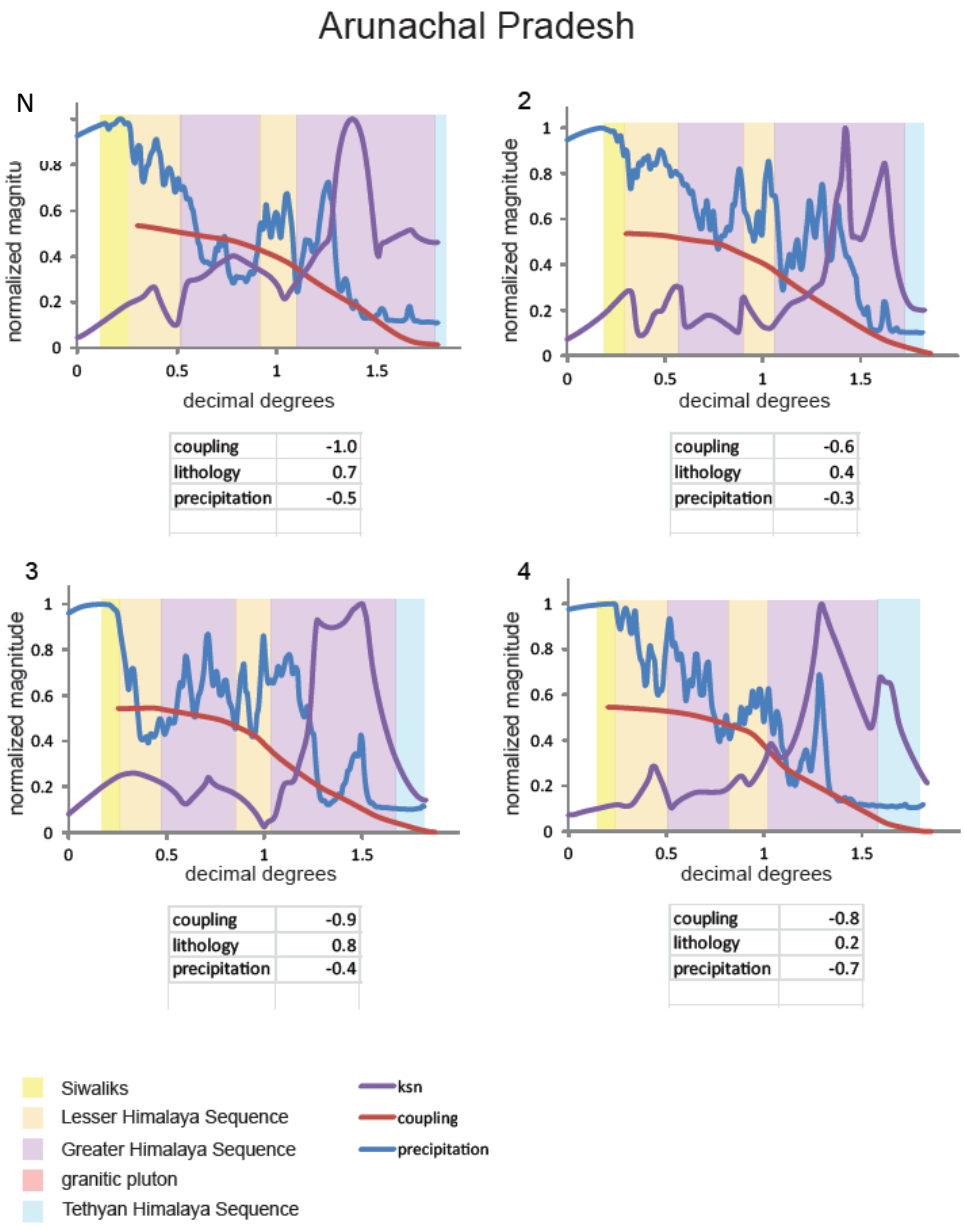

Figure 5n.1. Arunachal Pradesh comparison profiles 1-4 are plotted west-to-east on map in figure 5a and 5n.2. Correlation coefficients listed below each graph.

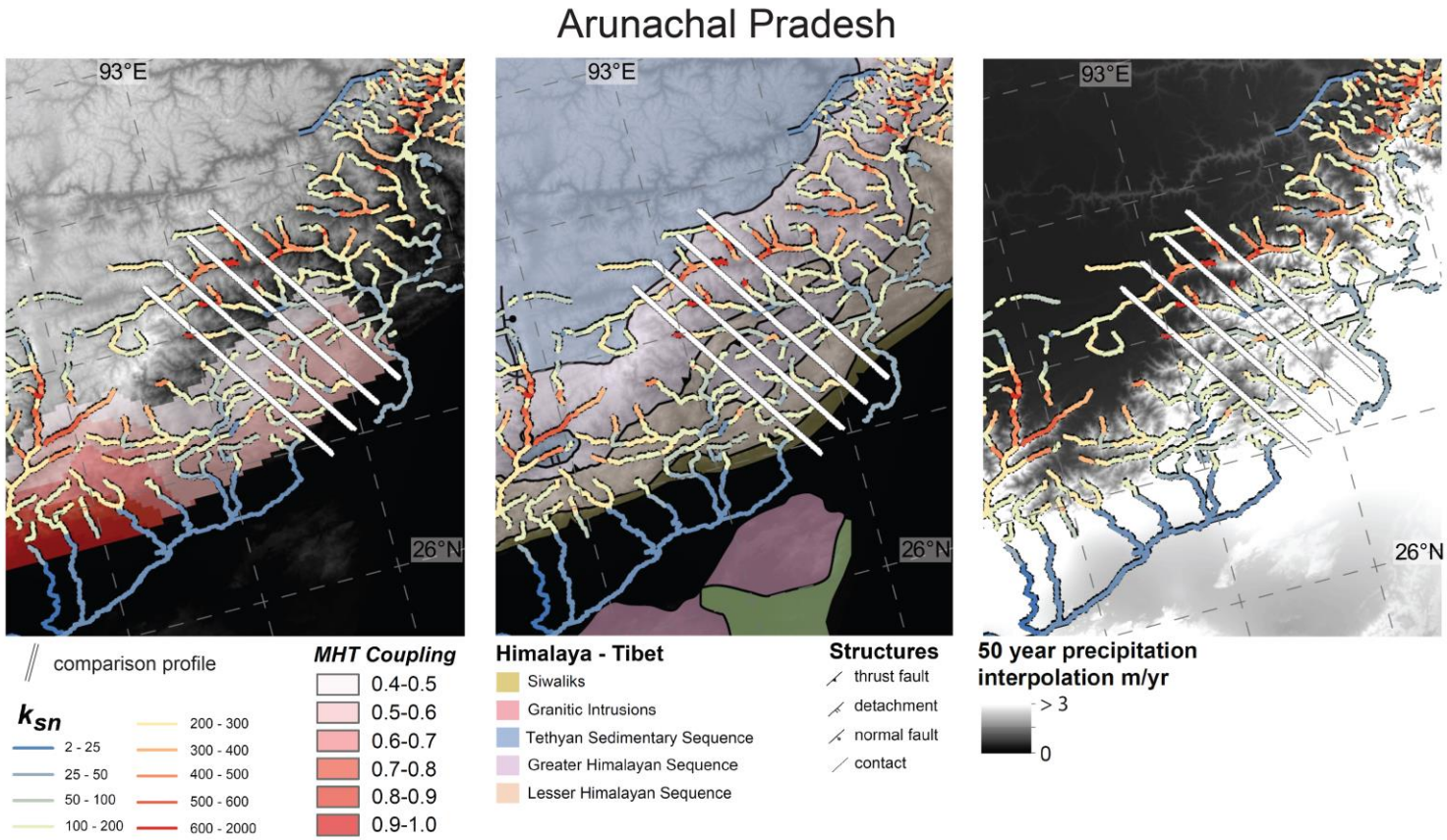

Figure 5n.2. Arunachal Pradesh comparison datasets and profiles 1- 4 (west-to-east). a) MHT coupling and k_{sn}, b) lithology and k_{sn}, c) 50 year precipitation interpolation (Hijmans et al., (2005) and k_{sn}..

2.5 Results

The results of the k_{sn} analysis and the statistical analysis are presented in the following sections. First, I evaluated the relative contributions precipitation, lithology (proxy for substrate erodability), and MHT coupling have on the k_{sn} signal, and then present my Himalayan river channel steepness data.

Table 1 Average correlation coefficients by region

Region	**Precipitation**	**Lithology**	**MHT Coupling**
West Himachal Pradesh	0.1	0.2	-0.5
East Himachal Pradesh	0.2	0.5	-0.9
West Uttarakhand	-0.2	0.3	-0.7
East Uttarakhand	0.2	0.1	-0.4
Dolpo	-0.5	0.5	-0.7
West Nepal	-0.4	0.4	-0.8
West Central Nepal	-0.3	0.2	-0.5
Kathmandu	0.0	0.1	-0.9
Arun	0.3	0.0	0.3
East Nepal	0.2	0.1	-0.4
West Bhutan	-0.3	0.2	-0.6
East Bhutan	0.2	0.2	-0.7
Arunachal Pradesh	-0.5	0.5	-0.8
Average	-0.1	0.3	-0.6

2.5.1 Climate Comparison

A map of average rainfall interpolated for the last 50 years (Hijmans et al., 2005) was used to generate correlation coefficients for k_{sn} and precipitation. The average r (correlation coefficient) for the entire Himalaya is -0.1 with a p-value of < 0.005 demonstrating a poor correlation with river-channel steepness (Figure 2.5b-n). The greatest degree of correlation was seen in Dolpo and Arunachal Pradesh where r = -0.5. The extremely low degree of average correlation reveals that either the spatial pattern of Himalayan precipitation has undergone significant changes over the last hundred thousand years or precipitation gradients play only of minor role in modulating k_{sn}.

2.5.2 Lithology Comparison

This analysis revealed a moderate degree of positive correlation (average r = 0.3 and a p-value of < 0.05) for k_{sn} and lithology (Figure 2.5b-n). Regionally, the correlation was strongest in east Himachal Pradesh, Dolpo, and Arunachal Pradesh (See Table 1) where r = 0.5, demonstrating the effect that the juxtaposition of lithologies with different erodibilities can have on river channel steepness. The moderate degree of positive correlation between k_{sn} and lithology is evidence of the role substrate erodibility plays in modulating the k_{sn} signal,

while it can be locally significant, e.g. capstone plateaus, regionally it plays a secondary role in setting the pattern of river channel steepness.

2.5.3 MHT Coupling Comparison

MHT coupling (Stevens and Avouac, 2015) is well correlated with k_{sn} (-0.6 and p-value < 0.05) (Figure 2.5b-n). The strong negative correlation between the degree of MHT coupling and river-channel steepness suggests that in the Himalaya, rock-uplift rate is the primary driver of river channel steepening, relating it directly to interseismic strain accumulation. Regionally, this correlation is often stronger than the average, and in many cases approaches -1 (See Table 1). The strength of the negative correlation was limited by a single positive outlier (Arun 0.4). While the GPS dataset that the MHT coupling model was based upon was recorded over decadal timescales, it takes far longer (10^4-10^5 years) for the k_{sn} signal to be recorded, indicating that the localization of rapid rock uplift is in steady-state over these timescales. This guided our interpretation of k_{sn} as primarily a function of the degree of MHT coupling, and by inference strain accumulation. Our findings suggest that of the three fundamental forcing mechanisms thought to influence river-channel steepness (substrate erodibility, precipitation gradients, and rock-uplift rate), in the Himalaya, rock-uplift rate is the primary driver, modulated by lithology, and to a minor extent by the pattern of

modern precipitation. This is in agreement with recent studies of the Bhutan Himalaya (Adams et al., 2016; Adams, 2014).

2.5.4 Normalized River Channel steepness

Over most its 2500 km length, regions of rapid rock uplift in the Himalaya can be characterized by clusters of high k_{sn} rivers overlying weakly coupled portions of the MHT located 60-120 km north of the range front (Figure 2.2c). Only west Nepal and Bhutan host high k_{sn} clusters that overlie strongly coupled portions of the MHT, 30-50 km from the range front (Figure 2.2c). The spatial dimensions of the high k_{sn} clusters vary in width, length, and distance from the range front and are summarized in Table 2.

Table 2 Spatial dimensions and distance from the range front of high k_{sn} clusters

Region	Arc normal width (km)	Arc parallel length (km)	Arc normal distance from range front (km)
Himachal Pradesh	70-80	340	70-100
Uttarakhand	78-80	290	90-115
West Nepal (2 clusters)	46-60 (north) 30 (south)	200 (north) 80 (south)	120 (north) 50 (south)
Central Nepal	70-80	380	60-70
East Nepal	65	125	70
Bhutan (2 clusters)	40-50 (north) 30-50 (south)	230 (north) 240 (south)	80-110 (north) 30-40 (south)
Arunachal Pradesh	40-50	270	90-110

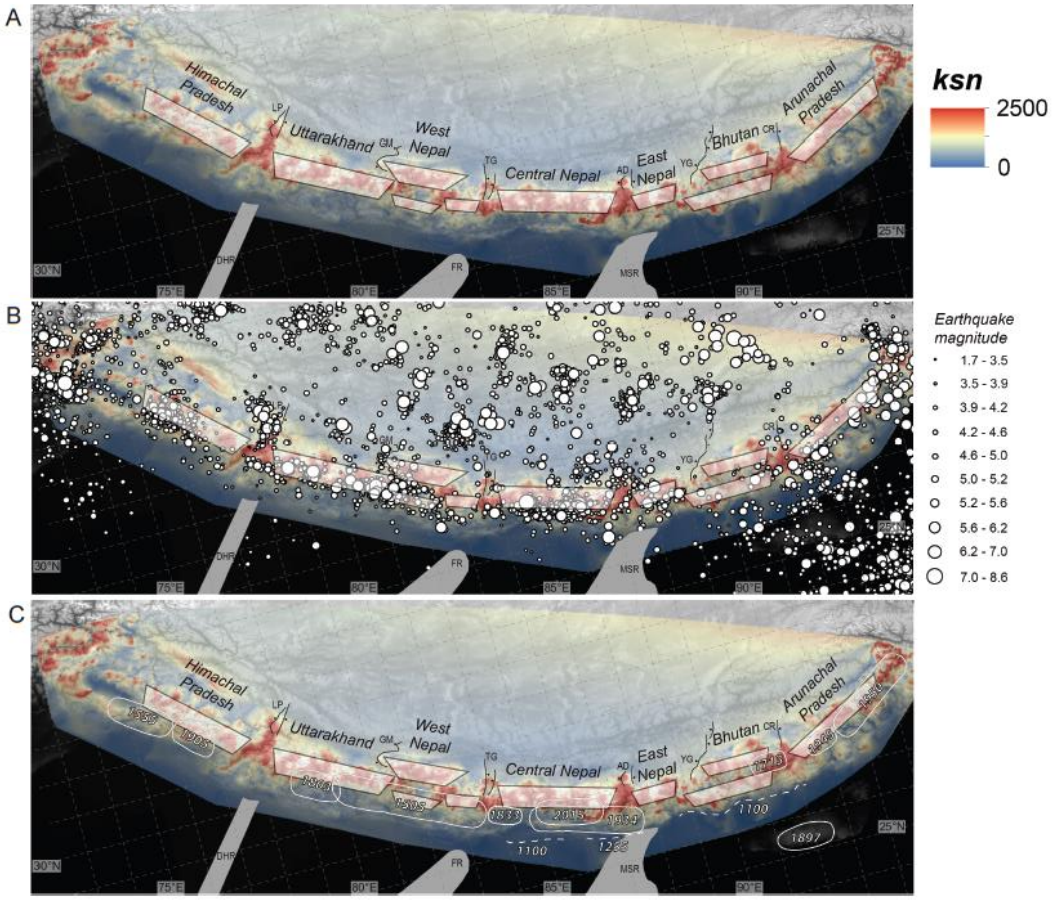

Figure 2.6. a) Interpolated k_{sn} with continuous high k_{sn} segments (labelled) highlighted as semi-transparent polygons and Hima-Tibetan rifts. b) Interpolated k_{sn} map with Hima-Tibetan seismicity (1973-2015 National Earthquake Information Center) overlaid. c) Interpolated k_{sn} map with historical ruptures (Ambraseys and Jackson, 2003; Berthet et al., 2014) overlaid.

High k_{sn} clusters overlying weakly coupled portions of the MHT are located at variable distances (60-120 km) from the range front, but nearly all are between 70 km and 100 km. Neighboring segments host clusters that are

typically offset by 10-20 km, but by as much as 60 km in the case of the west Nepal-central Nepal segments. This indicates that whatever mechanism (passive uplift above MHT ramps, out-of-sequence thrusting, duplexing, tectonic wedging) is responsible for rapid rock uplift within the clusters it is not purely a function of distance from the range front as would be expected if the geometry of the MHT was invariable. The boundaries between segments are collocated with Hima-Tibetan rifts suggesting that they may share a common causal mechanism (Figure 2.6a). Three of the segment boundaries, the Himachal Pradesh - Uttarakhand, west Nepal - central Nepal, and east Nepal - Bhutan are coincident with Indian basement ridges (Figure 2.6a). The longest continuous cluster of high k_{sn} river channels is located in the central Nepal segment which goes from the Thakkhola graben in the west to the Ama Drime detachment in the east (Figure 2.6a). This segment also hosts the only region (Arun) with a positive correlation (0.4) between k_{sn} and MHT coupling (Figure 2.5i). The high k_{sn} cluster that defines the central Nepal segment is the closer to the range front (60-70 km) than any other cluster overlying a weakly coupled portion of the MHT, as well as being the longest continuous cluster (Figure 2.6a). Only west Nepal and Bhutan contain two parallel clusters of high k_{sn}, one close to the range front (30-50 km), and one coincident with the High Himalaya (80-120 km). The more foreland of these clusters overlie the strongly coupled portion of the MHT, and are located at a prominent lithologic boundary (LHS-GHS) suggesting that substrate erodibility plays a role in steepening the channels. However in both locations there is also

evidence for active rock uplift. In west Nepal, this high k_{sn} cluster coincides with a belt of microseismicity (Figure 2.6b), while in southwest Bhutan this high k_{sn} cluster coincides with young cooling ages (McQuarrie et al., 2014). In west Nepal, this has been interpreted to reflect an active MHT flat connecting a hinterland ramp with the more foreland ramp (Harvey et al., 2015), my analysis suggests that a similar geometry may be present in Bhutan. West Nepal and Bhutan are also home to the most prominent gaps in historic seismicity anywhere in the Himalaya.

The boundaries between high k_{sn} clusters are marked by range perpendicular rifts in southern Tibet, and in three cases (Himachal Pradesh – Uttarakhand, west Nepal – central Nepal, and central Nepal – east Nepal) by basement ridges in the India subsurface which are currently being subducted (Gahalaut and Kundu, 2012) (Figure 2.6a). The segments documented here are typically 300-400 km long with the exception of east Nepal which is only 125 km (Figure 2.6a and Table 2). This regular spacing suggests that segment boundaries are the product of a frequency-dependent mechanism, possibly buckling of the downgoing Indian plate. Buckling of slabs is a function of arc curvature and slab thickness which, in a homogenous medium, would result in a set wavelength and amplitude (Yin, 2000). Another possibility is that both rifts and k_{sn} segment boundaries are the geometric consequence of the curvature of the Himalayan arc.

Structural analysis of the deformed Siwalik Group at the leading edge of the MHT in western Nepal indicates the presence of north-striking lateral ramps in the MFT (Mugnier et al., 1999) that may extend far into the thrust wedge as ramps in the MHT. It is also observed that the intersection of Indian basement ridges and the MFT coincide spatially with the Uttarakhand - west Nepal, west Nepal – central Nepal, and central Nepal – east Nepal segment boundaries (Figure 2.6a) (Gahalaut and Kundu, 2012). The timing of ductile deformation and metamorphism varies across the Falzabad ridge (west Nepal – central Nepal boundary) suggesting that these differences could be explained by lateral ramps in the MHT produced by subduction of these features (Gibson et al., 2016). Based on our results these hypothesized lateral ramps may also explain the origin of the margins of the strain accumulation segments. A third possibility is that lateral ramps are generated by slip on syncollisional normal faults that strike at a high-angle to the thrust wedge, such as Thakkhola graben, Kaurik-Chango (Leo Pargil), Gurla Mandhata-Humla, and Yadong-Gulu (Figure 2.6a). Slip on these structures is coeval with thrusting below. Cyclic motion on these structures and thrusts below, including the MHT could produce orogen-normal shear zones that juxtapose contrasting structural levels.

2.5.5 Earthquakes

The High Himalaya overlies the weakly coupled portion of the MHT (Stevens and Avouac, 2015) and separates stably sliding southern Tibet from the strongly coupled portion of the MHT, suggesting that it acts as a dashpot storing interseismic strain (Bilham et al., 2001; Ader et al., 2012). In this view the dashpot accumulates strain imparted by India-Asia convergence until the stored stain is sufficient to overcome static friction on the strongly coupled portion of the MHT separating the dashpot from the toe of the thrust wedge (MFT). The spatial distribution of historical earthquake ruptures is an area of ongoing research (Ambraseys and Jackson, 2003; Kumar et al., 2006; Rajendran et al, 2015; Hossler et al., 2016). My analysis reveals a correspondence between ruptures and segments delineated by high k_{sn} clusters. Most rupture patches of great Himalayan earthquakes plot within a single segment (Figure 2.6b), suggesting that the boundaries between segments are, in many cases, capable of inhibiting rupture propagation. An exception is the 1505 Kumoan earthquake, whose magnitude has variously been interpreted to be between Mw 8.2 and 9.0 (Ambraseys and Jackson, 2003; Kumar et al., 2006) depending on the rupture length. If its rupture length is closer to the 9.0 estimated by Kumar et al. (2006), it would span the entire west Nepal segment and the eastern half of the Uttarakhand segment. The most striking correspondence between my analysis and the spatiotemporal distribution of historical earthquakes is in the west Nepal, central Nepal, and Bhutan segments. The west Nepal segment has not ruptured since 1505, Bhutan

(excluding the Shillong plateau) since 1713, while the central Nepal segment has ruptured three times in the last three hundred years 1803, 1934, and 2015 (Figure 2.6b). This apparent dichotomy may simply reflect our lack of knowledge of the Himalayan seismic cycle, or it may indicate that the central Nepal segment accumulates and releases strain more efficiently than its neighbors. This hypothesis is supported by several considerations. First it hosts the longest continuous high k_{sn} cluster (380 km) overlying a weakly coupled portion of the MHT (Figure 2.6a). Second this high k_{sn} cluster is located closer the toe of the thrust wedge than any other cluster. Finally it is located in the most orthogonally convergent part of the orogen so none of the convergence is segregated into lateral motion. In contrast, west Nepal and Bhutan each host two narrow (30-50 km wide), short (80-230 km long), high k_{sn} clusters the more foreland of which overlies a strongly coupled portion of the MHT. West Nepal lies within the obliquely convergent western half of the Himalaya in which some portion of India-Asia convergence has been hypothesized to be segregated into west directed lateral motion (Styron et al., 2010; Murphy et al., 2014; Whipp et al., 2014). Similarly, the paucity of seismicity in Bhutan (Figure 2.6a) has been attributed to strain partitioning between the range and the Shillong plateau (Figure 2.1) (Najman et al., 2016). Changes in the size of the "seismic dashpot", its proximity to the toe of the thrust wedge, and strain partitioning provide a plausible explanation for the seemingly disparate seismic cycles of west Nepal, central Nepal, and Bhutan.

2.5.6 Drainage Network

The drainage network of major Himalayan rivers is segmented similarly to channel steepness (Figure 2.1) suggesting that channel steepness and drainage network patterns form in response to the same tectonic forcing. The Nepal segments are characterized by large catchments in which numerous parallel drainages area collected into a few pour points at the range front. This process is driven by active anticlines in the sub-Himalaya which grow more rapidly than the individual drainages can incise through them producing lower river reaches that flow parallel to the range front for 70-100 km. The result is a 760 km long segment of the range hosts only three catchments, the Karnali, Narayani, and Arun. In west Nepal, near the plateau boundary, the Karnali river's upper reaches, the Mugu in the west and Dolpo Karnali in the east, flow along the axis of the Dolpo syncline paralleling the range front for 100 km and 150 km, respectively. Axial drainage along the leading edge of the growing Dolpo anticline (Cannon and Murphy, 2014) in the Karnali's two main trunk channels funnels into a zig-zag drainage pattern in the largest erosional bite anywhere in the Himalaya (Figure 2.1). The lower reaches of the Karnali contain two hairpin turns suggesting recent drainage network reorganization by active anticlines at the range front. The 270 km long Bhutan segment contains five catchments, the largest of which host a parallel drainage network characteristic of steep active mountain fronts. Activity along the range front in Bhutan is expressed differently than in the western and central Himalaya. To the west, the range front is

characterized by closely spaced network of anticlines separated from the range by broad flat valleys. Whereas in Bhutan foothill-anticlines are intermittent, duns are narrow, the MFT is difficult to recognize, and the first topographic step is commonly associated with the MBT. However, these differences are minor compared to the presence of the Shillong plateau in the eastern Bhutanese foreland. The Shillong plateau is located 100 km south of the range front and has over a kilometer of relief above the surrounding foreland basin. It has been characterized as a popup structure bounded to the north and south by oppositely dipping thrusts, however its significance for the thrust wedge and its implications for the interaction of climate of tectonics are debated (Adams, 2014; Bilham and England, 2001; Clark and Bilham, 2008; Grujic et al., 2006; Najman et al., 2016). Whatever role the Shillong plateau plays in accommodating India-Asia convergence, it is clear that at the range front either strain is accumulating at a lower rate than in Nepal, or else is concentrated on the MBT as all drainages flow across the MFT with no deflection.

2.6 Discussion

Despite numerous geologic and geophysical studies of the Himalayan plate boundary, basic questions remain unanswered. Foremost is the geometry of the subduction interface. Seismic reflection surveys have resolved ramps and flats in the MHT (Hauck et al., 1998), although seismic refraction surveys have

failed to do so (Nábělek et al., 2009). Geodesists are able to model the pattern of MHT fault coupling using a single inclined plane by assuming that all significant variability in the position and dip of MHT ramps is located within strongly coupled portions (Bollinger et al., 2004b; Jouanne et al., 2004; Stevens and Avouac, 2015). Nevertheless, there is evidence for the existence of MHT ramps located within the weakly coupled portions of the MHT. Balanced cross sections (DeCelles et al., 1998; McQuarrie and Ehlers, 2015; Robinson, 2008; Schelling and Arita, 1991), electrical conductivity (Lemonnier et al., 1999), tectonic geomorphology (Figure 2.2c) (Cannon and Murphy, 2014; Seeber and Gornitz, 1983), microseismicity (Figure 2.3b) (Pandey et al., 1999), and Bayesian modeling of possible MHT geometries (Elliott et al., 2016) all suggest the presence of thrust ramps in essentially the same locations at the boundary between the strongly and weakly coupled portions of the MHT. My analysis in west Nepal and Bhutan indicates the presence of rapid rock uplift in the hinterland above weakly coupled portions of the MHT (Figure 2.2c). Changes in the position of high k_{sn} clusters are most pronounced between west Nepal and central Nepal where high k_{sn} clusters overlying weakly coupled portions of the MHT are offset by 60 km along a sharp boundary coincident with the GMH core complex (Figure 2.6a). This strongly suggests the geometry of the MHT changes along strike. That the largest offset of high k_{sn} clusters occurs here has kinematic significance. GMH is thought to be an extensional step over feeding slip from the right lateral Karakorum fault in southern Tibet into the right lateral cross-orogen West Nepal

Fault System (WNFS) (Murphy et al., 2014). The combined Karakorum Fault and WNFS, in concert with the MHT and MFT form a tectonic sliver in which convergence is hypothesized to be partitioned between range normal and range parallel components (Styron et al., 2010; Murphy et al., 2014). The WNFS crosses the west Nepal segment in a NW-SE direction and divides the western obliquely convergent Himalaya from the central orthogonally convergent Himalaya. Central Nepal is located in the most orthogonally convergent part of the arc and appears to have the most rapid recurrence of Mw > 7 earthquakes (Figure 2.6c). Convergence obliquity and great earthquake recurrence times increase to the west and east. The degree to which convergence obliquity modifies the geometry of the plate margin or modulates its seismic behavior remains an outstanding question.

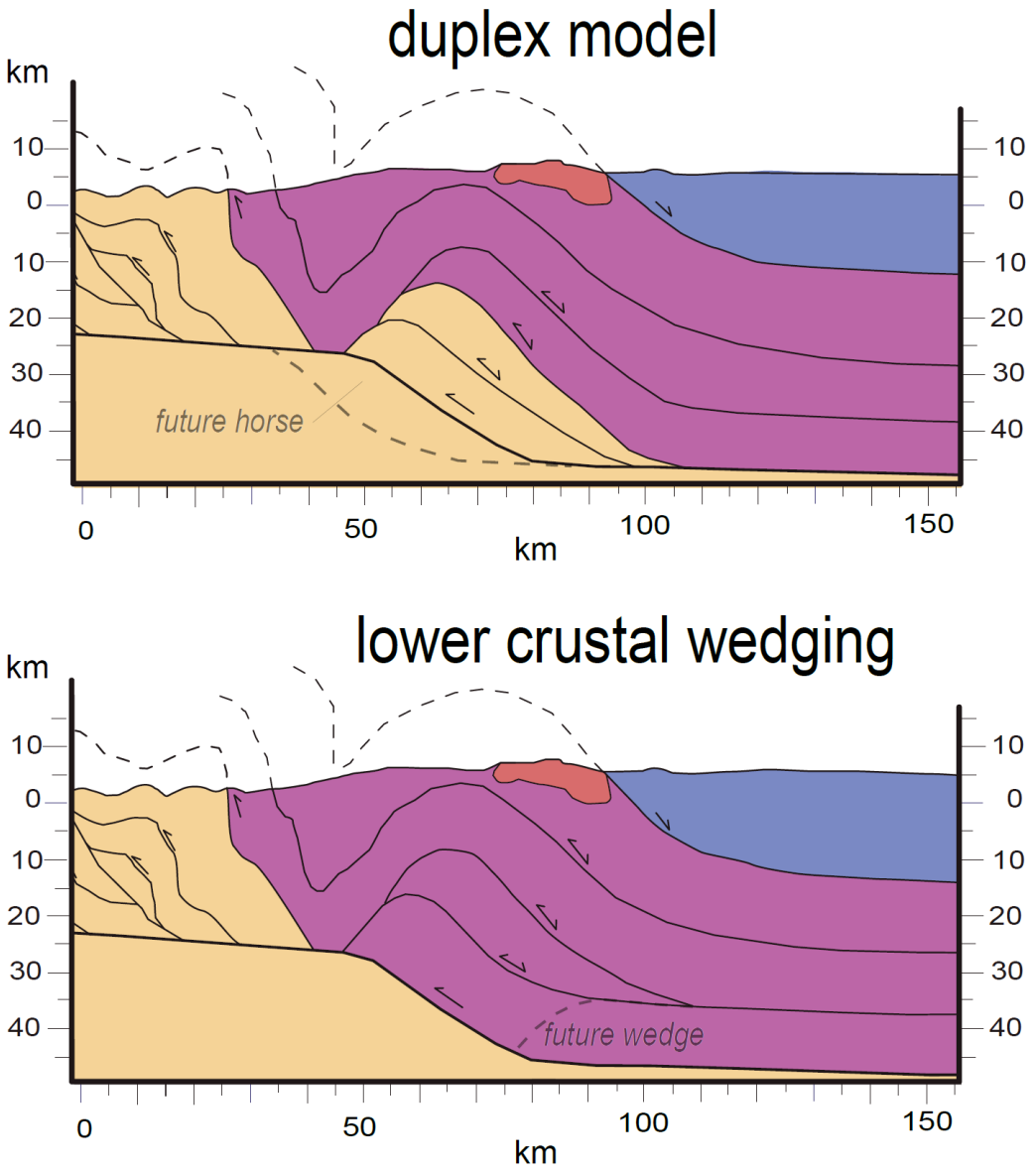

Figure 2.7. a) Underplating duplex model for hinterland ductile duplex in west Nepal. b) Tectonic wedging duplex model for hinterland ductile duplex in west Nepal.

Recent internal deformation of the Himalayan thrust wedge appears to be dominated by duplexing (Bollinger et al., 2004; Herman et al., 2010). Duplexing is characterized by a high ratio of crustal thickening to surficial horizontal shortening. This criterion is met in the hinterland of west Nepal and Bhutan where broad anticlines record vertical thickening to surficial horizontal shortening ratios of between 2:1 to 5:1, depending on the thickness of the repeated layer, requiring either blind reverse faulting or duplexing. Duplexes typically form by underplating, whereby slices of the footwall are accreted to the hanging wall (Figure 2.7a), however, no structural window in the High Himalaya has been documented which provides an unambiguous view of the mechanism thickening the hinterland. Alternatively, in the ductiley deforming lower crust, repeated tectonic wedging (Webb et al., 2007; Yin, 2006) at the BPT could also produce a duplex which is restricted to the hanging wall of the MHT (Figure 2.7b). BPT tectonic wedging is a hybrid model combining the idea of a ductiley deforming medium bounded below by the MHT and above by a mid-crustal discontinuity with the opposite shear sense, i.e. channel flow, with the tectonic wedge insertion model. In this view, hinterland thickening results from repeated insertion of ductile wedges along a ramp which controls the position of the MHT-BPT forming an antiformal stack. As the active wedge is inserted at the base of the stack, it forces the preceding wedges up building topography and steepening river channels at the surface. The brittle upper crust overlying the stack absorbs elastic strain imparted by the south directed sliding of southern Tibet recorded by GPS

(Ader et al., 2012). This mechanism provides a plausible explanation for the coincidence of interseismic strain, high k_{sn} clusters, and the highest topography in the range without calling upon ramp migration + delayed erosion (Grandin et al., 2012) or an unbalanced earthquake cycle (Bilham and Ambraseys, 2005; Meade, 2010), by allowing the lower crust to accommodate more permanent strain than the upper crust. The greater velocity of the lower crust relative to the upper crust predicted by channel flow models (Beaumont et al., 2001; Jamieson et al., 2006) produces a south-directed lower-crustal flow which can be invoked to drive the insertion of wedges of ductile lower crust. Recently several "midcrustal discontinuities" have been identified within the GHS of Nepal predating the main period of the linked MCT-STD motion in the late Early to Middle Miocene (Carosi et al., 2010; Larson et al., 2015; Larson and Cottle, 2014; Montomoli et al., 2013). These have been interpreted as shear zones bounding horses within a hinterland duplex which was exhumed during thrusting on the MCT (Larson et al., 2015). If this interpretation is correct, it provides us with a picture of what modern tectonic wedging at the BPT may look like. These duplexes create permanent uplift by thickening the lower crust while storing elastic strain in the upper crust, the net result of which is a collocated increase in rock-uplift rate and elastic strain. Currently, I cannot distinguish between these two duplexing models although the presence of Lesser Himalayan Sequence isotopic signatures in anatectic melts of the Gurla Mandhata core complex provides compelling evidence for the underplating model (Murphy, 2007).

2.7 Conclusions

Rapid rock uplift in the Himalaya, recorded by k_{sn} analysis, is predominantly localized within the High Himalaya above weakly coupled portions of the MHT. The timescales required to encode k_{sn} signals in the landscape (10^4-10^5 years) allows this approach to bridge the time gap between GPS datasets and low-temperature thermochronology. Regions of rapid rock uplift recorded here are offset across Hima-Tibetan rifts, the largest offset occurs between west and central Nepal along a previously proposed strain partitioning boundary. These regions of rapid rock uplift separate stably sliding southern Tibet from the Himalayan seismogenic zone. As such, they accumulate interseismic strain, storing it until it is sufficient to overcome static friction on the strongly coupled portion of MHT. Segmenting the Himalaya based on high k_{sn} clusters reveals an association with the spatiotemporal distribution of historical great earthquakes. This indicates that the size of high k_{sn} clusters and their distance from the toe of the thrust wedge have an impact on the recurrence time of great earthquakes.

2.8 References

Adams, B., Whipple, K., Hodges, K., and Heimsath, A., 2016, In-situ development of high-elevation, low-relief landscapes via duplex deformation in the Eastern Himalayan hinterland, Bhutan: Journal of Geophysical Research: Earth Surface, v. 121, p. 294-319.

Adams, B.A., 2014, Tectonic and climatic influence on the evolution of the Bhutan Himalaya, Arizona State University.

Ader, T., Avouac, J.P., Liu-Zeng, J., Lyon-Caen, H., Bollinger, L., Galetzka, J., Genrich, J., Thomas, M., Chanard, K., and Sapkota, S.N., 2012, Convergence rate across the Nepal Himalaya and interseismic coupling on the Main Himalayan Thrust: Implications for seismic hazard: Journal of Geophysical Research: Solid Earth (1978–2012), v. 117, p. B04403.

Ambraseys, N., and Jackson, D., 2003, A note on early earthquakes in northern India and southern Tibet: Current Science, v. 84, p. 570-582.

Avouac, J.-P., 2003, Mountain building, erosion, and the seismic cycle in the Nepal Himalaya: Advances in Geophysics, v. 46, p. 1-80.

Beaumont, C., Jamieson, R., Nguyen, M., and Lee, B., 2001, Himalayan tectonics explained by extrusion of a low-viscosity crustal channel coupled to focused surface denudation: Nature, v. 414, p. 738-742.

Berthet, T., Ritz, J.-F., Ferry, M., Pelgay, P., Cattin, R., Drukpa, D., Braucher, R., and Hetényi, G., 2014, Active tectonics of the eastern Himalaya: New

constraints from the first tectonic geomorphology study in southern Bhutan: Geology, v. 42, p. 427-430.

Bilham, R., and Ambraseys, N., 2005, Apparent Himalayan slip deficit from the summation of seismic moments for Himalayan earthquakes, 1500–2000: Current Science, v. 88, p. 1658-1663.

Bilham, R., and England, P., 2001, Plateau 'pop-up'in the great 1897 Assam earthquake: Nature, v. 410, p. 806-809.

Bilham, R., Gaur, V.K., and Molnar, P., 2001, Himalayan seismic hazard: Science, v. 293, p. 1442-1444.

Bilham, R., Larson, K., Freymueller, J., Jouanne, F., Le Fort, P., Leturmy, P., Mugnier, J., Gamond, J., Glot, J., and Martinod, J., 1997, GPS measurements of present-day convergence across the Nepal Himalaya: Nature, v. 386, p. 61-64.

Bollinger, L., Avouac, J., Beyssac, O., Catlos, E., Harrison, T., Grove, M., Goffé, B., and Sapkota, S., 2004a, Thermal structure and exhumation history of the Lesser Himalaya in central Nepal: Tectonics, v. 23, p. TC5015.

Bollinger, L., Avouac, J., Cattin, R., and Pandey, M., 2004b, Stress buildup in the Himalaya: Journal of Geophysical Research: Solid Earth (1978–2012), v. 109, p. B11405.

Bollinger, L., Perrier, F., Avouac, J.P., Sapkota, S., Gautam, U., and Tiwari, D., 2007, Seasonal modulation of seismicity in the Himalaya of Nepal: Geophysical Research Letters, v. 34, p. L08304.

Cannon, J., and Murphy, M., 2014, Active lower crustal deformation and Himalayan seismic hazard revealed by stream channels and regional geology: Tectonophysics, v. 633, p. 34-42.

Cannon, J.M.R., 2011, The East Jhomolari Fault System and the timing of east-west extension in NW Bhutan, Masters Thesis, The University of Texas at El Paso, retrieved from Digital Commons, publication number AAI1498273.

Carosi, R., Montomoli, C., Rubatto, D., and Visonà, D., 2010, Late Oligocene high-temperature shear zones in the core of the Higher Himalayan Crystallines (Lower Dolpo, western Nepal): Tectonics, v. 29, p. TC4029.

Cattin, R., and Avouac, J., 2000, Modeling mountain building and the seismic cycle in the Himalaya of Nepal: Journal of Geophysical Research: Solid Earth (1978–2012), v. 105, p. 13389-13407.

Clark, M.K., and Bilham, R., 2008, Miocene rise of the Shillong Plateau and the beginning of the end for the Eastern Himalaya: Earth and Planetary Science Letters, v. 269, p. 337-351.

Cooper, F., Hodges, K.V., Parrish, R., Roberts, N., and Horstwood, M., 2015, Synchronous N-S and E-W extension at the Tibet-to-Himalaya transition in NW Bhutan: Tectonics, v. 34, p. 1375-1395.

Davis, W., 1902, Baselevel, grade and peneplain: The Journal of Geology, v. 10, p. 77-111.

DeCelles, P., Gehrels, G., Quade, J., Ojha, T., Kapp, P., and Upreti, B., 1998, Neogene foreland basin deposits, erosional unroofing, and the kinematic history of the Himalayan fold-thrust belt, western Nepal: Geological Society of America Bulletin, v. 110, p. 2-21.

Elliott, J., Jolivet, R., González, P., Avouac, J.-P., Hollingsworth, J., Searle, M., and Stevens, V., 2016, Himalayan megathrust geometry and relation to topography revealed by the Gorkha earthquake: Nature Geoscience, v. 9, p. 174-180.

Gahalaut, V., and Kundu, B., 2012, Possible influence of subducting ridges on the Himalayan arc and on the ruptures of great and major Himalayan earthquakes: Gondwana Research, v. 21, p. 1080-1088.

Gibson, R., Godin, L., Kellett, D.A., Cottle, J.M., and Archibald, D., 2016, Diachronous deformation along the base of the Himalayan metamorphic core, west-central Nepal: Geological Society of America Bulletin, p. B31328. 1.

Godin, L., Gleeson, T., Searle, M., Ullrich, T., and Parrish, R.R., 2006a, Locking of southward extrusion in favour of rapid crustal-scale buckling of the Greater Himalayan sequence, Nar valley, central Nepal: Geological Society, London, Special Publications, v. 268, p. 269.

Godin, L., Grujic, D., Law, R., and Searle, M., 2006b, Channel flow, ductile extrusion and exhumation in continental collision zones: an introduction: Geological Society, London, Special Publications, v. 268, p. 1-23.

Grandin, R., Doin, M.-P., Bollinger, L., Pinel-Puysségur, B., Ducret, G., Jolivet, R., and Sapkota, S.N., 2012, Long-term growth of the Himalaya inferred from interseismic InSAR measurement: Geology, v. 40, p. 1059-1062.

Grujic, D., Coutand, I., Bookhagen, B., Bonnet, S., Blythe, A., and Duncan, C., 2006, Climatic forcing of erosion, landscape, and tectonics in the Bhutan Himalayas: Geology, v. 34, p. 801-804.

Grujic, D., Hollister, L.S., and Parrish, R.R., 2002, Himalayan metamorphic sequence as an orogenic channel: insight from Bhutan: Earth and Planetary Science Letters, v. 198, p. 177-191.

Hack, J.T., 1957, Studies of Longitudinal Stream Profiles in Virginia and Maryland, U.S. Government Printing Office.

Harvey, J.E., Burbank, D.W., and Bookhagen, B., 2015, Along-strike changes in Himalayan thrust geometry: Topographic and tectonic discontinuities in western Nepal: Lithosphere, v. 7, p. 511-518.

Hauck, M., Nelson, K., Brown, L., Zhao, W., and Ross, A., 1998, Crustal structure of the Himalayan orogen at∼ 90 east longitude from Project INDEPTH deep reflection profiles: Tectonics, v. 17, p. 481-500.

Herman, F., Copeland, P., Avouac, J.-P., Bollinger, L., Mahéo, G., Le Fort, P., Rai, S., Foster, D., Pêcher, A., and Stüwe, K., 2010, Exhumation, crustal deformation, and thermal structure of the Nepal Himalaya derived from the inversion of thermochronological and thermobarometric data and

modeling of the topography: Journal of Geophysical Research, v. 115, p. B06407.

Hirth, G., and Tullis, J., 1992, Dislocation creep regimes in quartz aggregates: Journal of Structural Geology, v. 14, p. 145-159.

Hodges, K.V., Wobus, C., Ruhl, K., Schildgen, T., and Whipple, K., 2004, Quaternary deformation, river steepening, and heavy precipitation at the front of the Higher Himalayan ranges: Earth and Planetary Science Letters, v. 220, p. 379-389.

Hossler, T., Bollinger, L., Sapkota, S., Lavé, J., Gupta, R., and Kandel, T., 2016, Surface ruptures of large Himalayan earthquakes in Western Nepal: Evidence along a reactivated strand of the Main Boundary Thrust: Earth and Planetary Science Letters, v. 434, p. 187-196.

Jackson, M.E., and Bilham, R., 1994, 1991–1992 GPS measurements across the Nepal Himalaya: Geophysical research letters, v. 21, p. 1169-1172.

Jamieson, R., Beaumont, C., Nguyen, M., and Grujic, D., 2006, Provenance of the Greater Himalayan Sequence and associated rocks: predictions of channel flow models: Geological Society, London, Special Publications, v. 268, p. 165.

Jouanne, F., Mugnier, J.-L., Gamond, J., Fort, P.L., Pandey, M., Bollinger, L., Flouzat, M., and Avouac, J., 2004, Current shortening across the Himalayas of Nepal: Geophysical Journal International, v. 157, p. 1-14.

Kellett, D., Grujic, D., Warren, C., Cottle, J., Jamieson, R., and Tenzin, T., 2010, Metamorphic history of a syn-convergent orogen-parallel detachment: The South Tibetan detachment system, Bhutan Himalaya: Journal of Metamorphic Geology, v. 28, p. 785-808.

Kirby, E., and Whipple, K., 2001, Quantifying differential rock-uplift rates via stream profile analysis: Geology, v. 29, p. 415-418.

Kirby, E., and Whipple, K.X., 2012, Expression of active tectonics in erosional landscapes: Journal of Structural Geology, v. 44, p. 54-75.

Kumar, S., Wesnousky, S.G., Rockwell, T.K., Briggs, R.W., Thakur, V.C., and Jayangondaperumal, R., 2006, Paleoseismic evidence of great surface rupture earthquakes along the Indian Himalaya: Journal of Geophysical Research: Solid Earth (1978–2012), v. 111, p. B03304.

Larson, K.P., Ambrose, T.K., Webb, A.G., Cottle, J.M., and Shrestha, S., 2015, Reconciling Himalayan midcrustal discontinuities: The Main Central thrust system: Earth and Planetary Science Letters, v. 429, p. 139-146.

Larson, K.P., and Cottle, J.M., 2014, Midcrustal discontinuities and the assembly of the Himalayan midcrust: Tectonics, v. 33, p. 718-740.

Lavé, J., and Avouac, J., 2001, Fluvial incision and tectonic uplift across the Himalayas of central Nepal: Journal of Geophysical Research: Solid Earth (1978–2012), v. 106, p. 26561-26591.

Lemonnier, C., Marquis, G., Perrier, F., Avouac, J.P., Chitrakar, G., Kafle, B., Sapkota, S., Gautam, U., Tiwari, D., and Bano, M., 1999, Electrical

structure of the Himalaya of central Nepal: High conductivity around the mid-crustal ramp along the MHT: Geophysical Research Letters, v. 26, p. 3261-3264.

Long, S., McQuarrie, N., Tobgay, T., Grujic, D., and Hollister, L., 2011, Geologic map of Bhutan: Journal of Maps, v. 7, p. 184-192.

Mackin, J.H., 1948, Concept of the graded river: Geological Society of America Bulletin, v. 59, p. 463-512.

McCallister, A.T., Taylor, M.H., Murphy, M., Styron, R.H., and Stockli, D.F., 2014, Thermochronologic constraints on the late Cenozoic exhumation history of the Gurla Mandhata metamorphic core complex, Southwestern Tibet: Tectonics, v. 33, p. 27-52.

McDermott, J.A., Hodges, K.V., Whipple, K.X., Van Soest, M.C., and Hurtado Jr, J.M., 2015, Evidence for Pleistocene low-angle normal faulting in the Annapurna-Dhaulagiri Region, Nepal: The Journal of Geology, v. 123, p. 133-151.

McDermott, J.A., Whipple, K.X., Hodges, K.V., and Soest, M.C., 2013, Evidence for Plio-Pleistocene north-south extension at the southern margin of the Tibetan Plateau, Nyalam region: Tectonics, v. 32, no. 3, p. 317-333.

McQuarrie, N., and Ehlers, T.A., 2015, Influence of thrust belt geometry and shortening rate on thermochronometer cooling ages: Insights from thermokinematic and erosion modeling of the Bhutan Himalaya: Tectonics, v. 34, no. 6, p. 1055-1079.

McQuarrie, N., Tobgay, T., Long, S.P., Reiners, P.W., and Cosca, M.A., 2014, Variable exhumation rates and variable displacement rates: Documenting recent slowing of Himalayan shortening in western Bhutan: Earth and Planetary Science Letters, v. 386, p. 161-174.

Meade, B.J., 2010, The signature of an unbalanced earthquake cycle in Himalayan topography?: Geology, v. 38, p. 987-990.

Montomoli, C., Iaccarino, S., Carosi, R., Langone, A., and Visonà, D., 2013, Tectonometamorphic discontinuities within the Greater Himalayan Sequence in Western Nepal (Central Himalaya): Insights on the exhumation of crystalline rocks: Tectonophysics, v. 608, p. 1349-1370.

Murphy, M., Taylor, M., Gosse, J., Silver, C., Whipp, D., and Beaumont, C., 2014, Limit of strain partitioning in the Himalaya marked by large earthquakes in western Nepal: Nature Geoscience, v. 7, p. 38-42.

Murphy, M., Yin, A., Kapp, P., Harrison, T., Manning, C., Ryerson, F., Lin, D., and Jinghui, G., 2002, Structural evolution of the Gurla Mandhata detachment system, southwest Tibet: Implications for the eastward extent of the Karakoram fault system: Geological Society of America Bulletin, v. 114, p. 428-447.

Murphy, M.A., 2007, Isotopic characteristics of the Gurla Mandhata metamorphic core complex: Implications for the architecture of the Himalayan orogen: Geology, v. 35, p. 983-986.

Nábělek, J., Hetényi, G., Vergne, J., Sapkota, S., Kafle, B., Jiang, M., Su, H., Chen, J., and Huang, B.-S., 2009, Underplating in the Himalaya-Tibet collision zone revealed by the Hi-CLIMB experiment: Science, v. 325, p. 1371-1374.

Najman, Y., Bracciali, L., Parrish, R.R., Chisty, E. and Copley, A., 2016, Evolving strain partitioning in the Eastern Himalaya: The growth of the Shillong Plateau. Earth and Planetary Science Letters, v. 433, p.1-9.

Pandey, M., Tandukar, R., Avouac, J., Lave, J., and Massot, J., 1995, Interseismic strain accumulation on the Himalayan crustal ramp (Nepal): Geophysical Research Letters, v. 22, p. 751-754.

Pandey, M., Tandukar, R., Avouac, J., Vergne, J., and Héritier, T., 1999, Seismotectonics of the Nepal Himalaya from a local seismic network: Journal of Asian Earth Sciences, v. 17, p. 703-712.

Rajendran, C. P., John, B., & Rajendran, K., 2015, Medieval pulse of great earthquakes in the central Himalaya: Viewing past activities on the frontal thrust. Journal of Geophysical Research: Solid Earth, v. 120, p. 1623-1641.

Robinson, D.M., 2008, Forward modeling the kinematic sequence of the central Himalayan thrust belt, western Nepal: Geosphere, v. 4, p. 785-801.

Schelling, D., and Arita, K., 1991, Thrust tectonics, crustal shortening, and the structure of the far-eastern Nepal Himalaya: Tectonics, v. 10, p. 851-862.

Searle, M.P., and Godin, L., 2003, The south Tibetan detachment and the Manaslu Leucogranite: A structural reinterpretation and restoration of the Annapurna-Manaslu Himalaya, Nepal: The Journal of Geology, v. 111, p. 505-523.

Seeber, L., and Gornitz, V., 1983, River profiles along the Himalayan arc as indicators of active tectonics: Tectonophysics, v. 92, p. 335-367.

Stevens, V., and Avouac, J., 2015, Interseismic coupling on the main Himalayan thrust: Geophysical Research Letters, v. 42, p. 5828-5837.

Styron, R.H., Taylor, M.H., and Murphy, M.A., 2011, Oblique convergence, arc-parallel extension, and the role of strike-slip faulting in the High Himalaya: Geosphere, v. 7, p. 582-596.

Sundell, K.E., Taylor, M.H., Styron, R.H., Stockli, D.F., Kapp, P., Hager, C., Liu, D., and Ding, L., 2013, Evidence for constriction and Pliocene acceleration of east-west extension in the North Lunggar rift region of west central Tibet: Tectonics, v. 32, p. 1454-1479.

Tullis, J., and Yund, R., 1992, The brittle-ductile transition in feldspar aggregates: An experimental study: International Geophysics, v. 51, p. 89-117.

Webb, A.A.G., Yin, A., Harrison, T.M., Célérier, J., and Burgess, W.P., 2007, The leading edge of the Greater Himalayan Crystalline complex revealed in the NW Indian Himalaya: Implications for the evolution of the Himalayan orogen: Geology, v. 35, p. 955-958.

Whipp, D.M., Beaumont, C., and Braun, J., 2014, Feeding the “aneurysm”: Orogen-parallel mass transport into Nanga Parbat and the western Himalayan syntaxis: Journal of Geophysical Research: Solid Earth, v. 119, p. 5077-5096.

Wobus, C., Heimsath, A., Whipple, K., and Hodges, K., 2005, Active out-of-sequence thrust faulting in the central Nepalese Himalaya: Nature, v. 434, p. 1008-1011.

Wobus, C., Whipple, K.X., Kirby, E., Snyder, N., Johnson, J., Spyropolou, K., Crosby, B., and Sheehan, D., 2006, Tectonics from topography: Procedures, promise, and pitfalls: Geological Society, London, Special Publications, v. 398, p. 55.

Wu, C., Nelson, K., Wortman, G., Samson, S.D., Yue, Y., Li, J., Kidd, W., and Edwards, M., 1998, Yadong cross structure and South Tibetan Detachment in the east central Himalaya (89–90 E): Tectonics, v. 17, p. 28-45.

Yin, A., 2000, Mode of Cenozoic east-west extension in Tibet suggesting a common origin of rifts in Asia during the Indo-Asian collision: Journal of Geophysical Research, v. 105, p. 21,745-21,759.

—, 2006, Cenozoic tectonic evolution of the Himalayan orogen as constrained by along-strike variation of structural geometry, exhumation history, and foreland sedimentation: Earth-Science Reviews, v. 76, p. 1-131.

Chapter 3 Implications of subsidence analysis on dynamic topography in the Gulf of Mexico

3.1 Chapter Summary

Geodynamic models predict a wave of dynamic subsidence with ~1 km amplitude swept across the Gulf of Mexico (GoM) between 120 Ma and the present as the Farallon slab passed beneath it. I tested this by conducting a subsidence analysis of the abyssal-plain using eight deep seismic reflection lines traversing the northern GoM. Results show three episodes of enhanced subsidence: Early Cretaceous (142-97 Ma), early Cenozoic (65-49 Ma), and late Cenozoic (34 Ma – Recent). I attribute the first, which immediately follows cessation of sea floor spreading, to thermal contraction and density-driven subsidence, and requires no additional dynamic component. The second is synchronous with peak Laramide orogenesis and consistent with asymmetric basin filling. It does not correlate with the predictions of a dynamic subsidence sweep. Early Cenozoic subsidence is maximized in the west where models predict the onset of dynamic support and minimized in the east where models predict maximum rates of dynamic subsidence. The third correlates with rapid progradation and aggradation of the GoM shelf-margin wedge accompanying enhanced sediment delivery to the northeastern GoM. Flexure beneath the sediment load accounts for 78–100% of this episodes subsidence. The magnitude and patterns of GoM subsidence can be explained by thermal contraction,

asymmetric basin filling, and flexure without invoking dynamic subsidence due to sublithospheric passage of a subducted slab. Therefore, I suggest the downward force imparted by the sinking Farallon slab was either attenuated by the overlying mantle, or was insufficient to overcome the flexural rigidity of the lithosphere beneath the GoM.

3.2 Introduction

Most topography on earth is supported isostatically by vertical differences in the density of the lithosphere (Watts, 2001). However, sublithospheric mantle circulation may drive deflections from isostatic equilibrium by generating traction on the base of the lithosphere, i.e., within the asthenosphere, capable of vertically deflecting the overlying lithosphere (Flament et al., 2013; Gurnis, 1990; Hager et al., 1985). The resulting dynamic subsidence is a downward deflection of the lithosphere and may be produced by viscous flow around a high density anomaly, e.g., a subducted slab, sinking into the mantle. Deflections are thought to be long-wavelength, 100-10,000 km, and low-amplitude, 100-2000 m, although estimates of the maximum amplitude vary widely (Braun, 2010; Flament et al., 2013; Flament et al., 2014; Gurnis, 1990; Kaban et al., 2004; Molnar et al., 2015; Shephard et al., 2014). Models of modern dynamic topography predict a kilometer deep dynamic low in the central and eastern Gulf of Mexico (GoM) driven by the still-sinking Farallon slab (Forte et al., 2010) now in the deep

mantle below Florida (Bunge and Grand, 2000). By reconstructing the past position of the western North American convergent margin and assuming a Farallon-North America convergence rate, Shephard et al. (2014) and Flament et al. (2014) predicted that the predicted modern dynamic low began as a kilometer-deep trough in the western GoM at 120 Ma, which then migrated across the gulf as the Farallon slab passed below (Figure 3.1b). The predicted trough reaches its maximum deflection in the western GoM at 70 Ma and then sweeps east-northeast reaching the eastern GoM by 40 Ma (Figure 3.1a and c). As the wave migrates east it gradually becomes longer wavelength and lower amplitude as the vertical distance to the slab increases and intervening asthenosphere attenuates the downward force on the overlying lithosphere. Feng et al. (1994) examined subsidence in deepwater of the western GoM using seismic stratigraphy at three sites offshore northern Veracruz (Figure 3.1a) and found rapid subsidence from 66 Ma to 40 Ma (Figure 3.1c), which they attributed to emplacement of Laramide thrusts in eastern Mexico. I expand their analysis of abyssal GoM subsidence by conducting geohistory analyses of eight GulfSPAN seismic reflection profiles provided by *ION Geophysical* (Figure 3.2). All locations are basinward of the toe of the sediment wedge (Figure 3.1a), which spans the northern Gulf. Results are interpreted in terms of thermal history, regional sedimentation, and flexure; they are then compared with model predictions for the predicted timing, magnitude, and distribution of dynamic subsidence.

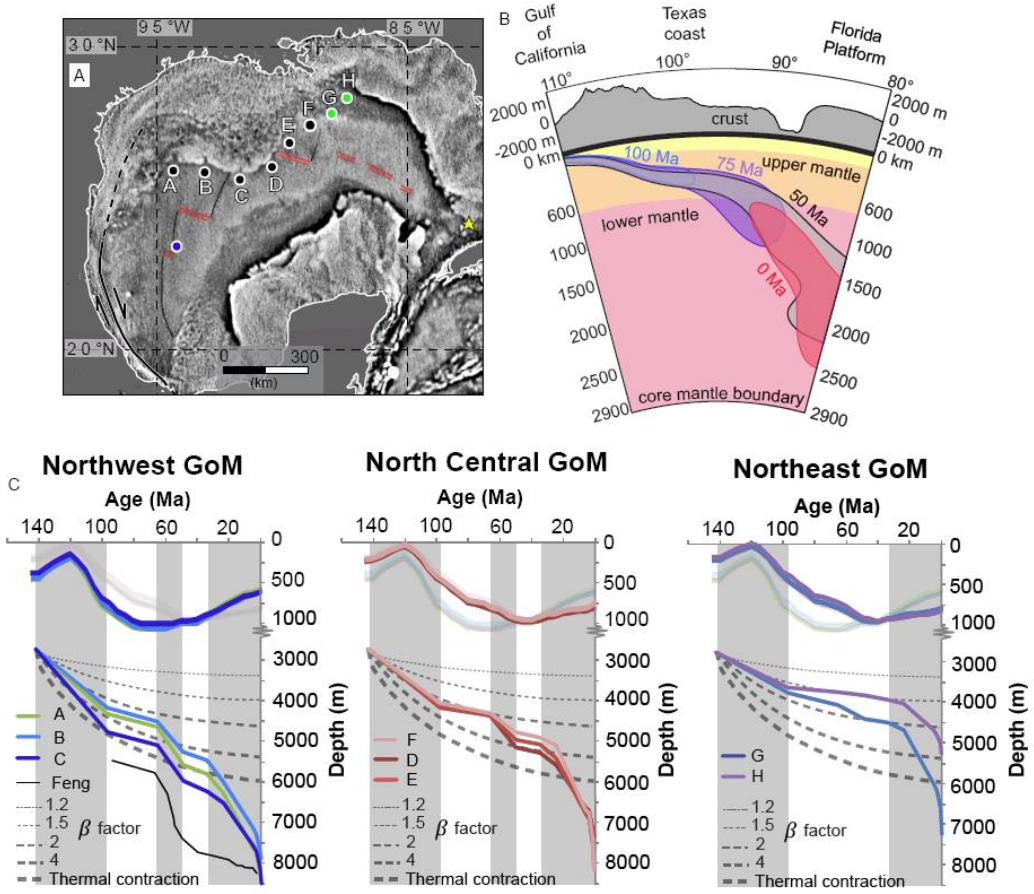

Figure 3.1. a) Gulf of Mexico free air gravity map (Sandwell et al., 2014) subsidence analysis locations are shown as colored circles. Interpreted extinct spreading ridges and transforms are shown as red and black line, respectively. Yellow star is approximate pole of rotation for GoM opening. b) Schematic Farallon subduction history after Shephard et al., 2014 showing predicted slab location and geometry from 100 Ma to the present. c) Subsidence curves (bottom) and predicted dynamic subsidence curves (top) from Shephard et al., 2014. Note the different depth scales on the y-axis. Dynamic subsidence curves the western, central, and eastern GoM are in bolded in their respective graphs to highlight migration of the dynamic subsidence wave. Dashed grey lines show subsidence predicted for different stretching (β) factors. Vertical grey bars highlight the observed episodes of enhanced subsidence in the middle Cretaceous, early Cenozoic, and late Cenozoic.

3.3 Tectonic Setting

Initial rifting of the GoM occurred in the early Late Triassic Eagle Mills rift spanning southern Arkansas and central Texas (Moy and Traverse, 1986). Rifting was followed by deposition of a 2-5 km thick layer of evaporites (Salvador, 1987) that was extended and eventually divided by seafloor spreading into the Louann and Campeche salts in the northern and southern GoM, respectively (Hudec et al., 2013; Pindell, 1985). Opening was accomplished by 800-1000 km of translation and ~45° counterclockwise rotation of the Yucatan Peninsula along a right lateral continent-ocean transform fault running the length of eastern Mexico around a pole of rotation in the straits of Florida (Bird et al., 2005; Pindell and Kennan, 2009). The GoM is thought to have briefly achieved sea-floor spreading from 158-140 Ma (Pindell and Kennan, 2009), although no magnetic reversals are discernible and the igneous basement has yet to be drilled. The presence of oceanic crust is inferred from basin depth, as seismic lines reveal > 14 km of sediment accumulated across the northern GoM (Figure 3.2). Refraction studies also point to the presence of crust with oceanic crustal velocities (7-8 $km \cdot s^{-1}$) at 15-20 km depths (Eddy et al., 2014; Van Avendonk et al., 2015). Finally, gravity maps show ridges and transforms interpreted to have formed during initial sea floor spreading (Figure 3.1a) (Sandwell et al., 2014).

Since its opening, the GoM's 1.6 x 10^6 km^2 of lithosphere has cooled and accumulated > 3 x 10^6 km^3 of clastic sediment along its northwestern margin, and carbonate banks along its eastern and southern margins (Figure 3.1a). Paleocene siliciclastic sedimentation in the northern GoM buried the Cretaceous carbonate platform (Winker and Buffler, 1988). Since then, the sediment wedge has prograded, aggraded, and slid more than 1000 km basinward creating the modern coastal plain, shelf, slope, and salt-floored thrust front.

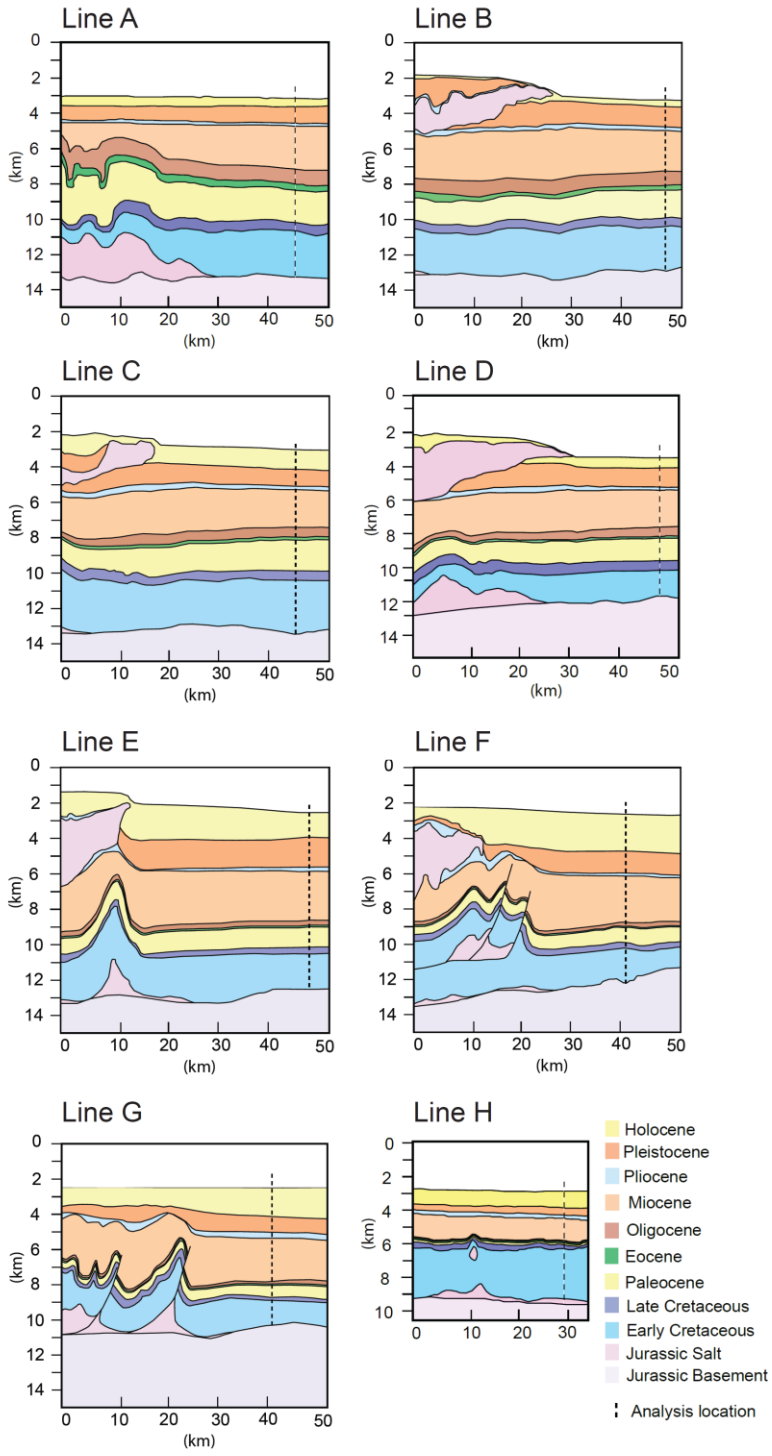

Figure 3.2. Line drawings of lines A-H (west-to-east) see figure 3.1 for locations, note the decrease in thickness of the Paleocene-Eocene section from west to east.

3.4 Methods

3.4.1 Subsidence Analysis

Decompaction and backstripping were carried out in *Move*™, and isostatic corrections (Angevine et al., 1990; Van Hinte, 1978) were applied to the abyssal portions of eight interpreted GulfSpan seismic lines (lines A-H Figure 3.1a and c). Geohistory analysis requires *a priori* knowledge of the age, lithology, and thickness of accumulated sediments (Figure 3.2), as well as the paleobathymetry of the basin over the time interval analyzed. The lack of deep wells in the abyssal GoM precludes direct knowledge of age and lithology at the locations analyzed, however, correlation of seismic stratigraphic interpretation conducted by *ION Geophysical* from the nearest deep wells allows some constraint. I use a compaction coefficient of 0.45/km and initial porosity of 0.6 values corresponding to a 25-75% sand-shale mix to approximate deepwater sedimentation. The 142-97 Ma portion of the subsidence curves are based on two assumptions: the unconformity at the base of the seismic sections postdates seafloor spreading from 158-142 Ma (Pindell, 1985), and the GoM achieved water depths of 3000 m by this time (Winker and Buffler, 1988). I include the effects of eustatic sea-level changes using estimates of long term, first-order average sea level (Haq, 1988) which show sea levels decreasing ~230 m since the Late Cretaceous. The calculated subsidence is then compared to predictions from models of dynamic topography over the last 150 Ma (Flament et al., 2014; Liu et al., 2011; Shephard

et al., 2014), and a model of the flexural response of the lithosphere to a thick prograding sediment wedge (Wangen, 2010) to evaluate the relative contributions of each.

3.4.2 Oligocene to Recent Flexure Modeling

The Gulf of Mexico (GoM) is a small ocean basin that opened ~ 140 My ago. As such its lithosphere is thermally mature. We use a Monte Carlo simulation based on the Wangen (2010) flexure model to examine the effects of load density and effective elastic thickness (Te) on flexural deflection. The system of the Monte Carlo model is defined by the standard equations for calculating flexural rigidity (D) and the flexural parameter (α) (see Wangen, 2010 for details). We hold Young's modulus (E), Poisson's ratio, ρ fill, and ρ mantle constant at 100 GPa, 0.25, 1035 kg/m^3 (seawater), and 3300 kg/m^3, respectively. The dimensions of the load and lithosphere's effective elastic thickness (*Te*) have the greatest impact on the results of the analysis; the density of the load plays a secondary role. Therefore, *Te* and ρ load are incorporated into the Monte Carlo model as random variables. Values used for the former are model trial dependent (see below), whereas the latter is allowed to vary between 2100 and 2700 kg/m^3 for all model simulations. The load's dimensions are the Oligocene to Pleistocene sedimentary section within the shelf. The Holocene is not included in the flexure analysis since it is still undergoing compaction. Estimates of *Te* in thermally

mature ocean basins range from 20 km to 50 km with most estimates between 40 and 50 km (Watts and Zhong, 2000). Watts and Zhong (2000) compiled published estimates of *Te*, however none of these studies examined small mature ocean basins like the GoM which may have greater *Te* than their larger oceanic counterparts due to the proximity of transitional and continental crust. Lines B, D, and F were chosen to represent the western, central, and eastern Gulf of Mexico (GoM) abyssal plain, respectively. Two trials were run for each analysis location. The first trial attempts to match the magnitude of Oligocene-Recent subsidence calculated in our subsidence analysis. In trial one the Monte Carlo simulation allows *Te* to vary between 40 and 80 km while filtering the results for the deflection predicted by our subsidence analysis. The second trial constrains *Te* to be 40-50 km and does not filter the resulting deflections. The results are presented in the Table 3 and in Figure 3.3.

Table 3. Parameters for Monte Carlo Flexure model

	Line B Trial 1	**Line B Trial 2**	**Line D Trial 1**	**Line D Trial 2**	**Line G Trial 1**	**Line G Trial 2**
Te Mean (km)	59.9 ± 6.1	45 ± 2.9	50.8 ± 1.7	45 ± 2.9	52 ± 1.6	45 ± 2.9
Mean load density (kg/m^3)	2277 ± 38	2433 ± 115	2265 ± 23	2436 ± 116	2633 ± 1	2437 ± 115
Flexural rigidity (D)	2.0e24 ± 5.7e23	8.2e23 ± 1.5e23	1.7e24 ± 1.1e23	8.2e23 ± 1.6e23	1.3e24 ± 1.1e23	8.2e23 ± 1.6e23
Distance from load (km)	24	24	25	25	20	20
Modeled Flexural Deflection (m)	1710 ± 1.7	1747 ± 151	1575 ± 1	1678 ± 152	1728 ± 1	1504 ± 124
Observed Oligocene–Recent subsidence (m)	1706	1706	1574	1574	1918	1918
Mismatch	-4 ± 1.7	-41 ± 151	-1 ± 1	-104 ± 152	190 ± 1	414 ±124
Number of Simulations	25,000	5,000	25,000	5,000	25,000	5,000

In trial one (*Te* = 40-80 km) in the western and central GoM we are able to match the results of our subsidence analysis, but are unable to do so in the east. In trial two (*Te* = 40-50 km), in western and central GoM, our model result is within uncertainty of the results of the subsidence analysis. In the eastern GoM we are still unable to match the results of the subsidence analysis. This is partially consistent with the general prediction of a dynamic topographic low imposed by the Farallon slab whose main mass is currently sinking below the

North American eastern board. However dynamic subsidence models predict that eastern and central GoM should be experiencing the same magnitude of the predictions of the dynamic subsidence (Figure 3.1) (Flament et al., 2014; Forte et al., 2010; Shephard et al., 2014) which does not fit the pattern of "missing" subsidence. None of our flexural models are consistent with a full kilometer of dynamically driven subsidence.

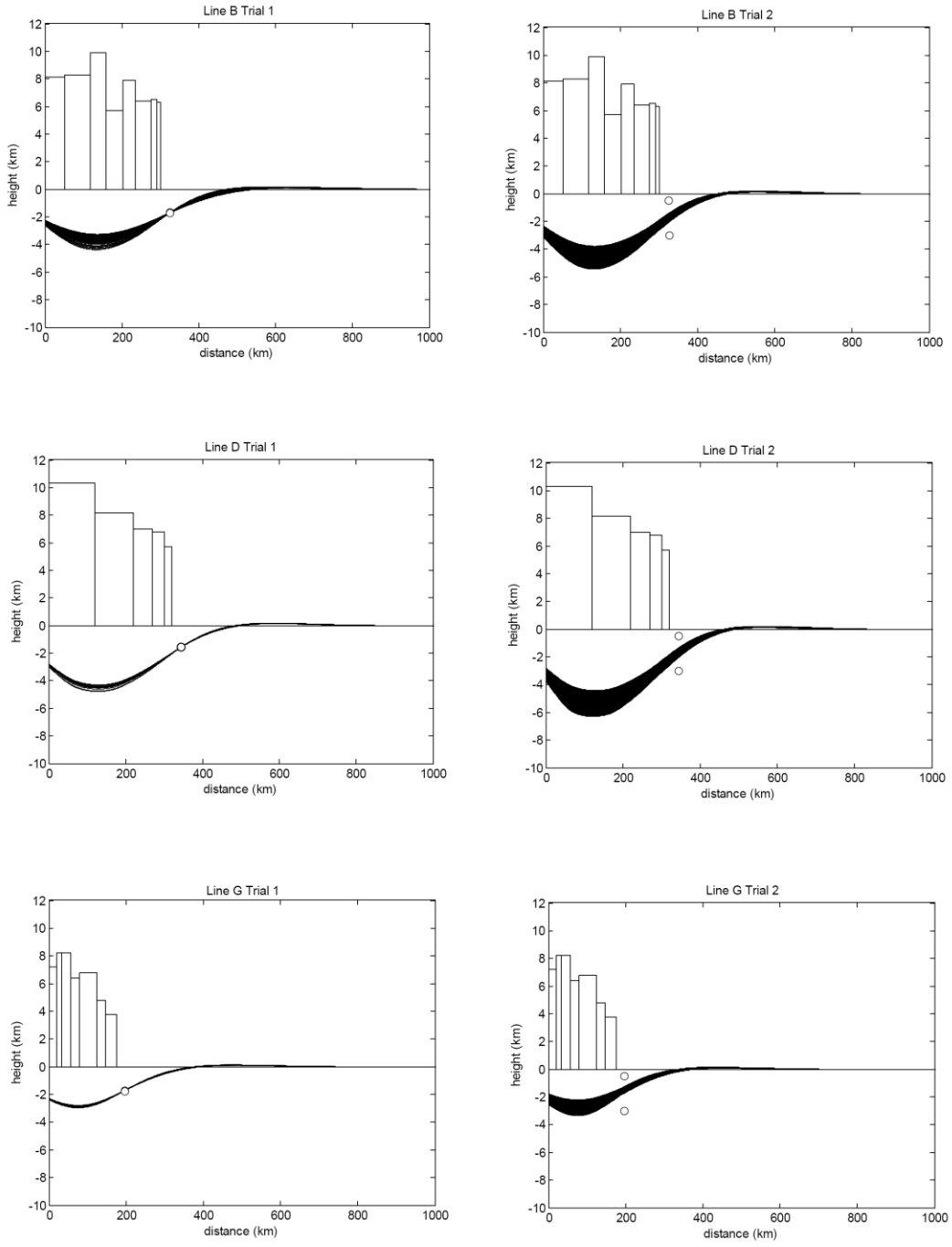

Figure 3.3. Results of Monte Carlo simulations of Oligocene to Recent flexure, rectangles are load blocks, horizontal position of circles marks the distance between load blocks and analysis location. Vertical position of circles show the range of deflections for which results have been filtered.

3.4.3 Line H Late Cretaceous Flexure

The location of our subsidence analysis of line H (easternmost line) is ~ 50 km from the Florida carbonate platform. This 6-7 km thick carbonate platform was active during the Late Jurassic and Cretaceous (Winker and Buffler, 1988) and influenced the early subsidence history of the adjacent seafloor. In order to compare the early subsidence history of line H to the rest of the subsidence analyses, we modeled the flexure associated with the growth of the Florida carbonate platform using a single load block 250 km wide and 6.5 km thick using a *Te* = 40 km (analysis location is on transitional crust), E = 1e11, load density = 2650 kg/m^3, in a water filled basin (Figure 3.4). Modeling suggests that nearly a kilometer of early subsidence was produced by flexure.

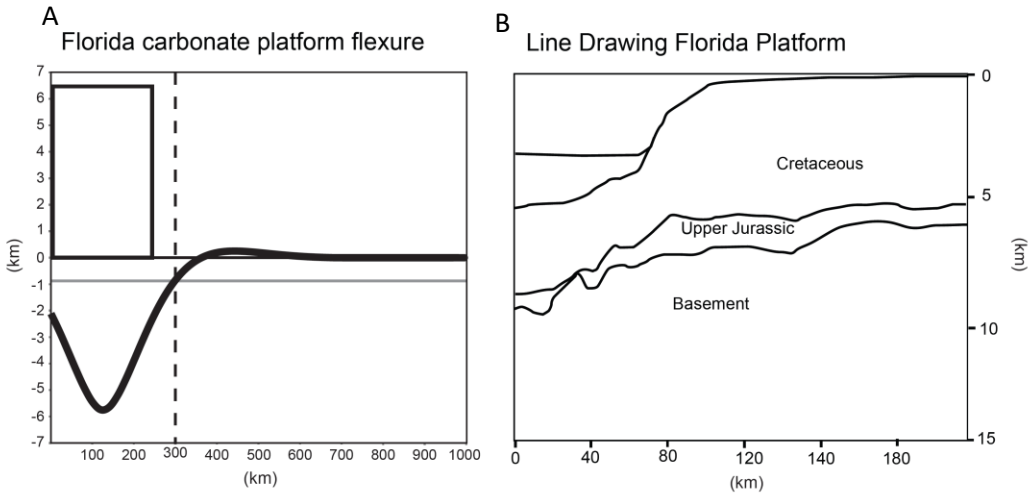

Figure 3.4 a) Results of flexure modeling (Wangen 2010) for Late Cretaceous subsidence along line H. Load block represents Florida carbonate platform. b) Line drawing of Florida carbonate platform *ION Geophysical* .

3.5 Results

Early Cretaceous northern GoM subsidence begins rapidly and then tails off to near zero, closely approximating the shape of the north Pacific thermal contraction curve of Parsons and Sclater (1977) and standard models of passive margin thermally driven subsidence (Xie and Heller, 2009) (Figure 3.1c). Most of our curves plot above the thermal contraction curve and between curves corresponding to initial stretching values (β factor) of 2-4. Our analysis reveals that the magnitude of stretching associated with basin opening is greatest in the western GoM and decreases systematically to the east (Figure 3.1c), consistent with its opening around a pole in the Straits of Florida. The proximity of line H to the Jurassic-Cretaceous Florida carbonate platform requires removing its associated flexure from its subsidence curve in order to compare initial stretching with the rest of our analyses. While most of our analyses are located on oceanic crust our easternmost sites (G and H) are likely located on transitional crust, and display the lowest amount of stretching.

Our results showed the northern abyssal GoM underwent two episodes of enhanced subsidence during the Cenozoic (Figure 3.1c). During the earlier, Paleocene–early Eocene episode the northwestern Gulf experienced a pulse of subsidence whose magnitude was greatest in the west (Figure 3.1 and 3.3). From 65–49 Ma the magnitude and rate of residual subsidence (a.k.a., tectonic

subsidence: sediment load removed) from the south Texas to Louisiana lines A–G is 1248-638 m at 78-40 m·My^{-1} and diminishes eastward to 188 m at 12 m·My^{-1} at the offshore Alabama line H (Figure 3.1 and 3.5). The eastern limit of Paleocene-Early Eocene rapid subsidence coincides with the Mississippi river. This basin asymmetry is reflected in the thickness of the Paleocene-Eocene sedimentary section which is 2-4 times thicker in the west than the east (Figure 3.2).

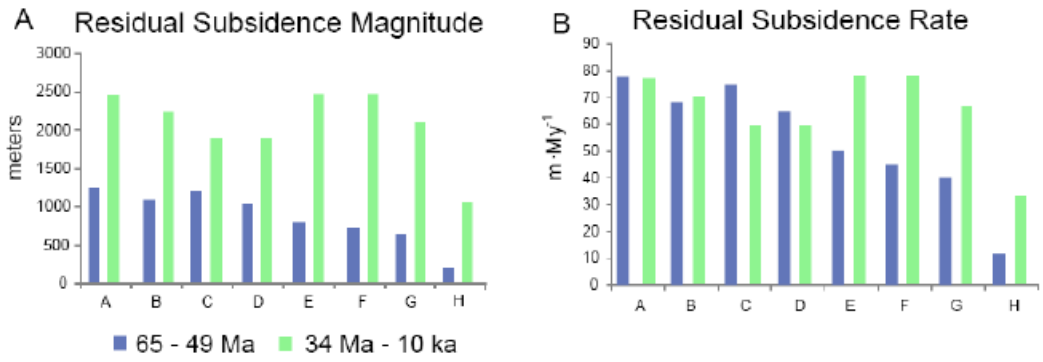

Figure 3.5. Histograms showing the magnitude and rate of subsidence at each analysis location.

During the Eocene the northern GoM has the lowest subsidence rate (3–17 m·My^{-1}) of any time since the Late Cretaceous. The magnitude and rate of Oligocene–Pliocene subsidence episodes display a bimodal distribution with maxima in the northeast and northwest GoM. The western maximum is centered at lines A and B where 2441 and 2229 m (Figure 3.5a) of residual subsidence developed at 76 and 70 m·My^{-1} (Figure 3.5b), and the eastern maximum is

centered at lines E and F where 2468 m (Figure 3.5a) of subsidence accumulated at 77 $m \cdot My^{-1}$ (Figure 3.5b) and decreases to the east and west . The initiation of rapid subsidence during the Oligocene is asymmetric as well. Lines A and B experience the most rapid Oligocene subsidence rates of 47 $m \cdot My^{-1}$ and 52 $m \cdot My^{-1}$, accompanied by more modest subsidence rates of 28 $m \cdot My^{-1}$, 31 $m \cdot My^{-1}$, and 34 $m \cdot My^{-1}$ at adjacent lines C, D, and E, respectively. Analysis locations east of the Louisiana-Mississippi border (F-H) record minimal increases in Oligocene subsidence with rates reaching only 10 $m \cdot My^{-1}$ to 18 $m \cdot My^{-1}$. During the Miocene the northern GoM experiences a spatially uniform pulse of rapid subsidence in which all locations subside at > 50 $m \cdot My^{-1}$ (Figure 3.1 and 3.5). Flexure modeling results reveals 200-400 m of "missing" subsidence at line G, 100 m at line D, and 0 m at line B (Figure 3.3). Analysis locations D and G are within the 0.5-1 km deep trough predicted by models of modern dynamic topography (Forte et al., 2010) and residual topography (Panasyuk and Hager, 2000).

3.6 Discussion

The timing and pattern of subsidence across the northern GoM in the early Cretaceous is consistent with post-rifting thermal subsidence. The latter half of this subsidence episode (120–100 Ma) coincides with rapid dynamic subsidence in the western GoM predicted by geodynamic modeling (Flament et al., 2014; Shephard et al., 2014). However, comparison of our subsidence analysis to the

expected thermal contraction curves leaves no room for the predicted 1 km of dynamic subsidence. Subtracting the predicted dynamic component from the subsidence curves yields unrealistically low stretching factors of 1–2 during seafloor spreading (Figure 3.6a).

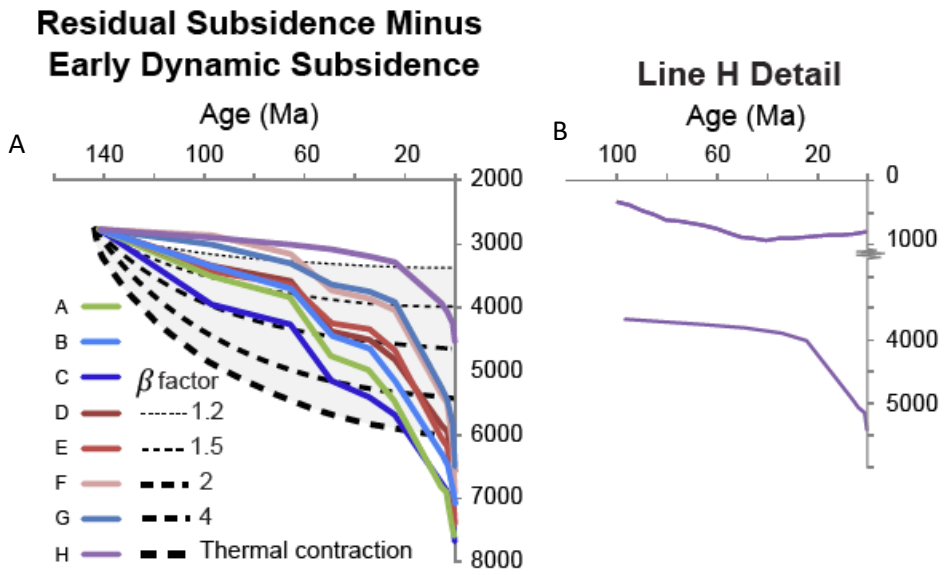

Figure 3.6 a) Comparison of residual subsidence curves with the Late Cretaceous predicted dynamic subsidence subtracted and β factor curves. b) Line H 100 Ma to present residual subsidence (bottom) and predicted dynamic subsidence (top).

The dynamic topography model of Flament et al. (2014) and Shephard et al. (2014) predicts that the western GoM began to rise dynamically at 70 Ma and the eastern GoM at 40 Ma, which contrasts with the subsidence history (Figure 3.1c). The magnitude of western GoM residual subsidence from 100-34 Ma is large enough that it could conceivably mask the predicted dynamic rise. However, in the easternmost GoM (line H) the magnitude of 100-34 Ma subsidence is only 1/3 of the predicted dynamic subsidence (Figure 3.1c and

3.4b). This suggests that by the time the Farallon slab was located below the eastern GoM the vertical traction it imparted was almost entirely attenuated by the intervening mantle and asthenosphere.

The Paleocene-early Eocene subsidence episode began simultaneously across the northwestern GoM and coincided temporally with two interrelated events: rapid exhumation of Laramide uplifts, and a major pulse of GoM sedimentation (Epis and Chapin, 1975; Fan and Carrapa, 2014; Galloway et al., 2011; Peyton et al., 2012). While the emplacement of Laramide thrust sheets in eastern Mexico likely contributed to the exceptionally rapid, ~200 $m \cdot My^{-1}$, 60-44 Ma subsidence event in the western GoM (Feng et al., 1994) it is unlikely to have affected locations discussed here. While the Laramide thrust front is ~400 km from the locations of Feng et al., (1994), approaching the maximum horizontal dimensions of flexural foreland basins, Laramide crustal thickening is 500–1000 km from our NW GoM locations that underwent simultaneous enhanced subsidence. The thickness of the GoM Paleocene-Eocene sedimentary section shows that the northwestern GoM received more than 2-4 times the volume of sediment as the northeastern GoM (Figure 3.2) creating the pronounced asymmetry evident in our subsidence analysis (Figure 3.1c). This is consistent with a paleogeographic reconstruction during this time interval in which the Rio Grande and Colorado rivers fed the main GoM depocenters, focusing sedimentation in the western GoM (Galloway et al., 2011). The Oligocene–Recent subsidence episode coincides with the initiation of Oligocene-Miocene

salt canopies, regional salt floored gravity slides, and the progradation and aggradation of the sediment wedge to its current position adjacent to our analysis locations (Diegel et al., 1995; Galloway et al., 2011; Peel et al., 1995). The pattern of enhanced subsidence initiation during this episode correlates with the spatiotemporal pattern of GoM sedimentation in which the major depocenters shift to the northwest GoM and are fed by the Rio Bravo, Rio Grande, and Houston-Brazos rivers from the Latest Eocene-Early Miocene, while the Mississippi becomes the primary fluvial axis during the Early Oligocene before being joined in the northeast GoM by the Red and Tennessee drainages during the Early and Middle Miocene, respectively (Galloway et al., 2011). Flexural modeling can account for 78–100% of the calculated Oligocene–Recent subsidence, with a maximum deviation of 400 m. This mismatch may be due to uncertainties in model parameters (e.g., compaction coefficient, seismic velocity models etc.). Alternatively, it may place a maximum on the amount dynamic subsidence present in the GoM. None of our models are consistent with a km of dynamic subsidence, nor are they consistent with the spatial pattern predicted by geodynamic models (Flament et al., 2014; Forte et al., 2010; Shephard et al., 2014).

3.7 Conclusions

Decompaction, backstripping, and isostatic correction of eight seismic sections identified three major episodes of regional subsidence in the northern GoM. The first episode, from 142–97 Ma is consistent with thermal contraction following initial sea-floor spreading. Subsidence during the second episode spanning the Paleocene–early Eocene was greatest in the west and decreased eastward to almost zero at the longitude of the Mississippi River. This episode correlates with asymmetric filling of the northwestern GoM driven by a pulse of sediment shed from Laramide uplifts. During this subsidence event, 2-4 times as much sediment reached the northwest GoM as the northeast. The third episode, starting in the Oligocene, is bimodal, focused in the western and central GoM, and attenuates to the west and east. Subsidence during this event is consistent with flexural modeling of thermally-mature oceanic crust loaded by the prograding and aggrading Oligocene–Pliocene sediment wedge.

The subsidence history of the GoM can be explained by thermal contraction, asymmetric filling of the basin, and advance of the thrust-floored shelf. Both of the Paleocene–Eocene and Oligocene–Pliocene episodes of enhanced subsidence correlate spatially and temporally with the pattern of regional sedimentation. If there is a dynamic topographic response to the basal traction imposed by the sinking Farallon plate it appears to be no greater than 400 meters.

3.8 References

Angevine, C.L., Heller, P.L., and Paola, C., 1990, Subsidence Analysis: Chapter 3, p. 7-19.

Bird, D.E., Burke, K., Hall, S.A., and Casey, J.F., 2005, Gulf of Mexico tectonic history: Hotspot tracks, crustal boundaries, and early salt distribution: AAPG Bulletin, v. 89, p. 311-328.

Braun, J., 2010, The many surface expressions of mantle dynamics: Nature Geoscience, v. 3, p. 825-833.

Bunge, H.-P., and Grand, S.P., 2000, Mesozoic plate-motion history below the northeast Pacific Ocean from seismic images of the subducted Farallon slab: Nature, v. 405, p. 337-340.

Diegel, F. A., J. F. Karlo, D. C. Schuster, R. C. Shoup, and P. R. Tauvers, 1995, Cenozoic structural evolution and tectono-stratigraphic framework of the northern Gulf coast continental margin, *in* M. P. A. Jackson, D. G. Roberts, and S. Snelson, eds., Salt tectonics: a global perspective: AAPG Memoir 65, p. 109-151.

Eddy, D.R., Van Avendonk, H.J., Christeson, G.L., Norton, I.O., Karner, G.D., Johnson, C.A., and Snedden, J.W., 2014, Deep crustal structure of the northeastern Gulf of Mexico: Implications for rift evolution and seafloor spreading: Journal of Geophysical Research: Solid Earth, v. 119, p. 6802-6822.

Epis, R.C., and Chapin, C.E., 1975, Geomorphic and tectonic implications of the post-Laramide, late Eocene erosion surface in the southern Rocky Mountains: Geological Society of America Memoirs, v. 144, p. 45-74.

Fan, M., and Carrapa, B., 2014, Late Cretaceous–early Eocene Laramide uplift, exhumation, and basin subsidence in Wyoming: Crustal responses to flat slab subduction: Tectonics, v. 33, p. 509-529.

Feng, J., Buffler, R.T., and Kominz, M.A., 1994, Laramide orogenic influence on late Mesozoic-Cenozoic subsidence history, western deep Gulf of Mexico basin: Geology, v. 22, p. 359-362.

Flament, N., Gurnis, M., and Müller, R.D., 2013, A review of observations and models of dynamic topography: Lithosphere, v. 5, p. 189-210.

Flament, N., Gurnis, M., Williams, S., Seton, M., Skogseid, J., Heine, C., and Müller, R.D., 2014, Topographic asymmetry of the South Atlantic from global models of mantle flow and lithospheric stretching: Earth and Planetary Science Letters, v. 387, p. 107-119.

Forte, A., Moucha, R., Simmons, N., Grand, S., and Mitrovica, J., 2010, Deep-mantle contributions to the surface dynamics of the North American continent: Tectonophysics, v. 481, p. 3-15.

Galloway, W.E., Whiteaker, T.L., and Ganey-Curry, P., 2011, History of Cenozoic North American drainage basin evolution, sediment yield, and accumulation in the Gulf of Mexico basin: Geosphere, v. 7, p. 938-973.

Gurnis, M., 1990, Bounds on global dynamic topography from Phanerozoic flooding of continental platforms: Nature, v. 344, p. 754-756.

Hager, B.H., Clayton, R.W., Richards, M.A., Comer, R.P., and Dziewonski, A.M., 1985, Lower mantle heterogeneity, dynamic topography and the geoid: Nature, v. 313, p. 541-545.

Haq, B.U., 1988, Mesozoic and Cenozoic chronostratigraphy and cycles of sea-level change: Society of Exploration Paleontologists and Mineralogists, v. 42, p. 71-108.

Hudec, M.R., Norton, I.O., Jackson, M.P., and Peel, F.J., 2013, Jurassic evolution of the Gulf of Mexico salt basin: AAPG Bulletin, v. 97, p. 1683-1710.

Kaban, M., Schwintzer, P., and Reigber, C., 2004, A new isostatic model of the lithosphere and gravity field: Journal of Geodesy, v. 78, p. 368-385.

Liu, S., Nummedal, D., and Liu, L., 2011, Migration of dynamic subsidence across the Late Cretaceous United States Western Interior Basin in response to Farallon plate subduction: Geology, v. 39, p. 555-558.

Molnar, P., England, P.C., and Jones, C.H., 2015, Mantle dynamics, isostasy, and the support of high terrain: Journal of Geophysical Research: Solid Earth, v. 120, p. 1932-1957.

Moy, C., and Traverse, A., 1986, Palynostratigraphy of the subsurface eagle mills formation (Triassic) from a well in east-central texas, USA: Palynology, v. 10, p. 225-234.

Panasyuk, S.V., and Hager, B.H., 2000, Models of isostatic and dynamic topography, geoid anomalies, and their uncertainties: Journal of Geophysical Research: Solid Earth (1978–2012), v. 105, p. 28199-28209.

Peel, F. J., C. J. Travis, and J. R. Hossack, 1995, Genetic structural provinces and salt tectonics of the Cenozoic offshore U.S. Gulf of Mexico: a preliminary analysis, *in* M. P. A. Jackson, D. G. Roberts, and S. Snelson, eds., Salt tectonics: a global perspective: AAPG Memoir 65, p. 153-175.

Peyton, S.L., Reiners, P.W., Carrapa, B., and DeCelles, P.G., 2012, Low-temperature thermochronology of the northern Rocky Mountains, western USA: American Journal of Science, v. 312, p. 145-212.

Pindell, J.L., 1985, Alleghenian reconstruction and subsequent evolution of the Gulf of Mexico, Bahamas, and Proto-Caribbean: Tectonics, v. 4, p. 1-39.

Pindell, J.L., and Kennan, L., 2009, Tectonic evolution of the Gulf of Mexico, Caribbean and northern South America in the mantle reference frame: an update: Geological Society, London, Special Publications, v. 328, p. 1-55.

Salvador, A., 1987, Late Triassic-Jurassic paleogeography and origin of Gulf of Mexico basin: AAPG Bulletin, v. 71, p. 419-451.

Sandwell, D.T., Müller, R.D., Smith, W.H.F., Garcia, E., and Francis, R., 2014, New global marine gravity model from CryoSat-2 and Jason-1 reveals buried tectonic structure: Science, v. 346, p. 65-67.

Shephard, G., Flament, N., Williams, S., Seton, M., Gurnis, M., and Müller, R., 2014, Circum-Arctic mantle structure and long-wavelength topography

since the Jurassic: Journal of Geophysical Research: Solid Earth, v. 119, p. 7889-7908.

Van Avendonk, H.J., Christeson, G.L., Norton, I.O., and Eddy, D.R., 2015, Continental rifting and sediment infill in the northwestern Gulf of Mexico: Geology, v. 43, p. 631-634.

Van Hinte, J., 1978, Geohistory analysis--application of micropaleontology in exploration geology: AAPG Bulletin, v. 62, p. 201-222.

Wangen, M., 2010, Physical principles of sedimentary basin analysis, Cambridge University Press.

Watts, A.B., 2001, Isostasy and Flexure of the Lithosphere, Cambridge University Press.

Winker, C.D., and Buffler, R.T., 1988, Paleogeographic evolution of early deep-water Gulf of Mexico and margins, Jurassic to Middle Cretaceous (Comanchean): AAPG Bulletin, v. 72, p. 318-346.

Xie, X., and Heller, P.L., 2009, Plate tectonics and basin subsidence history: Geological Society of America Bulletin, v. 121, p. 55-64.